Astronomy Letters, Vol. 26, No. 7, 2000, pp. 413–422. Translated from Pis'ma v Astronomicheskiĭ Zhurnal, Vol. 26, No. 7, 2000, pp. 483–492.

Observations of Cosmic Gamma-Ray Bursts with the Main Detector of the SIGMA Telescope onboard the Granat Observatory

R. A. Burenin[1]*, O. V. Terekhov[1], R. A. Sunyaev[1, 2], A. V. D'yachkov[1], G. Khavenson[1], B. S. Novikov[1], I. D. Tserenin[1], K. M. Sukhanov[1], P. Goldoni[3], A. Claret[3], A. Goldwurm[3], J. Paul[3], F. Pelaez[4], E. Jourdain[4], J.-P. Roques[4], and G. Vedrenne[4]

[1] *Space Research Institute, Russian Academy of Sciences, ul. Profsoyuznaya 84/32, Moscow, 117810 Russia*
[2] *Max Planck Instutut für Astrophysik, Karl-Schwarzschild-Strasse 1, 86740 Garching bei München, Germany*
[3] *Service d'Astrophysique, Centre d'Etudes Nucleaires de Saclay, 91191 Gif-sur-Yvette Cedex, France*
[4] *Centre d'Etude Spatiale des Rayonnements (CNRS/UPS) 9, avenue du Colonel Roche, B.P. 4346, F-31028 Toulouse Cedex, France*

Received October 13, 1999; in final form, December 27, 1999

Abstract—We present the observations of cosmic gamma-ray bursts (GRBs) with the main detector of the SIGMA telescope onboard the Granat Observatory from January 1990 through September 1994. The observations were carried out in the energy range 35–1300 keV. We detected 36 GRBs and 31 high-energy solar flares during this period. No GRB fell within the main field of view; they were all recorded by the "secondary optics" of the telescope. The SIGMA telescope recorded relatively bright bursts with peak fluxes of 10^{-6}–10^{-4} erg s^{-1} cm^{-2} in the 100–500-keV energy band. Stable detector background allows the long-term variability of GRB sources on a time scale of ~1000 s to be studied. The results of our search for early afterglows of GRBs are presented. The flux averaged over all bursts in the interval 100–800 s after the main event is 0.36 ± 0.14 counts s^{-1}(35–300 keV), suggesting that there is soft gamma-ray emission on this time scale after a considerable number of GRBs.

Key words: *cosmic gamma-ray bursts*

DESCRIPTION OF THE INSTRUMENT

The SIGMA telescope is part of the scientific payload of the Granat Orbiting Observatory. It operates on the principle of a coded aperture and consists of a coded mask, a position-sensitive detector, and passive and active anticoincidence shields. The telescope is designed to form images with an angular resolution of ~15′ in the energy range 35–1300 keV. Its sensitivity is at a maximum in a $4\overset{\circ}{.}3 \times 4\overset{\circ}{.}7$ region (the region of complete coding). The main field of view is $11\overset{\circ}{.}4 \times 10\overset{\circ}{.}5$ at half sensitivity (see [1] for a detailed description of the telescope).

The X-ray and gamma-ray radiation from sources outside the SIGMA main field of view can fall on the detector by passing through slits between individual protection units. Given the positions and geometrical sizes of these slits, the source coordinates can be restored with an accuracy of ~1° from the burst image on the detector. The "secondary optics" was described in detail by Claret *et al.* [2]. The diagram of SIGMA sensitivity to GRBs averaged relative to the pointing axis is given in [3]. The telescope detector can be roughly assumed to record bursts from directions within 90° of the pointing direction, but the SIGMA sensitivity to them is a factor of 10–20 lower than the sensitivity to bursts within the main field of view. The latter depends on burst duration and is $(4\text{–}10) \times 10^{-8}$ and $(2\text{–}5) \times 10^{-7}$ erg s^{-1} cm^{-2} in the 40–90- and 90–750-keV energy bands, respectively [3].

In this paper, we present our five-year-long observations: from January 1990 through September 1994. Over this period, 802 observing sessions, each with a duration of 20–30 h, were carried out. The total observing time was 3.9×10^7 s. Since September 1994, the Granat Observatory has operated most of the time in "scanning mode," in which cosmic GRBs were difficult to observe with the SIGMA telescope.

OBSERVATIONS

To detect cosmic GRBs, the SIGMA main detector is equipped with a burst cell whose signal triggers a more detailed data recording than that in the main operation mode. The burst cell consists of four independent triggers operating in two broad energy bands (40–90

* E-mail address for contacts: br@hea.iki.rssi.ru

Table 1

N	Session number	Burst designation[1]	Triggering time	$T_{1/2}$, s	Peak flux		Confirmations
					counts s^{-1}	100–500 keV $\times 10^{-5}$ erg s^{-1} cm^{-2}	
1	64	900327	$10^h24^m28^s.1$	66.3	300		
2	66	900404	$17^h54^m35^s.2$	0.25	1200	2.3 ± 0.9	PW
3	70	900413	$3^h12^m37^s.5$	13.7	930	2.0 ± 0.8	P
4	87	900520	$12^h10^m17^s.5$	0.57	1500	7.3 ± 2.8	P
5	96	900604	$17^h31^m33^s.5$	0.45	700	1.7 ± 0.7	P
6	97	900605	$19^h23^m4^s.3$	3.3	240	0.59 ± 0.23	P
7	127	900720	$21^h45^m6^s.6$	9.6	270	0.30 ± 0.12	P
8	177	901014	$1^h13^m21^s.2$	4.2	550	0.89 ± 0.34	P
9	185	901027	$4^h21^m6^s.7$	8.6	320	0.32 ± 0.13	PW
10	228	910122	$15^h13^m48^s.6$	15.5	1600	1.0 ± 0.4	*PW
11	273	910417	$20^h7^m32^s.5$	14.9	530	1.1 ± 0.4	P
12	282	910517	$5^h2^m44^s.5$	3.1	250	0.44 ± 0.17	PW
13	315	910814	$19^h14^m34^s.8$	3.1	300	0.98 ± 0.37	PWB
14	320	910821	$10^h33^m57^s.7$	45.0	240	0.29 ± 0.11	PW
15	367	911119	$17^h12^m34^s.5$	0.32	410	0.18 ± 0.08	P
16	397	920125	$8^h57^m27^s.2$	0.24	900	0.58 ± 0.23	P
17	422	920311	$2^h20^m29^s.2$	11.4	590	1.8 ± 0.7	PWB
18	430	920325	$17^h17^m36^s.7$	0.47	500	0.82 ± 0.25	PWB
19	441	920414	$23^h22^m43^s.0$	1.1	320	0.65 ± 0.25	PB
20	468	920622	$7^h5^m6^s.8$	14.5	600	1.2 ± 0.5	PB
21	482	920714	$13^h4^m31^s.0$	25.0	600	0.48 ± 0.20	*PWB
22	486	920720	$3^h12^m9^s.2$	5.4	450	1.5 ± 0.6	PB
23	489	920723	$20^h3^m8^s.3$	5.0	5400	6.3 ± 2.4	*PW
24	546	930106	$15^h37^m39^s.5$	0.28	810	5.8 ± 2.3	PWB
25	575	930310	$7^h20^m7^s.2$	7.4	560		*B
26	578	930314	$2^h10^m32^s.0$	4.1	310	0.47 ± 0.19	P
27	626	930706	$5^h13^m30^s.9$	0.29	450	2.0 ± 0.8	PWB
28	672	931008	$0^h1^m59^s.7$	0.17	1100	0.43 ± 0.17	P
29	687	931205	$14^h59^m51^s.4$	0.24	660	3.1 ± 1.2	PB
30	703	940203	$15^h46^m59^s.7$	2.5	370	0.38 ± 0.15	PB
31	705	940206	$0^h8^m46^s.4$	7.1	1000	1.8 ± 0.7	*PB
32	714	940226	$12^h4^m53^s.5$	1.6	530		P
33	720	940310	$5^h0^m56^s.7$	1.0	520	2.8 ± 1.1	P
34	739	940415	$17^h1^m13^s.9$	0.42	620	0.16 ± 0.07	PB
35	770	940703	$4^h41^m16^s.9$	20.8	670	2.8 ± 1.1	PWB
36	795	940921	$5^h8^m21^s.3$	4.1	470		B

Notes: 1. The burst designations, as is customary, are composed of the last two digits of the year, month, and day when the burst was detected. Confirmations: * Localized by the secondary optics [2, 10]; P—PHEBUS/Granat [5–7]; W—WATCH/Granat [11]; B—BATSE/CGRO [12].

Table 2

N	Session number	Year	Month	Day	Triggering time	*N*	Session number	Year	Month	Day	Triggering time
1	69	1990	4	11	$16^h41^m40^s$	17	289	1991	5	31	$16^h54^m29^s$
2	71	1990	4	13	$21^h25^m46^s$	18	290	1991	6	1	$14^h57^m41^s$
3	72	1990	4	15	$2^h44^m47^s$	19	304	1991	6	30	$2^h56^m12^s$
4	92	1990	5	24	$20^h46^m59^s$	20	309	1991	7	17	$6^h25^m53^s$
5	100	1990	6	10	$7^h17^m5^s$	21	354	1991	10	14	$17^h34^m44^s$
6	101	1990	6	11	$9^h43^m11^s$	22	363	1991	10	26	$20^h35^m50^s$
7	145	1990	8	27	$20^h57^m57^s$	23	378	1991	12	15	$6^h23^m53^s$
8	201	1990	12	4	$2^h0^m41^s$	24	380	1991	12	20	$14^h2^m53^s$
9	210	1990	12	14	$13^h32^m13^s$	25	398	1992	1	26	$15^h27^m59^s$
10	216	1990	12	24	$15^h34^m43^s$	26	402	1992	2	7	$13^h58^m4^s$
11	231	1991	1	25	$6^h29^m41^s$	27	405	1992	2	11	$4^h22^m44^s$
12	236	1991	2	6	$6^h56^m17^s$	28	484	1992	7	16	$16^h55^m35^s$
13	252	1991	3	12	$12^h42^m2^s$	29	528	1992	10	27	$6^h52^m8^s$
14	255	1991	3	14	$18^h11^m55^s$	30	530	1992	10	29	$16^h11^m43^s$
15	256	1991	3	22	$22^h53^m0^s$	31	596	1993	4	18	$19^h8^m26^s$
16	281	1991	5	16	$6^h47^m32^s$						

and 90–750 keV) and with two integration times (0.25 and 2 s). The recording of detailed burst information begins if the count rate averaged over 0.25 or 2 s in any of the two energy bands exceeds the count rate averaged over the 64 previous seconds by nine standard deviations. Subsequently, 512 blocks, each containing information about the energies and positions of 63 photons on the detector and the arrival time of every 63rd photon, is written into the telescope memory. The first 64 blocks refer to the photons that have arrived before the cell triggering. The time resolution depends on the detector count rate and varies over the range 0.1–0.01 s. Detailed information about the count rate is recorded for several tens of seconds after the cell triggering, depending on burst intensity. In addition, during the entire observing session, the SIGMA detector count rate is written continuously into the onboard memory in four broad energy channels (35–70, 70–150, 150–300, and 300–600 keV) with 4-s resolution.

A total of 366 SIGMA burst cell triggerings have been recorded over five years of operation. Of them, 197 are false, 41 were caused by solar flares, 69 were

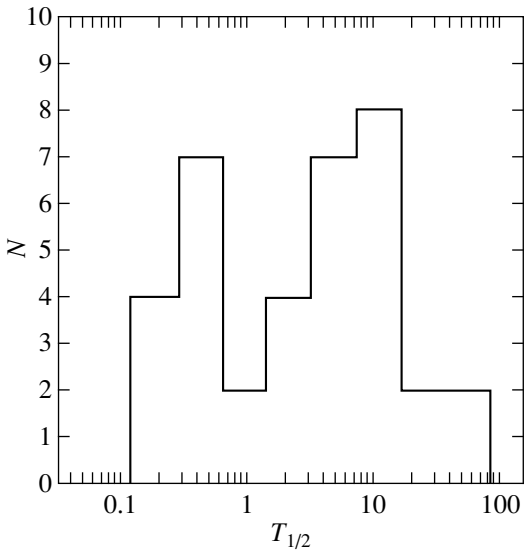

Fig. 1. The distribution of bursts in duration $T_{1/2}$.

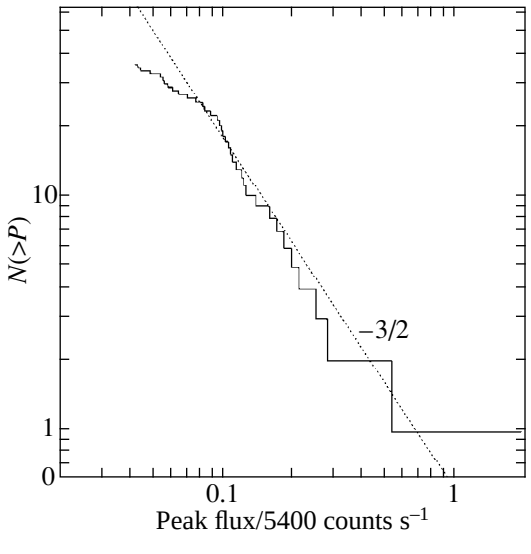

Fig. 2. The $\log N(>P)$–$\log P$ relation. The ratio of the burst peak count rates to the peak count rate of the brightest GRB 920723 is plotted along the *x* axis.

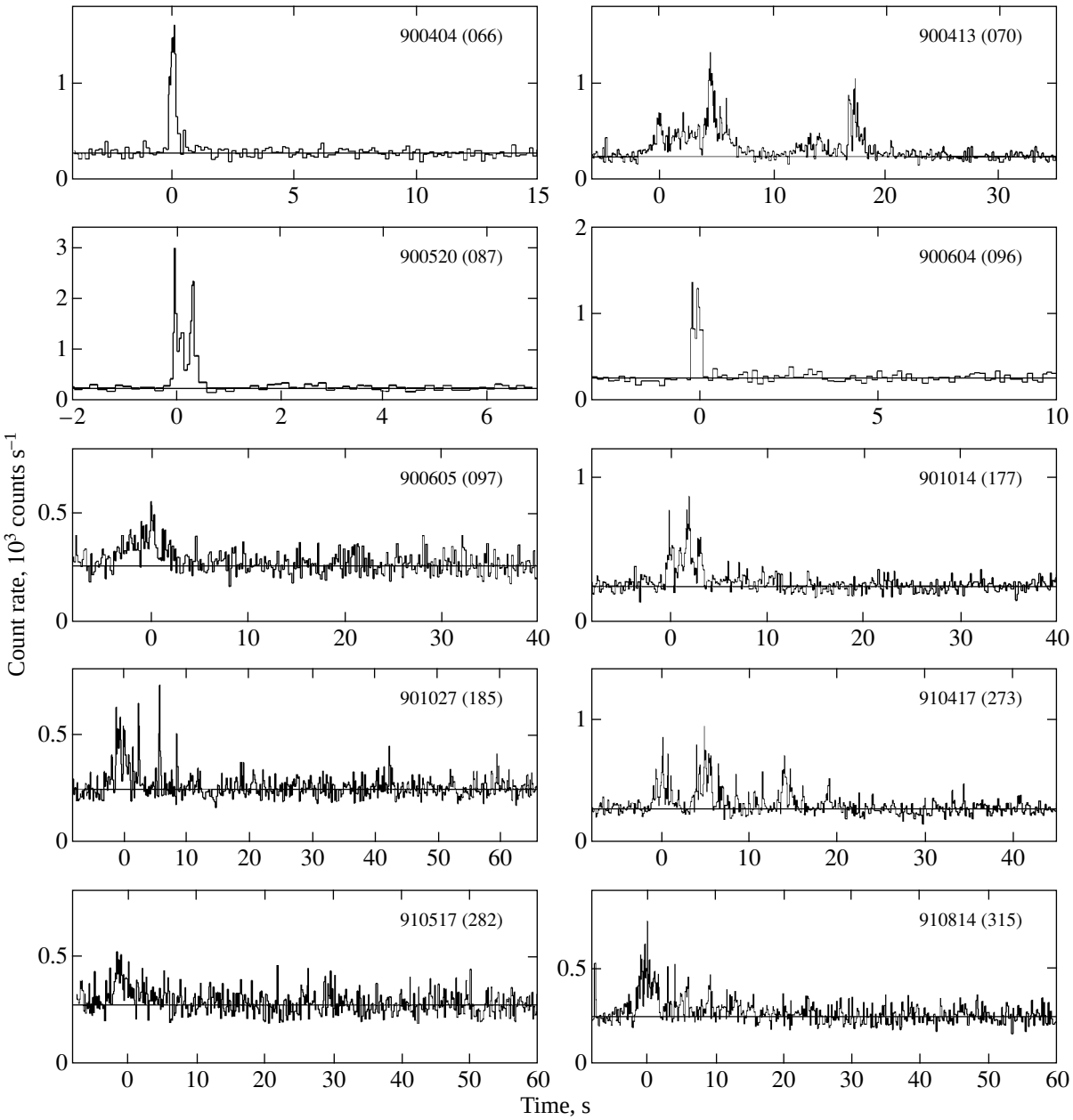

Fig. 3. Time histories of the detected GRBs in the 35–300-keV energy band. Same in Figs. 4–9.

caused by high-energy charged particles, seven events resulted from the detection of ultrarelativistic multicharged heavy-element nuclei (see, e.g., [4]), and 36 events are cosmic GRBs. The causes of the remaining triggerings could not be established reliably.

Table 1 provides basic data on the cosmic GRBs detected by the SIGMA telescope. Apart from running numbers, session numbers, and triggering times, the table gives burst durations at half maximum of the time history ($T_{1/2}$). The use of this characteristic of burst duration stems from the fact that this parameter is distorted only slightly during measurements with different sensitivities, because it is unrelated to low-flux measurements in the "tails" of the burst time histories. The table also gives peak count rates on a time scale of 0.1 s in the 35–300-keV energy band. The background count rate in this band is typically ~300 counts s^{-1}. The next column gives burst peak fluxes in the 100–500-keV energy band, as measured with the PHEBUS instrument [5–7]. The errors are not only statistical; we took into account uncertainty in the effective area of the instrument. It is evident from the table that the SIGMA telescope detects relatively bright bursts with peak fluxes ranging from 10^{-6} to 10^{-4} erg s^{-1} cm^{-2}.

All the detected bursts passed through the regions of weakened protection of the telescope detector men-

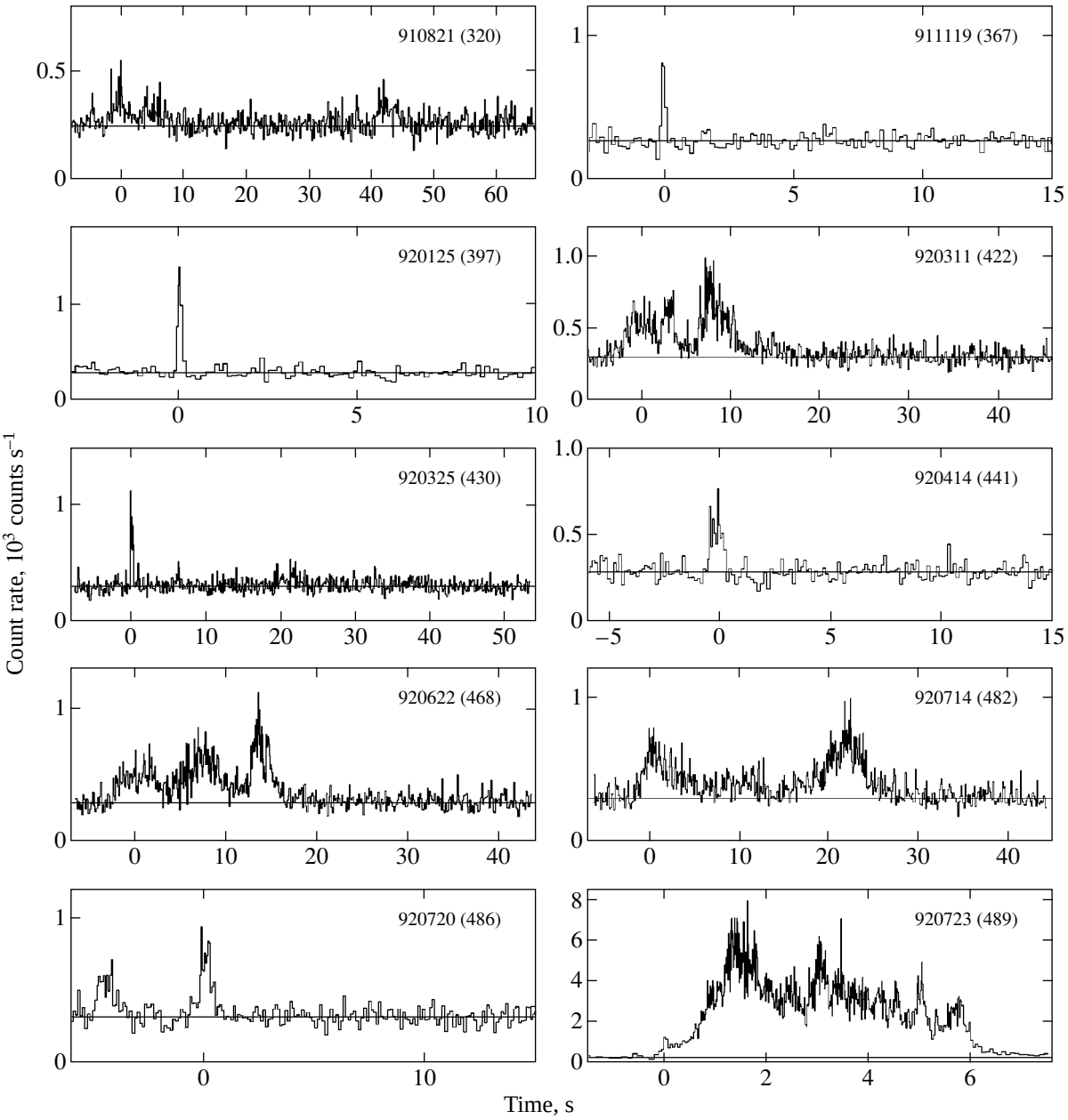

Fig. 4.

tioned above. Five GRBs were localized by their images on the detector [8–10]. These bursts are marked by asterisks in the "confirmations" column of Table 1. The same column lists some other instruments that observed the burst in question: PHEBUS [5–7], WATCH onboard the Granat Observatory [11], and BATSE [12] onboard the CGRO Observatory. Almost all the GRBs detected by the SIGMA telescope were observed by one of the above instruments.

The SIGMA telescope can localize virtually any burst that caused a cell triggering and that is located within the main field of view with an accuracy of the order of several arcminutes [3]. If the burst sources were uniformly distributed in Euclidean space, then about 30 bursts would fall within the main field of view over the entire period of observations. However, none of the bursts fell within the SIGMA main field of view. This is in agreement with the observed deficit of weak bursts compared to their number expected for a uniform distribution of sources in Euclidean space (see the review [13] for references).

For completeness, Table 2 lists the high-energy solar flares detected by the SIGMA telescope. A total of 31 solar flares were recorded; all of them were also observed by the PHEBUS instrument [14]. Some of them caused several burst cell triggerings in a row. In

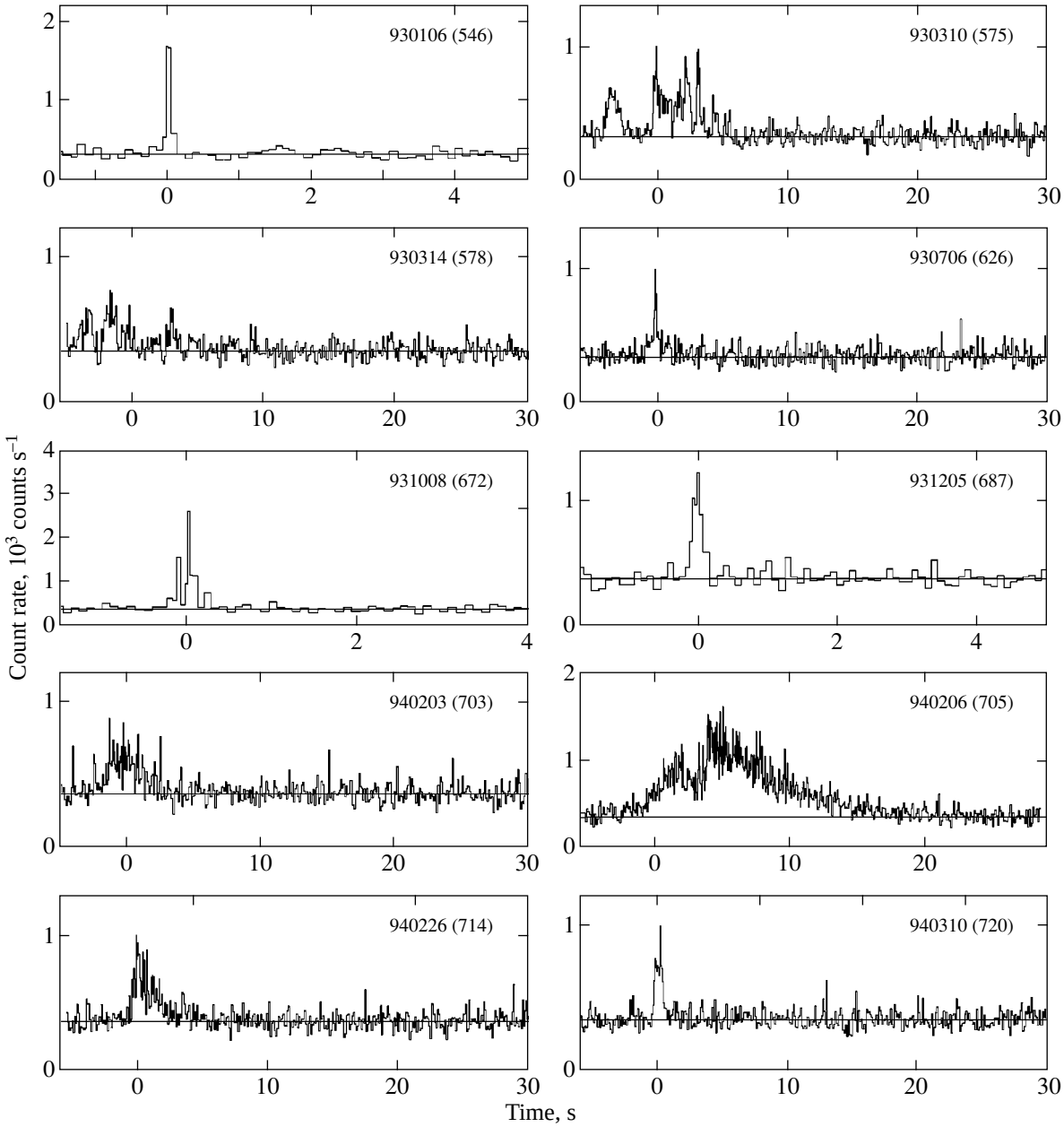

Fig. 5.

these cases, only the time of the first triggering is given in the table.

RESULTS

Figure 1 shows the distribution of GRBs in duration $T_{1/2}$. This distribution exhibits two maxima separated by a minimum at $T_{1/2} \approx 1$ s, as was previously observed in other experiments (see, e.g., references in the review [13]). The bimodal structure of the distribution of GRBs in duration suggests that the short and long bursts differ markedly in nature. PHEBUS/Granat data revealed that the short bursts are generally harder than the long ones [15, 16]. Furthermore, there are indications that the sources of short bursts may be uniformly distributed in Euclidean space [17]. Figure 2 shows the $\log N(>P) - \log P$ relation for the bursts detected by SIGMA. The ratio of the burst peak count rates to the peak count rate of the brightest GRB 920723 is plotted along the x axis. We see from the figure that this relation is closely fitted by a –3/2 power law. The deviation in the part of the count-rate curve corresponding to the weakest bursts is attributable to selection effects, which arise during the burst cell operation. The good agreement with the –3/2 power law suggests that most of the detected bursts come from distances at which their distribution is still uniform or

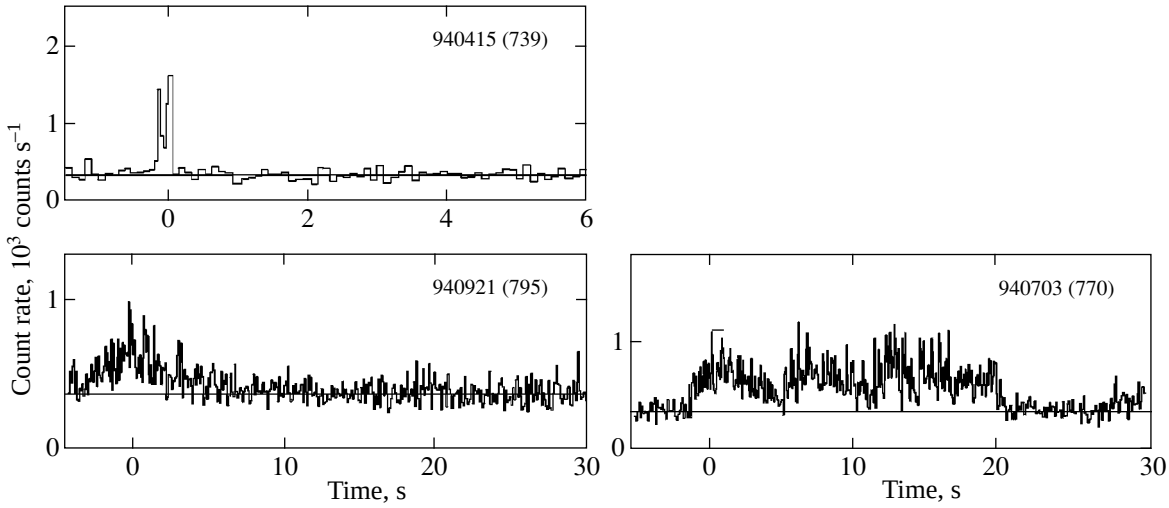

Fig. 6.

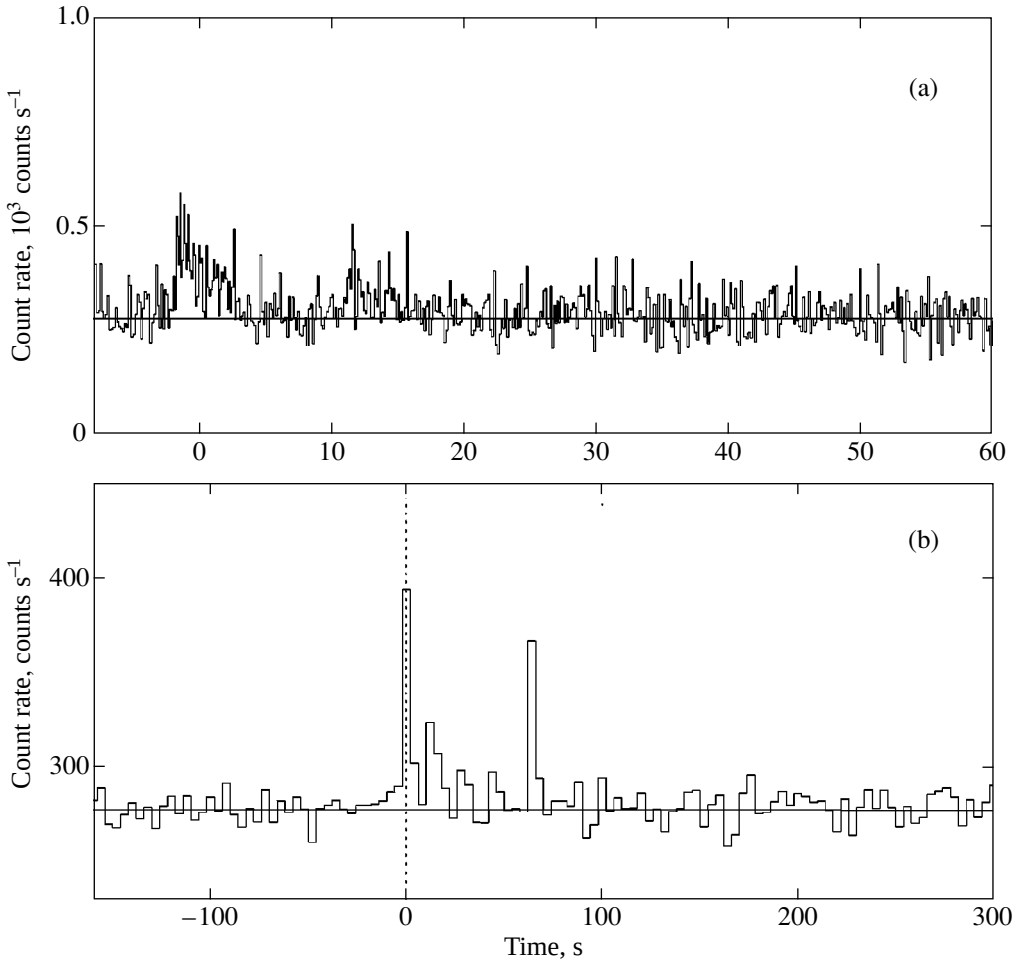

Fig. 7.

no cosmological effects producing a turnover in the count-rate curve show up. The fact that the field of view varies with sensitivity does not prevent this conclusion from being reached. The reason is that, for a uniform distribution of sources, the dependence on sensitivity can be integrated separately, much like the source luminosity function [18], and cannot distort the –3/2 power law. Deviations from this law are observed for weaker

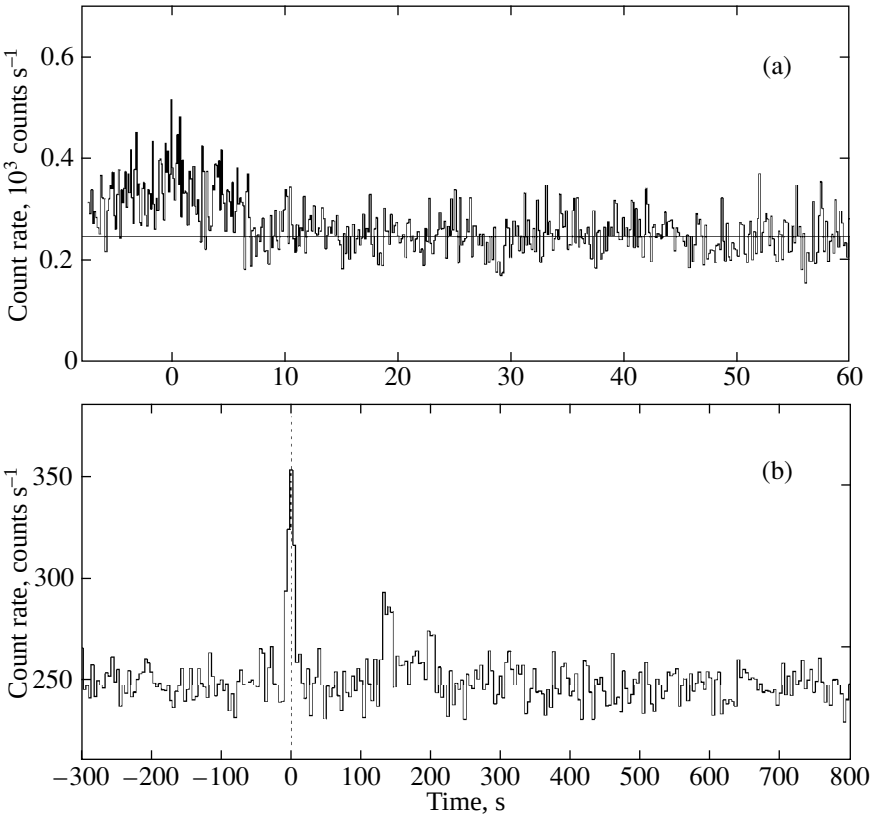
(a)
Count rate, 10^3 counts s^{-1}
0.6
0.4
0.2
0
0
10
20
30
40
50
60
(b)
Count rate, counts s^{-1}
350
300
250
−300
−200
−100
0
100
200
300
400
500
600
700
800
Time, s

Fig. 8.

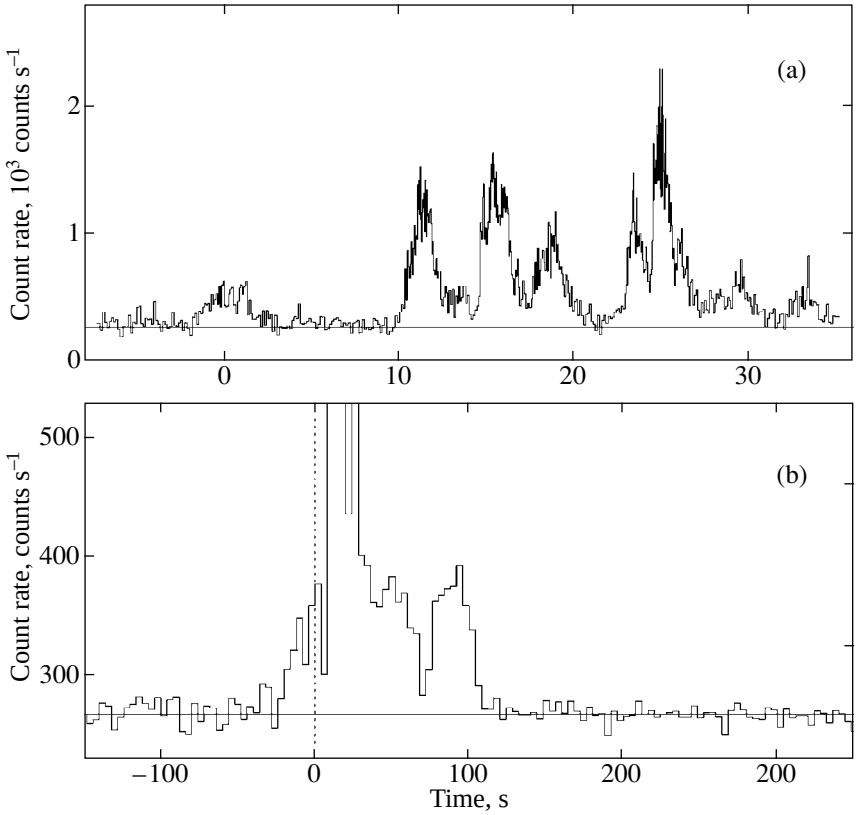
(a)
Count rate, 10^3 counts s^{-1}
2
1
0
0
10
20
30
(b)
Count rate, counts s^{-1}
500
400
300
−100
0
100
200
200
Time, s

Fig. 9.

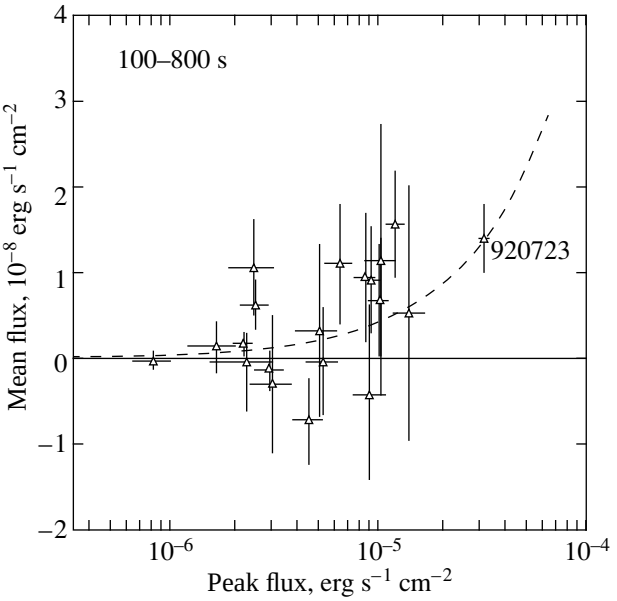

Fig. 10. Mean count rates in the 35–300-keV energy band in the time interval 100–800 s after burst-cell triggering versus burst peak count rates.

bursts with peak fluxes $\lesssim 3 \times 10^{-6}$ erg s^{-1} cm^{-2} (see [13]).

Figures 3–9 show time histories of the detected GRBs in the 35–300-keV energy band. Time histories of the GRBs 900327, 900720, and 910122 are shown separately in Figs. 7–9 on different time scales, because their duration is longer than the duration of data recording with good time resolution.

The Granat spacecraft is in a high-apogee orbit and is not affected by the Earth's radiation belts and other magnetospheric irregularities (such as the South Atlantic Anomaly) during observations. The SIGMA background generally exhibits no appreciable variability on time scales of 10^3 s, which makes it possible to study the persistent emission from GRBs. The time history of the brightest GRB 920723 was studied in detail in [19]. An afterglow was detected after the main burst that lasted ~6 s, whose flux fell off as $\sim t^{-0.7}$ for at least 1000 s. Here, we present the results of our search for early afterglows of other GRBs detected by the SIGMA main detector.

In Fig. 10, mean (35–300 keV) fluxes in the time interval 100–800 s after the burst cell triggering are plotted against burst peak fluxes. The background was fitted by Chebyshev polynomials, much as was done in [19]. Some bursts for which we could not qualitatively fit the background were not considered. There were ten such bursts. The definitely long bursts 900720 and 910122 (Figs. 8 and 9) are not shown in Fig. 10 either. The inclined curve shows a linear relation that passes through the extreme right point corresponding to the afterglow of GRB 920723. The coefficients for converting counts into energy units for each burst were determined by using the burst fluxes measured by the PHEBUS instrument. The related systematic error is ~30%. It was not included in the errors in Fig. 10, because it did not affect the significance of recording the flux.

The burst-averaged flux in the time interval 100–800 s is 0.36 ± 0.14 counts s^{-1}. This value was obtained by averaging the flux over all bursts except GRB 920723 and the definitely long GRBs 900720 and 910122 (Figs. 8 and 9). This count rate approximately corresponds to 3×10^{-9} erg s^{-1} cm^{-2}, which accounts for about 10^{-3} of the flux recorded during bursts. The fact that the mean flux is nonzero at a confidence level higher than 95% may be evidence for the presence of soft gamma-ray emission on a time scale of 1000 s after a considerable number of GRBs.

ACKNOWLEDGMENTS

This study was supported by the Russian Foundation for Basic Research (project nos. 96-15-96930 and 97-02-17693).

REFERENCES

1. J. Paul, P. Mandrou, J. Ballet, *et al.*, Adv. Space Res. **11**, 289 (1991).
2. A. Claret, F. Lebrun, P. Laurent, and J. P. Leray, Astron. Astrophys. **282**, 1034 (1994).
3. R. A. Sunyaev, M. R. Gilfanov, E. M. Churazov, *et al.*, Astrophys. J. **402**, 579 (1993).
4. O. V. Terekhov, A. V. Kuznetsov, K. Barat, Z. Vedrenn, and M. Niel', *Scientific Instrumentation for Space Studies (A89-14726 03-19)* (Nauka, Moscow, 1987), p. 140.
5. O. V. Terekhov, D. V. Denisenko, V. A. Lobachev, *et al.*, Pis'ma Astron. Zh. **20**, 323 (1994) [Astron. Lett. **20**, 265 (1994)].
6. O. V. Terekhov, D. V. Denisenko, V. A. Lobachev, *et al.*, Pis'ma Astron. Zh. **21**, 83 (1995) [Astron. Lett. **21**, 73 (1995)].
7. A. Yu. Tkachenko, O. V. Terekhov, R. A. Sunyaev, *et al.*, Pis'ma Astron. Zh. **24**, 833 (1998) [Astron. Lett. **24**, 722 (1998)].
8. O. V. Terekhov, V. A. Lobachev, D. V. Denisenko, *et al.*, Pis'ma Astron. Zh. **19**, 686 (1993) [Astron. Lett. **19**, 276 (1993)].
9. A. Claret, F. Lebrun, J. Paul, *et al.*, Astron. Astrophys. **287**, 824 (1994).
10. A. Goldwurm, S. Gaertner, E. Churazov, and M. Gilfanov, IAU Circ., No. 5932 (1994).
11. S. Yu. Sazonov, R. A. Sunyaev, O. V. Terekhov, *et al.*, Astron. Astrophys., Suppl. Ser. **129**, 1 (1998).
12. C. A. Meegan, G. N. Pendleton, M. S. Briggs, *et al.*, Astrophys. J., Suppl. Ser. **106**, 65 (1996).
13. G. J. Fishman and C. A. Meegan, Ann. Rev. Astron. Astrophys. **33**, 415 (1995).
14. O. V. Terekhov, A. G. Kuzmin, R. A. Sunyaev, *et al.*, Pis'ma Astron. Zh. **22**, 403 (1996) [Astron. Lett. **22**, 362 (1996)].

15. J.-P. Dezalay, C. Barat, R. Talon, *et al.*, in *Proceedings of 1st Huntsville Gamma-Ray Bursts Symposium, 1991*, Ed. by W. S. Paciesas and G. J. Fishman (AIP Conf. Proc., New York, 1991), p. 265.
16. J.-P. Dezalay, J. P. Lestrade, C. Barat, *et al.*, Astrophys. J. Lett. **471**, L27 (1996).
17. M. Tavani, Astrophys. J. Lett. **497**, L21 (1998); astro-ph/9802192.
18. Ya. B. Zel'dovich and I. D. Novikov, *Structure and Evolution of the Universe* (Nauka, Moscow, 1975), p. 87.
19. R. A. Burenin, A. A. Vikhlinin, O. V. Terekhov, *et al.*, Pis'ma Astron. Zh. **25**, 483 (1999) [Astron. Lett. **25**, 411 (1999)].

Translated by A. Dambis

Astronomy Letters, Vol. 26, No. 7, 2000, pp. 423–427. Translated from Pis'ma v Astronomicheskiĭ Zhurnal, Vol. 26, No. 7, 2000, pp. 493–498.

The Radio Galaxy RC J1148+0455

Yu. N. Pariĭskiĭ[1], N. S. Soboleva[1], A. I. Kopylov[1], O. V. Verkhodanov[1]*, A. V. Temirova[1], O. P. Zhelenkova[1], J. Winn[2], A. Fletcher[2], and B. Burke[2]

[1] *Special Astrophysical Observatory, Russian Academy of Sciences, Nizhniĭ Arkhyz, Karachaevo-Cherkessiya, 369167 Russia*
[2] *Massachusetts Institute of Technology, USA*

Received September 15, 1999

Abstract—Based on data from the MIT–GB–VLA 4850-MHz survey, we investigate the radio structure of RC J1148+0455 with a steep radio spectrum ($\alpha = -1.04$) from the COLD catalog. The radio source consists of two components, each having a complex structure. We analyze an optical identification of the source by using 6-m telescope images. The centroid of the radio source falls on a group of eight galaxies at a 24^m level in *R*. © *2000 MAIK "Nauka/Interperiodica"*.

Key words: *radio galaxies*

INTRODUCTION

Any search for distant radio galaxies suggests the selection of candidates by several parameters [1], including the presence of a steep spectrum and a two-component FRII-type radio structure [2]. About 100 such objects were selected from the COLD catalog (RC), which was compiled from RATAN-600 observations [3, 4] by using VLA data. Most of them are identified with galaxies to $24–25^m$ in *R*, as shown by the "Large Trio" observations with the 6-m Special Astrophysical Observatory telescope [5, 6]. VLA observations of objects from the MIT–GB survey [7] were also used to elucidate the structure of radio sources; the region surveyed overlaps with the COLD-survey zone. Detailed high-resolution maps were obtained for 69 RC objects from MIT–GB–VLA data [8].

Here, we investigate the nature of the radio source RC J1148+0455 (RC B1146+052) from the COLD catalog by using MIT–GB–VLA maps, which show a complex structure of its radio components, and observations with the 6-m Special Astrophysical Observatory telescope.

RADIO SPECTRUM

RC J1148+0455 also has radio identifications with objects from the 4C catalog [9] (4C+05.53) and the Parkes catalog [10] (PKS B1146+052). The spectrum of RC J1148+0455 is shown in Fig. 1.

Based on refined positions of decameter radio sources from the UTR catalog [11], Verkhodanov *et al.* [12] managed to extend the spectra of many radio sources to low frequencies. RC J1148+0455 is also identified with GR 1147+05, an object from the decameter catalog. The spectral index α_i determined by least-squares linear fitting of the radio source's spectrum from the centimeter to decameter bands using the CATS database [13] is –1.04 ($S \sim \nu^{\alpha_i}$), which allows this spectrum to be classified as ultrasteep. It should be noted that the curve $y = 2.597 - 0.664x - 0.066x^2$, where y is log$S$ (S is the flux density in Jy) and x is logν (ν is the frequency in MHz), provides the best fit with a minimum of the squares of the residuals. When constructing the spectrum, we used both data from the COLD catalog (marked in Fig. 1 by downward-directed filled

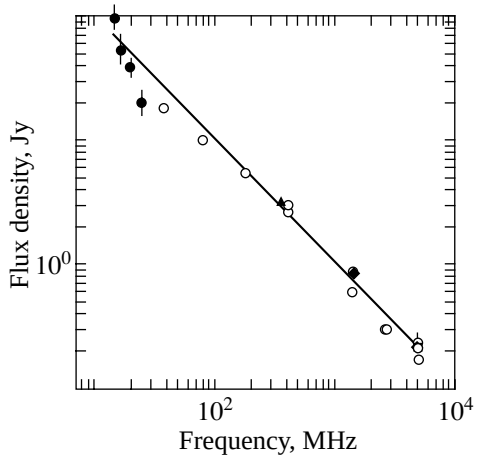

Fig. 1. The spectrum of RC J1148+0455. The COLD data points are marked by downward-directed filled triangles (the frequencies are 2300, 3900, 7700, and 11200 MHz); the UTR data points are indicated by filled circles (14.7, 16.7, 20, 25 MHz), the Texas and NVSS points are indicated by an upward-directed filled triangle (365 MHz) and a filled diamond (1400 MHz), respectively.

* E-mail address for contacts: vo@sao.ru

triangles) and data from other catalogs, which were obtained by means of the *match* problem in the CATS database and are given in Table 1. The columns of this table give, respectively, right ascensions α of the radio source (hours, minutes, seconds) for epoch 1950.0; right-ascension errors $\Delta\alpha$ (in seconds), if available; declinations δ (degrees, arcminutes, arcseconds) for epoch 1950.0; declination errors $\Delta\delta$ (in arcseconds), if available; frequencies ν (in MHz); flux densities S (in Jy); flux-density errors ΔS (in Jy), if available; and catalog names. The following references were used as the catalog names: UTR [11]; MSL (Master List), Dixon's combined catalog of radio sources [14], the 43rd version of 1981; CUL [15, 16]; 4C [9]; TXS [17]; RH74 [18]; MRC [19]; COLD [3, 4]; PKS90 [10]; Z2 [20, 21]; Z2–95 [22]; 87GB [23]; GB6 [24]; PMN [25]; MITG [7]; and NVSS [26].

We attribute the sharp fall of the spectrum at decameter flux densities to an underestimation of the values in this wavelength range. One should also take into account the fact that, when using the MIT–GB–VLA data to construct the spectrum, we disregarded the extent of the structure invisible with the VLA in the A configuration at a wavelength of 6 cm.

STRUCTURE OF THE RADIO SOURCE

We investigated the structure of the radio source by using VLA data stored at the Massachusetts Institute of Technology as archival FITS files of the MIT–GB–VLA survey. The image resolution is $0\farcs5$ at 4850 MHz in the A configuration.

Figure 2 shows a VLA map of RC J1148+0455; detailed maps of components A and B are shown in Figs. 3 and 4, respectively. Component A has a curved structure and was previously classified [1, 27] as a double independent radio source. Component B has a complex structure with three peaks. If this component is not

Table 1. Positions and flux densities from various surveys for the radio source RC J1148+0455

α(B1950.0)	$\Delta\alpha$	δ(B1950.0)	$\Delta\delta$	ν, MHz	S, Jy	ΔS, Jy	Catalog
$11^h47^m00^s$	17^s	+05°39′36″	396″	14.7	95	21.85	UTR
11 47 10	18	+05 42 36	216	16.7	53	14.84	UTR
11 47 10	10	+05 27 00	180	20	38	6.84	UTR
11 47 50	13	+05 34 48	396	25	20	5.4	UTR
11 46 13		+05 13 00		38	18		MSL
11 46 09.5		+05 12 02		80	11		CUL
11 46 13		+05 13 00		81.5	16.6		RH74
11 46 09.5		+05 12 02		160	5.9		CUL
11 46 13		+05 13 00		178	5.5		4C
11 46 13.632	0.032	+05 12 06.57	0.20	365	3.262	.069	TXS
11 46 13.301	0.2	+05 11 53	5	408	2.65	.12	MRC
11 46 17		+05 12 24		408	3		MSL
11 46 13.6		+05 12 06.5		960	.932	.08	COLD
11 46 13.433	0.03	+05 12 08.10	0.56	1400	.8291	.0263	NVSS
11 46 13.7		+05 11 34		1400	.87		WB92
11 46 14.3		+05 12 03		1410	.6		PKS90
11 46 13.6		+05 12 06.5		2300	.413	.033	COLD
11 46 14.3		+05 12 03		2700	.3		PKS90
11 46 13.6		+05 12 06.5		3900	.205	.008	COLD
11 46 13.6		+05 12 06.6		3900	.181	.019	Z2
11 46 13.88	0.07	+05 12 24	5	3900	.233	.012	COLD
11 46 13.6		+05 12 07		3900	.217		Z2–95
11 46 13.28		+05 15 36		3900	.2		Z2
11 46 13.6		+05 12 06.6		4800	.169	.011	Z2
11 46 13.6	0.9	+05 11 35	18	4850	.265	.034	87GB
11 46 13.723		+05 12 05.5		4850	.217	.015	PMN
11 46 13.725	0.5	+05 11 58.5	9	4850	.238	.02	GB6
11 46 14.4		+05 12 09		4850	.163		MITG
11 46 14.3		+05 12 03		5000	.18		PKS90
11 46 13.6		+05 12 06.6		7500	.133	.018	Z2
11 46 13.6		+05 12 07		7500	.1		Z2–95
11 46 13.6		+05 12 06.5		7700	.074	.011	COLD
11 46 13.6		+05 12 06.5		11200	.046	.003	COLD
11 46 13.6		+05 12 06.5		11200	.084	.031	Z2

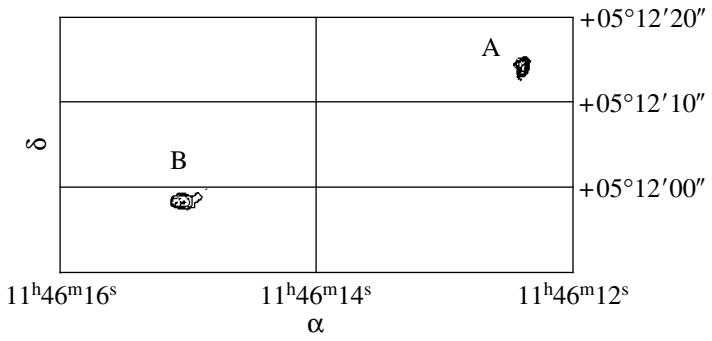

Fig. 2. The two-component structure of RC J1148+0455. The positions are given for epoch B1950.0.

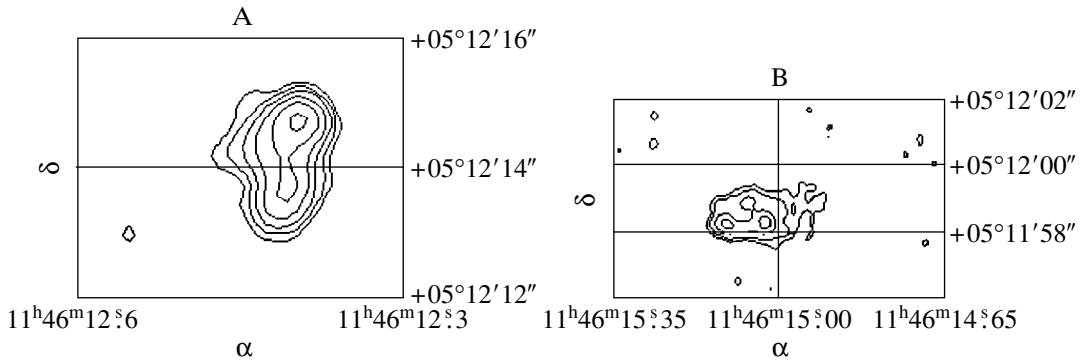

Fig. 3. The structure of the components of RC J1148+0455. The positions are given for epoch B1950.0.

associated with component A, then it could be considered as a candidate for a gravitational lens [28]. This is unlikely, because there are no optical objects brighter than $R = 25^m$ near this component. Positions of the peaks for components A and B and the total brightness distribution over the entire object A+B for epochs B1950.0 and J2000.0, as well as the corresponding flux densities (peak S_{peak} and total S_{tot} ones) at 4850 MHz, are given in Table 2.

The total flux was calculated in a region that included both components with the background subtracted. The separation between the components is 43″.8.

Positions and flux densities from the 87GB [23], GB6 [24], and NVSS [26] catalogs (see Table 1) can be used for comparison with our data. The beam size was 3′.5 in the 87GB and GB6 surveys, 45″ in the NVSS survey, and 54″ in the Texas survey. The above data are in good agreement with the results of MIT–VLA data reduction.

OPTICAL IDENTIFICATION

Figure 4 shows the isophotes of RC J1148+0455 that were constructed from the MIT–GB–VLA data; they were superimposed on the optical image obtained by reducing the *R* observations with the 6-m Special Astrophysical Observatory telescope. The exposure time was 400 s at 1″.5 seeing.

The centroid of the radio source falls on a group of eight galaxies at a 24^m level in *R*. The bright compact

Table 2. Characteristics of the components of RC J1148+0455

Radio component	α(B1950.0)	δ(B1950.0)	α(J2000.0)	δ(J2000.0)	S_{peak}, mJy beam^{-1}	S_{tot}, mJy
A	11h46m12s.38	+05°12′14″.8	11h48m46s.48	+04°55′34″.2	28.4	166
B	11 46 15.07	+05 11 58.6	11 48 49.16	+04 55 17.9	–	96
B2	11 46 15.03	+05 11 58.4	11 48 49.12	+04 55 17.8	5.7	–
B1	11 46 15.06	+05 11 58.9	11 48 49.16	+04 55 18.3	4.3	–
B3	11 46 15.10	+05 11 58.3	11 48 49.19	+04 55 17.7	6.2	–
A+B	11 46 13.37	+05 12 07.6	11 48 47.46	+04 55 27.0	–	263

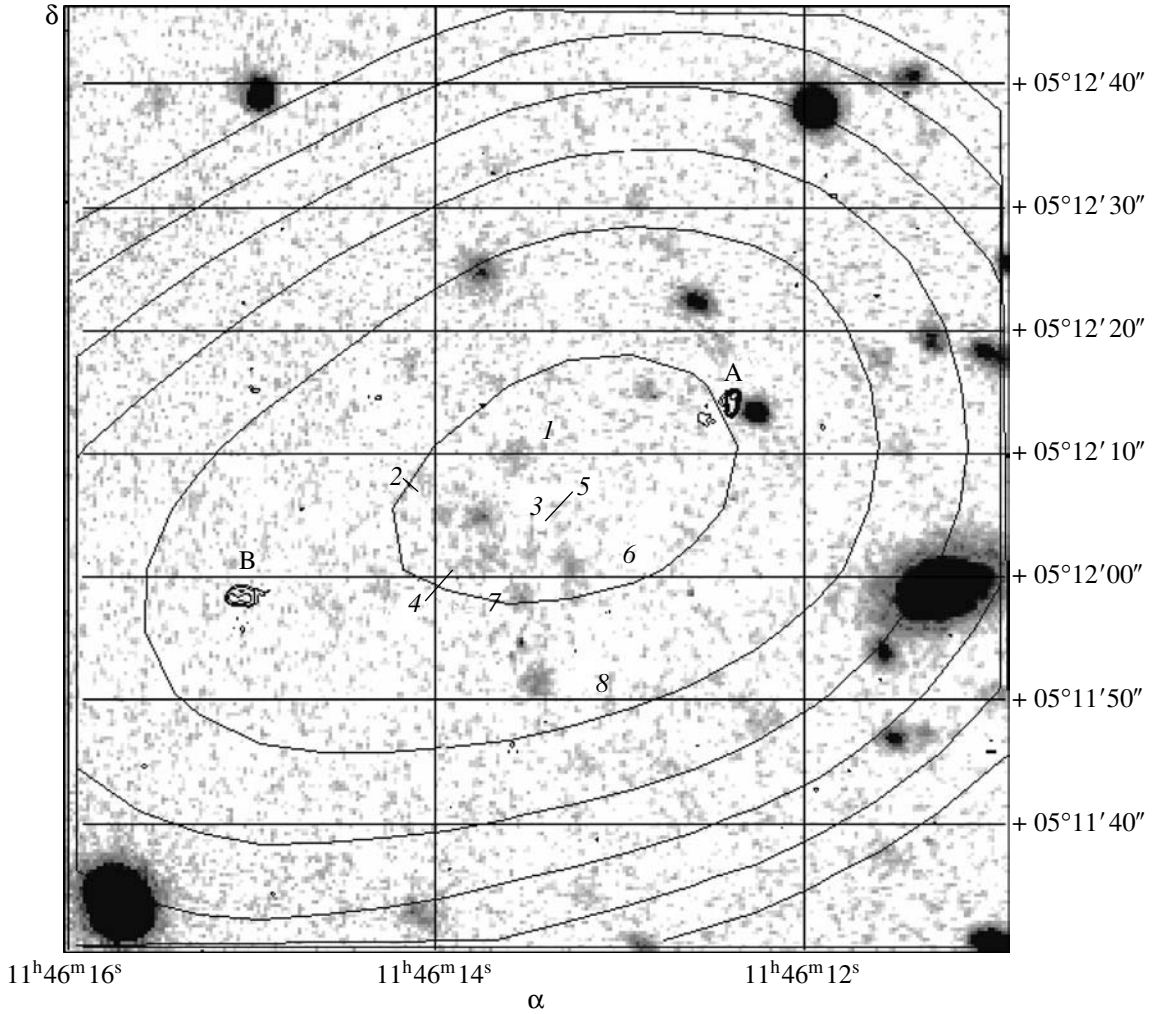

Fig. 4. The isophotes of RC J1148+0455 constructed from MIT–GB–VLA 4850 MHz and from NVSS data at 1400 MHz and superposed on the optical *R* image of this source obtained with the 6-m Special Astrophysical Observatory telescope. The isophotes were constructed with a factor of 2 at 4850 MHz (contours A and B) of the 1 mJy beam^{-1} level and at 1400 MHz of the 80 mJy beam^{-1} level. The positions are given for epoch B1950.0.

galaxy from the group (no. 3) lies on the axis connecting both components. It has an *R* magnitude of $23^m.2 \pm 0^m.2$ through a 3″ aperture and is the most likely candidate for an optical identification.

Table 3. Positions and magnitudes of the galaxies in the group

Number	α(B1950.0)	δ(B1950.0)	*R*
1	$11^h46^m13^s.58$	+5°12′10″.2	$23^m.8$
2	11 46 13.96	+5 12 05.3	24.3
3	11 46 13.77	+5 12 04.9	23.2
4	11 46 13.73	+5 12 01.9	23.7
5	11 46 13.48	+5 12 01.9	24.4
6	11 46 13.27	+5 12 00.1	23.7
7	11 46 13.55	+5 11 58.3	23.6
8	11 46 13.45	+5 11 51.7	23.1

Some characteristics of the galaxies are given in Table 3.

DISCUSSION

Based on the above data, we may conclude that RC J1148+0455 is a two-component FRII-type radio source.

The parent galaxy of the radio source probably belongs to the group (Table 3). The curved shape of component A can be explained by the interaction with the ambient medium, while the close location of the galaxy with coordinates J114846.34+045532.9 and magnitude $R = 21^m.6$ is a chance projection. The shape of component B (the arrangement of three "hot spots") can be explained in terms of the jet rotation model, or this shape resulted from the jet interaction with the ambient medium.

ACKNOWLEDGMENTS

This study was supported in part by the Russian Foundation for Basic Research (project nos. 99-07-90334 and 99-02-17114), as well as the Federal Program "Astronomy" (project nos. 1.2.1.2 and 1.2.2.4) and the Federal Program "Integration" (project no. 578).

REFERENCES

1. Yu. N. Parijskij, W. M. Goss, A. I. Kopylov, *et al.*, Bull SAO, No. 40 (1996), p. 5.
2. B. L. Fanaroff and J. M. Riley, Mon. Not. R. Astron. Soc. **167**, 31 (1974).
3. Yu. N. Parijskij, N. N. Bursov, N. M. Lipovka, *et al.*, Astron. Astrophys., Suppl. Ser. **87**, 1 (1991).
4. Yu. N. Parijskij, N. N. Bursov, N. M. Lipovka, *et al.*, Astron. Astrophys., Suppl. Ser. **96**, 583 (1992).
5. A. I. Kopylov, W. M. Goss, Yu. N. Pariiskii, *et al.*, Astron. Zh. **72**, 613 (1995).
6. Yu. N. Pariiskii, W. M. Goss, A. I. Kopylov, *et al.*, Astron. Zh. **75**, 483 (1998).
7. C. Bennett, B. Burke, J. Hewitt, *et al.*, Astrophys. J., Suppl. Ser. **61**, 1 (1986).
8. A. Fletcher, S. Conner, F. Crawford, *et al.*, Astron. Zh. **73**, 835 (1996).
9. J. D. H. Pilkington and P. F. Scott, Mem. R. Astron. Soc. **69**, 183 (1965).
10. R. E. Otrupcek and A. E. Wright, Proc. Astron. Soc. Austral. **951**, 170 (1991).
11. S. Ia. Braude, A. V. Megn, K. P. Sokolov, and N. K. Sharykin, Astrophys. Space Sci. **64**, 127 (1979).
12. O. V. Verkhodanov, H. Andernach, N. V. Verkhodanova, and N. Loiseau, *Proc. "Observational Cosmology with the New Radio Surveys,"* Ed. by M. Bremer, N. Jackson, and I. Pérez-Fournon (Astrophysics Space Sci. Library, Kluwer, 1998), Vol. 226, p. 255.
13. O. V. Verkhodanov, S. A. Trushkin, H. Andernach, and V. N. Chernenkov, *Astronomical Data Analysis Software and Systems VI*, Ed. by G. Hunt and H. E. Payne, ASP Conf. Ser. **125**, 322 (1997).
14. R. S. Dixon, Astrophys. J., Suppl. Ser. **20**, 1 (1970).
15. O. B. Slee and C. S. Higgins, Aust. J. Phys. Astrophys. Suppl., No. 27, 1 (1973).
16. O. B. Slee, Aust. J. Phys. Astrophys. Suppl., No. 43, 1 (1977).
17. J. N. Douglas, F. N. Bash, F. A. Bozyan, *et al.*, Astron. J. **111**, 1945 (1996).
18. A. C. S. Readhead and A. Hewish, Mem. R. Astron. Soc. **78**, 1 (1974).
19. M. I. Large, L. E. Cram, and A. M. Brugess, Observatory **111**, 72 (1991).
20. V. R. Amirkhanyan, A. G. Gorshkov, M. G. Larionov, *et al., The Zelenchuk Survey of Radio Sources between Declinations 0° and 14°* (Moscow State Univ., Moscow, 1989).
21. V. R. Amirkhanyan, A. G. Gorshkov, and V. K. Konnikova, Astron. Zh. **69**, 225 (1992).
22. A. G. Gorshkov and V. K. Konnikova, Astron. Zh. **72**, 291 (1995).
23. P. C. Gregory and J. J. Condon, Astrophys. J., Suppl. Ser. **75**, 1011 (1991).
24. P. C. Gregory, W. K. Scott, K. Douglas, and J. J. Condon, Astrophys. J., Suppl. Ser. **103**, 427 (1996).
25. M. R. Griffith and A. E. Wright, Astron. J. **105**, 1666 (1993).
26. J. J. Condon, W. D. Cotton, E. W. Greisen, *et al.*, Astron. J. **115**, 1693 (1998).
27. C. W. Lawrence, C. L. Bennett, J. N. Hewitt, *et al.*, Astrophys. J., Suppl. Ser. **61**, 105 (1986).
28. A. Fletcher, *Ph.D. Thesis* (Massachusetts Inst. Techn., Boston, USA, 1998).

Translated by V. Astakhov

Astronomy Letters, Vol. 26, No. 7, 2000, pp. 428–432. Translated from Pis'ma v Astronomicheskiĭ Zhurnal, Vol. 26, No. 7, 2000, pp. 499–503.

Prospects for Detecting Light Echoes of Galactic Supernovae by Wide-Angle Polarimetry

I. A. Maslov*

Space Research Institute, Russian Academy of Sciences, Profsoyuznaya ul. 84/32, Moscow, 117810 Russia

Received August 18, 1999

Abstract—We propose to use a global (wide-angle, of the order of several degrees) distribution of linearly polarized emission over the sky to detect light echoes of historical supernovae exploded in our Galaxy. The echo emission must be polarized tangential to the direction of the supernova explosion site, and its degree of polarization must exhibit a characteristic dependence on angular distance. The near infrared is an optimum spectral range for detection. A spotted structure in the shape of a ring ~5° in diameter and ~3° in width with a total brightness of ~12–13^m in polarized light with a tangential orientation of the electric vector must be currently seen in the direction where Tycho Brahe observed a supernova explosion in 1572. A comparison of the expected intensity of the echo with the intensities of the zodiacal light and the atmosphere shows that it can be detected in principle during long-term observations from space and, under favorable conditions, even from the ground.

Key words: *supernova remnants, polarization, light echoes*

INTRODUCTION

In Shklovsky's book entitled "Supernovae and Related Problems" [1], the very first formula (1.1) refers to the intensity of the light echo which can be seen on the nebula that reflected the light from a supernova (SN) exploded in our Galaxy several hundred years ago. To separate the weak emission arising when the light from the central source is scattered in the surrounding shell, Sholomitskiĭ [2] proposed to use the fact that this emission has a high degree of linear polarization with a well-known, tangential orientation of the electric vector. Regarding the search for SN echoes, these authors suggested a search for clouds with distinctive properties, from which it could be determined that the light from them was the reflection (scattering) of light from a previously exploded supernova. However, the light from the SN within several hundred years after its explosion has traveled father than 100 pc, and one might expect the interstellar medium on this scale, with a high probability, to be not empty and to have a mean density and, consequently, a scattering coefficient similar to their mean values for the Galaxy (near its plane, because SNe exploded there). Given that the light is significantly polarized (up to 100% for Rayleigh scattering at an angle of 90°) when scattered by interstellar dust and that the electric vector of polarization is perpendicular to the source direction, it seems appropriate to search for an echo in the overall distribution of linearly polarized light around the location where the SN was observed. If individual bright spots (scattering clouds or breaks in interstellar clouds) with suitable polarization were detected in this distribution, then they could subsequently be thoroughly studied. Besides, the brightness of these spots can (and must) be variable on times scales of several years, because the light echo propagates through relatively small-scale (~1 pc) density fluctuations in the interstellar medium. At the same time, the overall observed distribution must be more or less stationary (some spots fade, others flare up), and this gives hope that a long-term study of the sky distribution of polarized emission (a regular polarization sky survey) will reveal a SN echo against the zodiacal-light and atmospheric background.

ECHO INTENSITY

Assuming a single scattering, let us calculate the angular intensity distribution of the linearly polarized emission produced by the scattering of SN light by dust in the Galaxy. Below, we write Shklovsky's approximate formula [1] for the echo intensity in a more accurate form. Let the SN be at distance z from us, and its explosion was observed on Earth t years ago. The locus from which the light echo is currently observed is then the surface of an ellipsoid of revolution with the foci at the SN and at the Earth (Fig. 1), with

$$r + R = z + ct, \tag{1}$$

where r and R are the distances from the scattering point to the SN and the Earth, respectively; and $c \approx 0.3$ pc yr^{-1} is the speed of light. If the observations are

* E-mail address for contacts: imaslov@iki.rssi.ru

carried out at angle ω to the direction of the exploded SN, then the distance from the Earth to the scattering point is

$$R = \frac{ct}{2}\frac{z + ct/2}{z\sin^2(\omega/2) + ct/2}, \quad (2)$$

and the thickness from which the scattered light simultaneously comes is proportional to the explosion duration Δt:

$$\Delta R = \frac{dR}{dt}\Delta t = \frac{c\Delta t}{2}\left\{1 + \left(\frac{\sin(\omega/2)\cos(\omega/2)z}{z\sin^2(\omega/2) + ct/2}\right)^2\right\}. \quad (3)$$

The echo intensity (the flux on Earth per unit solid angle of the echo) is

$$\begin{aligned} B &= \frac{L}{r^2}\exp(-\tau_e r)\tau_s \Delta R\Phi(\alpha)\exp(-\tau_e R) \\ &= \frac{L}{(z + ct - R)^2}\exp(-\tau_e(z + ct))\tau_s \Delta R\Phi(\alpha), \end{aligned} \quad (4)$$

where L is the mean SN luminosity during the explosion; τ_s and τ_e are the volume coefficients of interstellar scattering and interstellar extinction, respectively; and $\Phi(\alpha)$ is the scattering phase function. The scattering angle α can be determined from the formula

$$\tan\alpha = \frac{z\sin\omega}{z\cos\omega - R}. \quad (5)$$

For convenience, let us write the intensity (4) as the equivalent number of stars of the mth magnitude from a square degree of the sky:

$$\begin{aligned} B_m &= \left(\frac{\pi}{180}\right)^2\left(\frac{10\text{ pc}}{z + ct - R}\right)^2\tau_s \\ &\times \exp(-\tau_e(z + ct))\Delta R\Phi(\alpha)10^{0.4(m-M)}, \end{aligned} \quad (6)$$

where M is the absolute magnitude of the SN during its explosion. Multiplying the intensity from equation (6) by the degree of linear polarization $P(\alpha)$ yields the tangentially polarized echo intensity

$$Q_m = B_m P(\alpha). \quad (7)$$

In the visible and in the near infrared,

$$\tau_s \approx \tau_e \approx \frac{A_V}{1.086^m}\frac{0.55\ \mu\text{m}}{\lambda}, \quad (8)$$

where A_V is the interstellar extinction coefficient near the Galactic plane (approximately $1–2^m$ kpc^{-1}). It follows from (6) that the echo intensity for $\tau_s = \tau_e = \tau$ is at a maximum in the spectral range where $\tau(z + ct) \approx 1$, i.e., in the infrared, if the distance to the SN is a few kpc. Note also that if the echo intensity is averaged over a fairly large angular area in (4) and (6), $\tau_s\exp(\tau_e(z + ct))$ must be replaced by its mean $\langle\tau_s\exp(-\tau_e(z + ct))\rangle \approx \langle\tau_s\rangle\langle\exp(-\tau_e(z + ct))\rangle$. If the extinction coefficient varies within this area, then substituting its mean value in the formulas causes the echo intensity to be underestimated, because $\langle\exp(-\tau_e(z + ct))\rangle \geq \exp(-\langle\tau_e\rangle(z + ct))$.

AN ESTIMATE FOR TYCHO BRAHE'S SN

The computed angular distributions of echo intensity $B_m(\omega)$ and tangentially polarized intensity $Q_m(\omega)$ for Tycho Brahe's SN (1572) are shown in Figs. 2 and 3. The distance to the SN was assumed to be 3 kpc [3], its absolute magnitude was $M = -19^m$, and the equivalent explosion duration was 15 days. In the visible (λ = 0.55 μm) and in the near infrared (λ = 1 μm), we used the empirical scattering phase function

$$\begin{aligned} \Phi(\alpha) &= \frac{g_2 - g}{g_2 - g_1}\frac{1 - g_1^2}{(1 + g_1^2 - 2g_1\cos\alpha)^{3/2}} \\ &+ \frac{g - g_1}{g_2 - g_1}\frac{1 - g_2^2}{(1 + g_2^2 - 2g_2\cos\alpha)^{3/2}} \end{aligned} \quad (9)$$

and the degree of polarization

$$P(\alpha) = \begin{cases} p\dfrac{\sin^2\alpha}{1 + \cos^2\alpha} + b\left(1 - \dfrac{|\alpha - 145^\circ|}{35^\circ}\right), \\ |\alpha - 145^\circ| < 35^\circ \\ p\dfrac{\sin^2\alpha}{1 + \cos^2\alpha}, \quad |\alpha - 145^\circ| \geq 35^\circ, \end{cases} \quad (10)$$

with the parameters (see the table) calculated by White [4] for the dust mixture that was proposed by Mathis *et al.* [5] as satisfactorily fitting the interstellar extinction law. For λ = 2.5 μm, we used the Rayleigh scattering phase function

$$\Phi(\alpha) = \frac{3}{4}(1 + \cos^2\alpha) \quad (11)$$

and the degree of polarization

$$P(\alpha) = \frac{\sin^2\alpha}{1 + \cos^2\alpha}. \quad (12)$$

We performed our calculations for two interstellar extinction coefficients: the Galaxy-averaged one, $A_V = 1\overset{m}{.}9$ kpc^{-1} [6], and the mean one toward Cassiopeia, $A_V = 0.8^m$ kpc^{-1} [7, 8]. The second value agrees with the magnitude of Tycho Brahe's SN at maximum $m_V \approx -4^m$

Parameters of the scattering phase function

λ, μm	g	g_1	g_2	p	b
0.55	0.47	−0.52	0.51	0.38	0.05
1.0	0.23	−0.39	0.34	0.77	−0.035

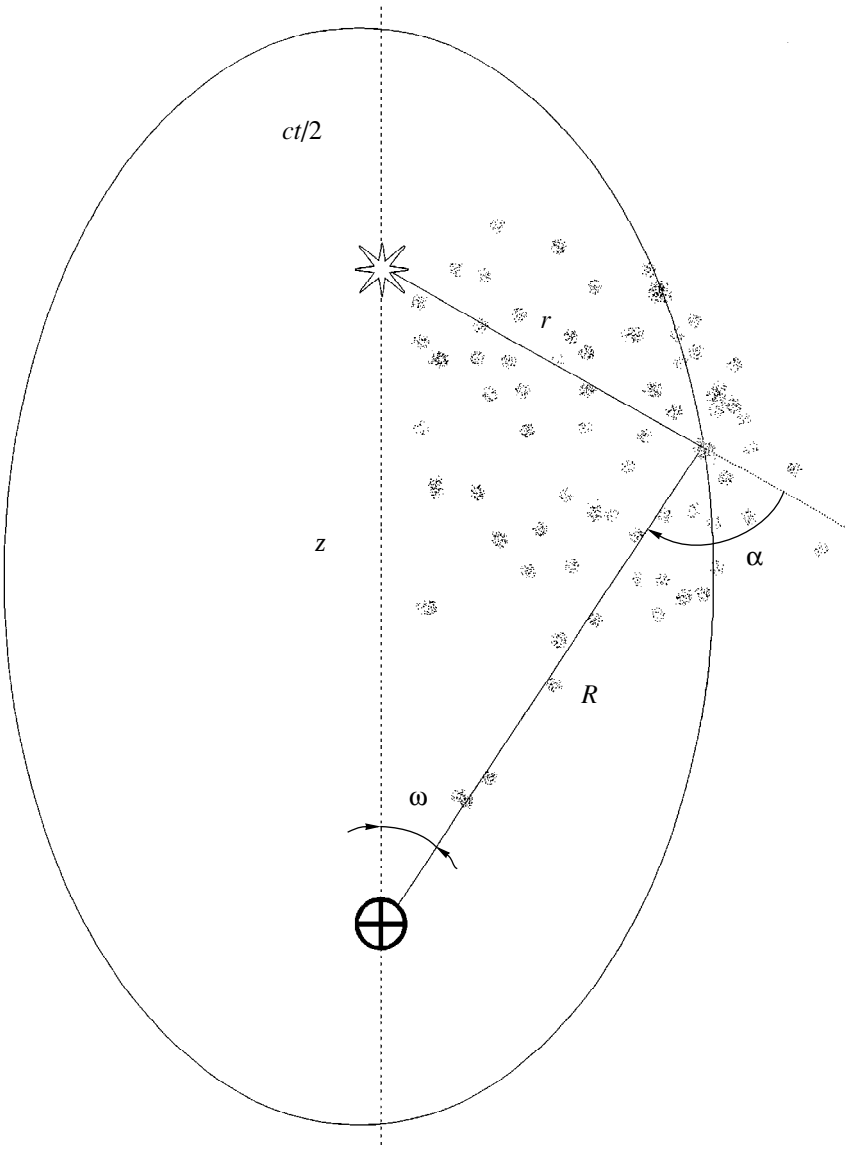

Fig. 1. A scheme for the scattering of SN light by the interstellar medium.

[9] and with its absolute magnitude $M = -19^m$ for the assumed distance of 3 kpc.

The echo intensity (Fig. 2) is at a maximum toward the SN. Because of the strong wavelength dependence of the scattering phase function, this intensity decreases with angular distance differently for different spectral regions. The tangentially polarized echo intensity for Tycho Brahe's SN (Fig. 3) must be at a maximum at an angular distance of 2°–3°. For a homogeneous medium, the pattern for tangentially polarized light would have the shape of a ring ~5° in diameter and ~3° in width.

Since the interstellar medium is highly inhomogeneous, a spotted structure, which generally preserves the above angular dependences of intensity and polarization, must be observed. The total brightness obtained by integrating the tangentially polarized echo intensity in the ring $1° < \omega < 4°$ is $\sim 12^m$ in the infrared and 13^m in *V*.

The visible intensity of the zodiacal light far from the ecliptic is approximately $2 \times 10^4\ S_{15}$ (S_{15} is the equivalent number of stars of the 15th magnitude per square degree); the atmospheric contribution is approximately the same under good observing conditions. It is virtually impossible to detect an increase in brightness toward the center ~1 S_{15} (Fig. 2) against this background. In polarized light, however, the tangential orientation of the electric vector must help distinguish the echo on a large-scale background map. Besides, the expected polarization of the light from the echo must be larger than that from the background. When measuring the large-scale polarization of galaxies (with a ~13-arcmin field), Sholomitskiĭ *et al.* [10] achieved an accuracy in

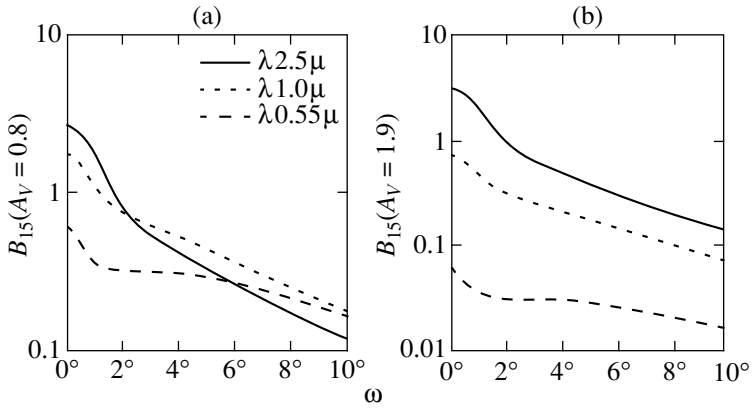

Fig. 2. Expected echo intensity for Tycho Brahe's SN, in units of S_{15} (the number of stars of the 15th magnitude per square degree), versus angular distance to the direction of its observation in 1572: (a) for $A_V = 0.8^m$ and (b) for $A_V = 1.9^m$.

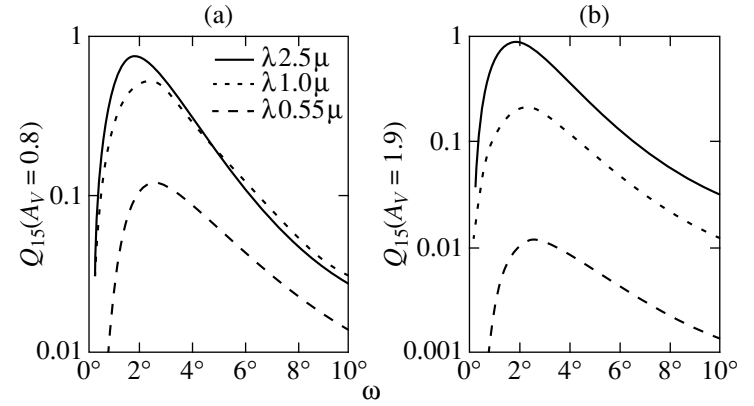

Fig. 3. Expected tangentially polarized echo intensity for Tycho Brahe's SN, in units of S_{15} (the number of stars of the 15th magnitude per square degree), versus angular distance to the direction of its observation in 1572: (a) for $A_V = 0.8^m$ and (b) for $A_V = 1.9^m$.

measuring the tangential linear polarization of approximately 10^{-4} of the (atmospheric) background level in 1 or 2 h of observations. Longer observations during one or more years to average (study) the zodiacal light must increase this accuracy. A prior knowledge of the angular distribution of the (fairly typical, Fig. 3) sought-for signal enables spatial filtration to be carried out and will allow the detection threshold to lower further still (several-fold) (of course, simultaneously with substantial losses in the possibility of comparing various models of the interstellar medium). One might expect an echo with a tangentially polarized intensity ~0.1 S_{15} to be detectable during long-term observations from space and, under favorable conditions, also from the ground; i.e., the echo of Tycho Brahe's SN (Fig. 3) can be detected.

CONCLUSION

Detecting light echoes of Galactic SNe requires no large instruments. It will suffice to have a 20–40-mm objective with a large aperture ratio, a CCD array, and a polaroid. A sufficiently high angular resolution is required for a field of view of several degrees, which allows stars and other objects clearly unrelated to the echo to be excluded.

Among the space experiments, we may note a geostationary, radiatively cooled telescope (GRCT) [11] with a 15-cm objective, a 2°–5° field of view, and an angular resolution of 20″–2′, which is currently under development. This telescope will survey polar sky regions in the visible and in the infrared and, among other tasks, will enable a regular construction of the polarization map.

Detecting light echoes of Galactic SNe and studying their intensity distribution and temporal variability can provide valuable information about the properties of the interstellar medium in the solar neighborhood.

ACKNOWLEDGMENTS

This study was supported by the Ministry of Science and Technology (IKON project of the Federal program "Astronomy and Space Research") and the Russian Foun-

dation for Basic Research (project nos. 99-02-18431 and 00-02-16396).

REFERENCES

1. I. S. Shklovskiĭ, *Supernovae and Related Problems* (Nauka, Moscow, 1976).
2. G. B. Sholomitskiĭ, Astron. Zh. **68**, 30 (1991) [Sov. Astron. **35**, 15 (1991)].
3. T. A. Lozinskaya, *Supernovae and Stellar Wind. Interaction with Galactic Gas* (Nauka, Moscow, 1986).
4. R. L. White, Astrophys. J. **229**, 954 (1979).
5. J. S. Mathis, W. M. Rumpl, and K. H. Nordsieck, Astrophys. J. **217**, 425 (1977).
6. C. W. Allen, *Astrophysical Quantities* (Athlone Press, London, 1973; Mir, Moscow, 1977).
7. É. S. Brodskaya, Izv. Krym. Astrofiz. Obs. **26**, 375 (1961).
8. A. S. Sharov, Astron. Zh. **40**, 900 (1963) [Sov. Astron. **7**, 689 (1963)].
9. D. H. Clark and F. R. Stephenson, Supernovae (New York, Pergamon Press, 1977).
10. G. B. Sholomitskiĭ, I. A. Maslov, and É. A. Vitrichenko, Pis'ma Astron. Zh. **25**, 803 (1999) [Astron. Lett. **25**, 697 (1999)].
11. G. B. Sholomitskiĭ and I. A. Maslov, Adv. Space Res. **25**, 2281 (2000).

Translated by V. Astakhov

Astronomy Letters, Vol. 26, No. 7, 2000, pp. 433–438. Translated from Pis'ma v Astronomicheskiĭ Zhurnal, Vol. 26, No. 7, 2000, pp. 504–509.

Novae in M 31 in 1998

A. S. Sharov[1†], A. Alksnis[2], A. V. Zharova[1*], and Yu. A. Shokin[1]

[1] *Sternberg Astronomical Institute, Universitetskiĭ pr. 13, Moscow, 119899 Russia*
[2] *Institute of Astronomy, Latvian University, Riga, Latvia*

Received December 14, 1999

Abstract—We present data on the six novae in the galaxy M 31 that were discovered by different groups of observers in 1998. Three of these novae were found near the nucleus of M 31, and one was found near the nucleus of M 32. © *2000 MAIK "Nauka/Interperiodica".*

Key words: *novae*

From July 1998 through March 1999, we continued our program of photographing the galaxy M 31 with the aim of searching for and studying novae. We used the 50-cm Maksutov telescope at the Crimean Station of the Sternberg Astronomical Institute and the Schmidt telescope (80/120/240 cm) at the Baldone Astrophysical Observatory of the Institute of Astronomy (Latvian University).

In our observations, we used hydrogen-hypersensitized NT-1 AS photographic plates produced by the limited-liability company "Dar" (Pereslavl'-Zalesskiĭ) and filters that reproduced the *B* photometric system. The plates were examined either in the mode of blink or stereo comparator, while the region near the nucleus of M 31 was also examined with the aid of a simple magnifying glass.

During the observing season of 1998/1999, a search for novae in M 31 was undertaken by a group of researchers as part of the Lick Observatory search for supernovae with a 0.8-m automatic telescope. They discovered three novae near the nucleus of M 31 [1–3] and one nova near the nucleus of M 32 (NGC 221), a companion of M 31 [4]. Two of these four novae were independently discovered by us on our plates, and one nova, N(Esip), was discovered by Esipov [5] with a CCD detector in Crimea. Yet another nova, N(Abas), was discovered at Abastumani Astrophysical Observatory [6] and one nova was found on our plates. We designated the three novae we discovered as ShA 62–ShA 64, in accordance with our previously adopted notation [7]. We studied a total of six novae, including the nova that flared up close to the center of M 32.

The nova coordinates RA and Dec for epochs 1950 and 2000 measured on our plates are given in columns 3–6 of Table 1. We used reference stars from the catalog [8] to determine accurate positions of the novae. The seventh and eighth columns give, respectively, the number of measured plates and the accuracy of determining the positions (in both coordinates). The first and second columns contain, respectively, our designation of the nova and the number of the IAU Circular in which the discovery of this nova with the automatic telescope as part of the Lick Observatory program was reported.

Finding charts for the novae are shown in Fig. 1. North is at the top, west is on the right, and the side of each chart is 6′.

Our brightness estimates of the novae were based on standards in the central region of M 31 [9] and on Arp's photoelectric standards [10]. The results are presented in Tables 2A, 2B, and 2C, which give mid-exposure Julian dates and *B* magnitudes. The *B* light curves are displayed in Fig. 2, where the rectangles and crosses represent, respectively, reliable and unreliable brightness estimates, and the pluses denote upper limits on the brightness if the star was unseen.

Basic data on the six novae are presented in Table 3. Columns 2 and 3 contain rectangular *X* and *Y* coordinates (in arcminutes) in Arp's system [10]: the positive direction of the *X* axis is along the major axis of M 31 to NE, and the positive direction of the *Y* axis is along the minor axis to SE. Column 4 gives distances *R* (in kpc) from the galaxy nucleus under the assumption that the novae are located in the plane of M 31 whose axial ratio is 4 : 1. Columns 5 and 6 list Julian dates and magnitudes $B(\max)$ at the observed maximum light. Column 7 gives the parameter $\log(100d)$, where d is the rate of decline in brightness (in magnitudes) within the first two magnitudes after maximum. Column 8 contains nova types according to Payne-Gaposchkin's [11] classification.

Three of the novae (ShA 62, N(Esip), and ShA 63) are at a distance of less than 1.6 arcmin from the M 31 center, where the high density and the large background

† Deceased.
* E-mail address for contacts: alla@sai.msu.ru

Table 1

Nova	IAU Circ.	RA (1950)	Dec (1950)	RA (2000)	Dec (2000)	*N*	Position accuracy
ShA 62	6981	$0^h39^m52^s.75$	+41°00′29″.6	$0^h42^m36^s.96$	+41°16′55″.3	2	0″.5
N(M 32)	7004	0 39 55.25	+40 34 43.9	0 42 39.32	+40 51 09.5	3	0.2
N(Abas)	–	0 39 49.73	+40 48 31.6	0 42 33.86	+41 04 57.3	4	0.2
N(Esip)	7015	0 40 02.40	+40 58 22.2	0 42 46.64	+41 14 47.8	1	0.3
ShA 63	7023	0 40 05.62	+41 00 22.4	0 42 49.53	+41 16 47.9	2	0.5
ShA 64	–	0 39 19.92	+40 55 26.6	0 42 03.97	+41 11 52.7	2	0.3

Table 2A

JD 2451000+	*B* (ShA 62)
02.503	18.4
22.415	16.2
22.436	16.0
26.422	17.1:
26.443	16.9
27.431	17.9:
41.373	18.4:
42.400	(18.4

Table 2B

JD 2451000+	*B* N(M 32)	*B* N(Abas)	*B* N(Esip)	JD 2451000+	*B* N(M 32)	*B* N(Abas)	*B* N(Esip)	*B* ShA 63
48.365	(19.2	(19.8		75.391	18.6:		17.1	
48.403	(19.5	(19.5		76.270			17.7	
49.362	(19.0	(18.6		76.308	19.0::			
52.340		18.3:		76.311	18.7	(19.1	17.3	
52.395		18.3:		77.296	18.7	(19.4	18.5	
53.375		16.4		77.322	19.2:		17.6	
53.572	18.8:	16.0		78.281			18.1	
54.404		16.1:		78.304	19.1:			
54.526		16.1		80.478			17.8:	(18.4
55.396		17.2:		80.508	18.1::		18.2:	(18.4
55.492	18.6	17.3		82.317	19.2			
56.427	17.6	17.2		83.281	19.0:		17.0	16.7
56.549	16.2	17.0		83.349	19.0:			
57.438	16.2	17.4		84.316	19.0:		17.0	16.8
60.532	17.2	17.8		84.353	19.2			
67.289		18.3:		85.365	19.2			
68.265	17.6			85.404			17.6	17.4
69.269	17.6			86.482			17.6	16.5
69.310	18.0			87.462			17.8:	17.3
70.333	18.7	18.5	16.5:	87.486			18.2	18.4:
70.361	18.2	19.1:	16.5	87.507	19.2:		18.4:	18.0::
72.288	18.4			88.469				18.1
73.316			16.5:	88.502	18.8			
74.302	18.4			96.229	19.2			
74.337		(18.3	16.7	97.251				(18.1
74.368			16.7:	100.278	18.8::			
75.313	18.6			113.293	(20.0	(20.0	(18.4	(18.4
75.342	18.8	19.2	17.3					

Table 2C

JD 2451000+	*B* ShA 64	JD 2451000+	*B* ShA 64
106.393	(19.5	139.328.	18.2
109.206	19.0:	139.352	(18.5
109.244	18.9	140.314	18.0
110.229	19.0	141.119	(18.0
111.226	19.0:	141.223	(18.5
112.266	(19.1	141.290	18.3
113.293	(19.8	141.320	18.5
115.417	(19.1	143.321	18.8
117.563	19.0:	143.348	18.7
127.215	(18.8	158.204	18.4
128.274	(18.5	158.236	18.4
128.306	(18.5	158.257	(18.5
129.214	(19.5	161.228	18.7
135.193	18.7:	161.286	(18.5
135.219	18.6	161.330	18.5:
136.223	(18.0:	170.206	18.8
137.215	17.2	170.241	18.7
137.290	18.0	189.200	(19.0
138.198	18.5:	189.237	(19.0

Table 3

Nova	*X*'	*Y*'	*R*, kpc	JD(max) 2451000+	*B*(max)	log(100*d*)	Type
ShA 62	–0.1	–1.6	1.2	21–23	$\leq 16\overset{m}{.}1$	1.5:	Very fast
N(Abas)	–9.9	+5.2	4.4	53–54	16.0	1.30	Very fast
N(Esip)	–0.3	+1.1	0.8	71–73	16.1–16.3	1.5:	Very fast
ShA 63	+0.9	+0.3	0.3	85–87	16.7:	1.5:	Very fast
ShA 64	–7.9	–3.5	3.0	137–140	17.5–17.9	<0.6	Slow (?)
N(M 32)	–20.5	+14.5	12.6	56–57	16.1	1.20	Fast

gradient limit the magnitude for the detection of stars, make it difficult to estimate their brightness, and lower the accuracy of the results. The same remarks can be made for the nova N(M 32), which is located at a mere 53″ from the nucleus of M 32 (NGC 221), considerably closer than the nova S 10730 [12], and may belong to this companion of the galaxy M 31. However, in Table 3, we give its coordinates and distance relative to the M 31 center.

Since we were able to estimate the brightness of the novae ShA 62 and ShA 63, which are close to the M 31 center, only in a short time interval after maximum, the parameters of the light curves for these novae in Table 3 are less reliable. Nevertheless, both stars undoubtedly belong to very fast novae. (The first estimate for ShA 62 in Table 2, $B = 18.4$, may refer to a plate defect, and we disregard it.) The initial brightness decline of the nova N(Esip) also corresponds to very fast novae; however, a secondary maximum was found 11–13 days after the primary maximum, which is not characteristic of fast and very fast novae. N(Abas) also belongs to very fast novae, and N(M 32) is a fast nova. The nova ShA 64 coincides in position, to within several arcseconds, with the known variable star V725 in M 31. The star was discovered by Baade and Swope [13]. The doubt as to whether the nova ShA 64 is this variable star remains. The light curve of ShA 64 is unusual: approximately 30 days before the maximum, a secondary maximum was noted, which may be a kind of a pre-maximum standstill—the well-known phase of the light curves for a number of novae. The rate of brightness decline in ShA 64 cannot be reliably determined

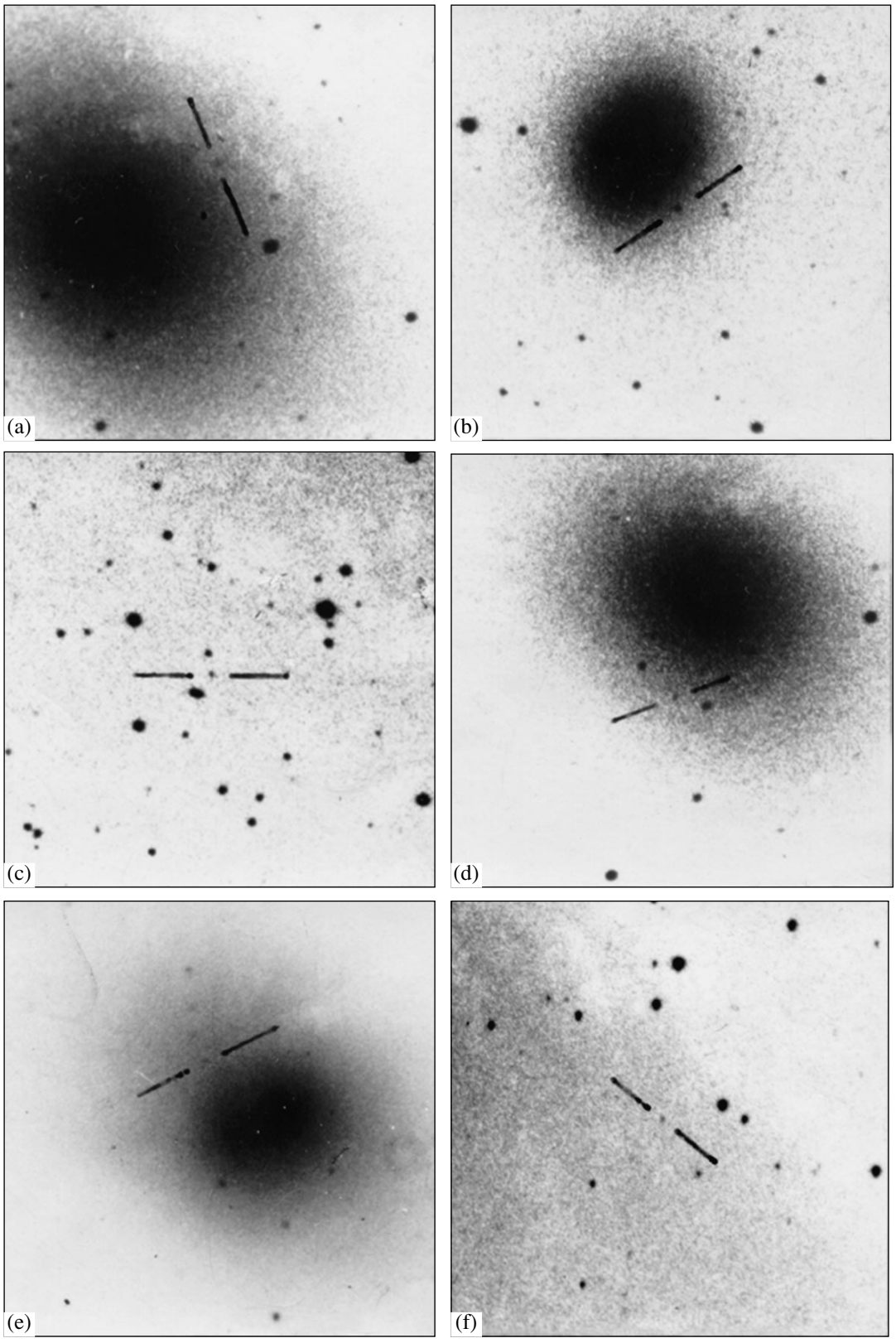

Fig. 1. (a–f) Finding charts for the novae in M 31 discovered in 1998.

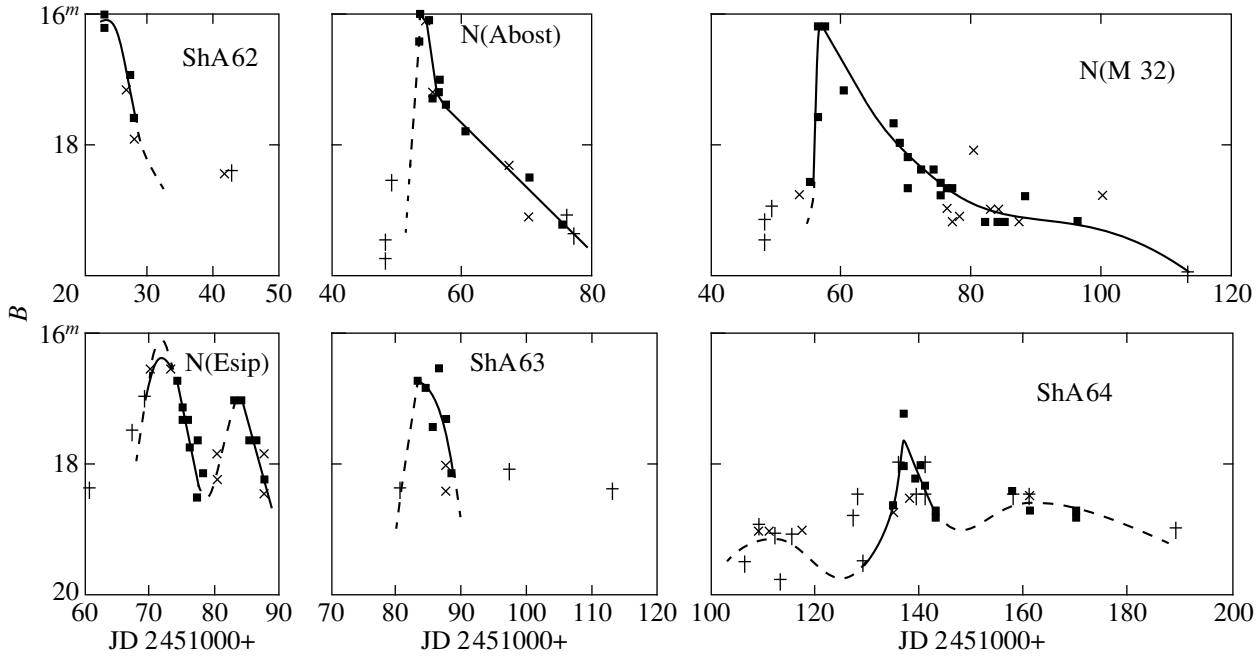

Fig. 2. *B* light curves of the novae.

from our data; if this star is a nova, it probably belongs to slow or moderately fast ones.

The high percentage (50%) of novae near the nucleus of M 31 in this observing season can be explained in part by the fact that M 31 was included in the observing program of the Lick Observatory automatic telescope in 1998. However, two of the three such novae were also discovered on our plates. The nova ShA 62 was found on July 31 when examining the center of M 31 with a magnifying glass on the plates taken on July 27/28 with the Schmidt telescope. The discovery of this object was facilitated by the fact that the exposure used for the photographs was not full, only 20 min instead of usual 40 min, because of the insufficiently dark sky background in this season. In order to detect and study novae flaring up near the center of M 31, we therefore have decided in our subsequent work to take also short-exposure (15–20 min) photographs, in addition to full-exposure photographs (40–60 min), whenever possible.

Four of the six novae can apparently be attributed to the bulge of M 31. If N(M 32) belongs to the companion of M 31, then only N(Abast) turns out to be a disk nova, in contrast to 4–6 such objects found in each of the previous seasons. Several disk novae were probably missed in the 1998/99 season, because many photographs of the July moonless period were veiled, while in October the Schmidt telescope was not operating.

Photometric observations close in time to our photographs were obtained for four 1998 novae in M 31 [1–4] as part of the Lick Observatory program of search for supernova. Although the Lick data are unfiltered CCD magnitudes [*m*(CCD)], their comparison with our brightness estimates can give an idea of the color indices for the novae in M 31.

Table 4 gives data for six such cases: the nova name is followed by the Julian date of observations, the *B* magnitude of the nova on a given night, the *B*–*m*(CCD) color index, and the time interval (in days) between the Lick and our observations. The *B*–*m*(CCD) color indices are virtually the same ($+1\overset{m}{.}6$) for two novae, ShA 62 and ShA 63, and differ significantly (from $-0\overset{m}{.}3$ to $-1\overset{m}{.}3$) for two other novae, N(M 32) and N(Esip). No correlation is seen between the color index and the nova brightness or the time after maximum light. These differences apparently cannot be explained by possible systematic errors in our *B* estimates due to the strong background and its steep gradient near the nucleus of M 31 on our photographs either. The color indices may change significantly at some phases of the nova light curves. However, the available data on color character-

Table 4

Novae	JD 2451000+	*B*	*B*–*m*(CCD)	Δt
ShA 62	22	16.1	$+1\overset{m}{.}7$	$0\overset{d}{.}4$
"	26	17.0	+1.4	0.4
N(M 32)	56	16.2	–0.4	0.4
"	57	16.2	–0.3	0.4
N(Esip)	73	16.5:	–1.3	0.5
"	87	18.1	–0.4	0.3
ShA 63	87	17.8:	+1.6	0.3

istics for M 31 novae are not enough for definitive conclusions to be reached.

ACKNOWLEDGMENTS

We are grateful to V.P. Goranskiĭ, N.A. Gorynya, D.Yu. Tsvetkov, and N.N. Pavlyuk, who took part in the Crimean observations and to T.A. Birulya, who prepared the photographic plates.

REFERENCES

1. M. Modjaz, E. Halderson, T. Shefler, *et al.*, IAU Circ., No. 6981 (1998).
2. M. Papenkova, J. Y. King, E. Halderson, *et al.*, IAU Circ., No. 7023 (1998).
3. E. Halderson, T. Shefler, M. Modjaz, *et al.*, IAU Circ., No. 7015 (1998)
4. E. Halderson, T. Shefler, M. Modjaz, *et al.*, IAU Circ., No. 7004 (1998).
5. V. F. Esipov, private communication (1998).
6. N. N. Samus', R. Inasaridze, G. Kimeridze, *et al.*, IAU Circ., No. 7028 (1998).
7. A. S. Sharov and A. Alksnis, Pis'ma Astron. Zh. **24**, 743 (1998).
8. Yu. A. Shokin and N. B. Kulagina, Pis'ma Astron. Zh. **24**, 93 (1998).
9. L. Rosino, M. Capaccioli, M. D'Onofrio, and M. Della Valle, Astron. J. **97**, 83 (1989).
10. H. C. Arp, Astron. J. **61**, 15 (1956).
11. C. Payne-Gaposchkin, *The Galactic Novae* (Amsterdam, North Holland, 1957), p. 24.
12. L. Meinunger, Mitt. über Veränd. Sterne (Sonneberg) **5**, 177 (1971).
13. W. Baade and H. H. Swope, Astron. J. **70**, 212 (1965).

Translated by N. Samus'

Astronomy Letters, Vol. 26, No. 7, 2000, pp. 439–451. Translated from Pis'ma v Astronomicheskiĭ Zhurnal, Vol. 26, No. 7, 2000, pp. 510–524.

Optical Spectrum of the Bipolar Nebula AFGL 2688

V. G. Klochkova[1]*, R. Szczerba[2], and V. E. Panchuk[1]

[1] *Special Astrophysical Observatory, Russian Academy of Sciences, Nizhniĭ Arkhyz, Karachaevo-Cherkessiya, 369167 Russia*
[2] *N. Copernicus Astronomical Center, Torun, Poland*

Received May 11, 1999; in final form, January 14, 2000

Abstract—Based on echelle spectra obtained at the prime focus of the 6-m telescope, we have determined for the first time the detailed chemical composition of one of the components of the bipolar nebula identified with the intense infrared source AFGL 2688 by the model-atmosphere method. The iron abundance [Fe/H] = –0.59 dex derived for AFGL 2688 suggests that the object probably belongs to an intermediate population of the Galaxy. The stellar atmosphere exhibits high carbon and nitrogen abundances, [C/Fe] = +0.73 and [N/Fe] = +2.00, and C/O > 1, confirming that the object is at the post-AGB stage. However, the detected overabundance of *s*-process elements (yttrium and barium) relative to iron is modest: [X/Fe] = +0.55. The lanthanides are even less enhanced: for La, Ce, Pr, and Nd, the mean abundance relative to iron is [la/Fe] = +0.26. This behavior of the heavy metals is consistent with the low intensity of the 21-μm band in the infrared spectrum of AFGL 2688; the intensity of this emission band is great in the spectra of all the studied PPN with large overabundances of s-process elements. An analysis of the radial velocities measured from spectral features originating in the atmosphere and in the circumstellar shell has revealed a high-velocity (~60 km s^{-1}) component of the stellar wind from AFGL 2688. © *2000 MAIK "Nauka/Interperiodica".*

Key words: *bipolar nebula, abundance analysis*

1. INTRODUCTION

Here, we present the results of our study of the optical spectra for AFGL 2688, an object that is rapidly evolving away from the asymptotic giant branch (AGB). This study is a continuation of our program of analyzing the optical spectra of Galactic infrared sources identified with stars at a short post-AGB evolutionary stage, during which intermediate-mass stars pass into the planetary-nebula phase. Previous results of our analysis of the optical spectra for protoplanetary-nebula (PPN) candidates were published in [1–11]. In his review article, Kwok [12] defined the class of PPN-candidate objects (high-luminosity stars with evidence of mass loss, with a double-peaked energy distribution, and with a detached expanding gas–dust shell) and listed the main observed features. Being at the post-AGB stage, these objects are of considerable interest in studying the chemical evolution of stars and the Galaxy as a whole, because it is the stars of this type that mainly enrich the interstellar medium with carbon, nitrogen, and s-process elements [13]. Stars at such an advanced evolutionary stage can exhibit chemical peculiarities determined by their own history—a successive change of energy-releasing nuclear reactions accompanied by a change in the structure and chemical composition of the stellar envelope, by the mixing of matter, and by the dredge-up of nuclear-reaction products to the surface layers.

The first stages of the investigation of AFGL 2688 (the Egg nebula) were chronicled by Ney [14]. An optical image of the object shows two small faint elliptical nebulae located almost along the north–south axis and separated by approximately 8 arcsec. Both nebulae scatter optical light from the central object, which is obscured from the observer by a dusty torus. The conclusion about the scattering of light from the central star is confirmed by the high degree of polarization in the visible and in the near infrared (~50%). The degree of polarization begins to decrease near a wavelength of 2 μm [15], suggesting an increasing contribution of the intrinsic emission from the dust shell. The conclusion about the presence of a torus follows from the position, orientation, and temperature (150 K) of the compact (1.5 arcsec) infrared source [15].

Forrest *et al.* [16] pointed out that the energy distribution in the range 2–24 μm could not be described by a single temperature of the dust shell, and that the absence of infrared spectral features at 9.7 and 3.1 μm suggested the absence of silicate dust and ice, respectively. The nebula had brightened in 50 years since 1920 by 2^m [17], but no appreciable light variations have been observed in recent years. Schmidt *et al.* [18] constructed a linear-polarization map for the object and showed the following: both dust nebulae are optically thin to scattering, the scattering-particle size is ~0.1 μm,

* E-mail address for contacts: valenta@sao.ru

the scattering enhances the blue part of the spectrum, and the total extinction of an F5 Ia supergiant exceeds 5^m.

Being extremely bright in the infrared, AFGL 2688 was one of the first objects on which new tools for infrared and submillimeter observations were tested. By now, the source has been extensively investigated in the above wavelength ranges. However, because of the low visible flux, the object has been studied at optical wavelengths only photometrically and with a medium spectral resolution; because of its high degree of polarization, it has also been investigated polarimetrically and spectropolarimetrically.

Neither metallicity nor a detailed atmospheric abundance curve for the central star can be inferred from medium-resolution optical spectra of the object. In addition, it is incomprehensible how the known radial-velocity determinations for individual features are related to the velocity of the central star. Consequently, the type of Galactic population to which this object belongs is still difficult to determine.

2. OBSERVATIONS AND DATA REDUCTION

We carried out all observations with the 6-m BTA telescope using the PFES echelle spectrometer [19] equipped with a 1040 × 1170 CCD array, which provided the spectral resolution R = 15 000. On different dates (see Table 1), three spectra with a signal-to-noise ratio ~100 were taken for AFGL 2688 in the wavelength range 4600–8000 or 4700–8600 Å. The spectrometer slit (3.5 arcsec in height and 0.6 arcsec in width) was oriented at the center of the optical image for the nebula's northern lobe parallel to the dust-disk plane.

We performed standard 2D-image processing procedures (addition, filtration to remove cosmic-ray hits, etc.) and extracted echelle orders from CCD images by using the ECHELLE context of the MIDAS-ESO system (version NOV95) in the Linux operating environment. To identify telluric lines in the spectra, we took a similar spectrum of a hot, rapidly rotating star on each observing night. The spectrum quality for the object under study was high enough to measure equivalent widths W with an accuracy of 10–15 mÅ. The line equivalent widths used to compute the chemical composition of AFGL 2688 are given in Table 2. It should be borne in mind that most of the lines used to compute the chemical composition have equivalent widths up to 100–150 mÅ. This places stringent requirements on the accuracy of observational data, because the accuracy of W for weak lines at a given spectral resolution depends mainly on the signal-to-noise ratio in the spectrum.

Based on reference lines in the comparison spectrum (thorium + argon), we constructed a calibration relation in the form of a bivariate third-degree polynomial for the entire echelle image. The position zero point of each spectrogram was determined by referencing to the positions of ionospheric night-sky emission features and telluric absorption spectral lines, which were observed against the background of the object's spectrum. The error in the radial velocity measured from a single spectral line is σ = 3.2 km s^{-1}.

3. DETERMINING THE MODEL-ATMOSPHERE PARAMETERS AND COMPUTING THE CHEMICAL COMPOSITION

The colors of the nebula's central star are distorted by circumstellar and interstellar extinction (reddening), by scattering by dust grains in circumstellar structures (an enhancement of the blue part of the spectrum), by molecular absorption in the shell (predominantly in C_3 bands; reddening), and by the contribution of molecular C_2 emission bands. The hydrogen-line profiles are distorted by emission components (see Fig. 1). We therefore had to restrict ourselves to metal lines in order to determine the model-atmosphere parameters. We derived the effective temperature $T_{\rm eff}$ from the condition that the Fe I abundance was independent of the excitation potential of the corresponding lines, chose the surface gravity log$g$ from the condition of ionization balance for iron atoms, and chose the microturbulence from the condition that the iron abundance was independent of line intensity.

When the model-atmosphere parameters are determined, it is important to restrict the analysis to low- and moderate-intensity lines. In the approximation of a stationary, plane-parallel atmosphere, strong lines in the spectrum of a supergiant are generally described worse. In addition, some of the strong absorption features may originate in the circumstellar shell, and the intensity of the shell components can be included in the intensity of the atmospheric components at an insufficient spectral

Table 1. A log of observations and the heliocentric radial velocities of AFGL 2688 measured from various features in its optical spectra. The number of spectral features measured to determine the mean velocity is given in parentheses

Spectrum	JD 2450000+	λ	$V_\odot$, km s^{-1}						
			metal lines	Hα		C_2 Swan	Na I D1, D2		
				abs.	emis.				
s17751	0677.42	4690–8600	–14.6 ± 0.5(54)	–17.5	–82.8	–84.1 ± 4.8(6)		–16.5	–83.9
s18208	0764.20	4690–8600	–27.6 ± 0.6(26)	–16.9	–123.4	–80.7 ± 5.7(4)	–1.5	–22.2	–85.9
s22301	1185.20	4550–8160	–20.1 ± 0.3(99)	–17.8	–74.0	–74.3 ± 4.4(8)	–0.8	–19.8	–75.2

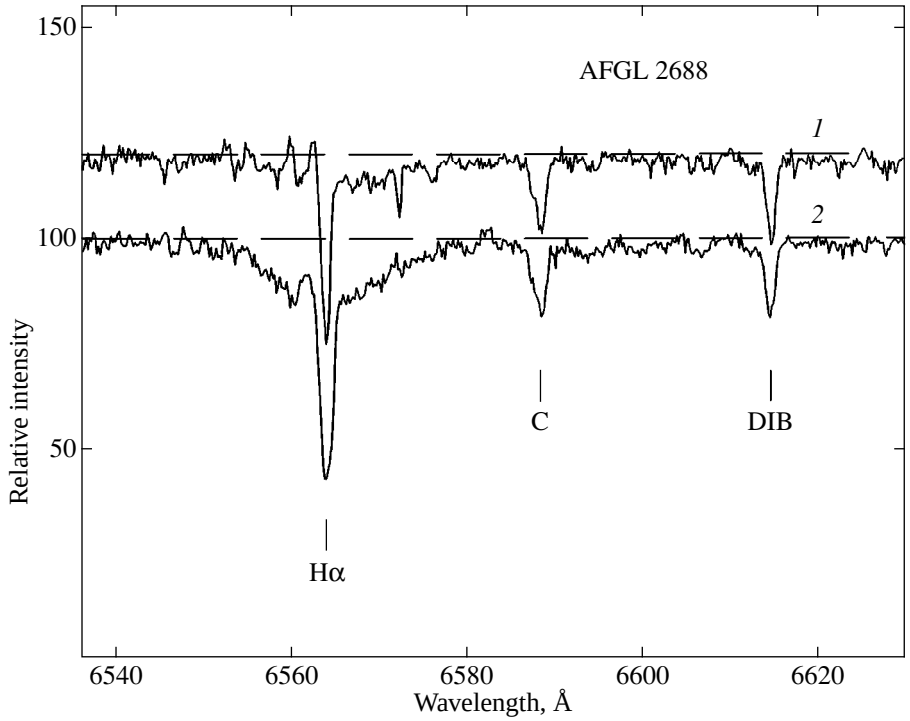

Fig. 1. The spectrum of AFGL 2688 near Hα for two epochs of observations: (*1*) JD = 2450677.4 and (*2*) JD = 2450764.2.

resolution. At the same time, the amount of matter concentrated in the cold envelope of a post–AGB star is not enough to produce weak lines, which emerge mostly during transitions to highly excited levels [5]. Consequently, using the above criteria for the entire set of lines can lead to significant errors in atmospheric parameters [6]. In this study, when determining the model-atmosphere parameters and when computing the elemental abundances, we restricted ourselves to lines with $W < 0.25$ Å.

We used a grid of models computed by means of the MARCS code [20] to determine the fundamental parameters of stellar model atmospheres (effective temperature $T_{\rm eff}$ and surface gravity log$g$) and to compute the chemical composition. Oscillator strengths gf of the spectral lines involved in determining the model parameters and the elemental abundances are given in Table 2. We took the oscillator strengths loggf from Luck's extensive list [21] for most of the lines and from [22, 23] for lines of the CNO group and sulfur. Table 2 provides data for several strong ($W \geq 0.25$ Å) lines, which we disregarded when computing the mean abundance of a given element.

As was noted above, we derived the effective temperature from the condition that the iron abundance was independent of the lower-level excitation potential for the Fe I lines used. An additional criterion for reliability of the method is the lack of the same dependence for other chemical elements, which are also represented in the spectra by numerous lines (for example, C I, S I, Ca I, Sc II). Besides, for a reliably determined microturbulence, there is no dependence of individual abundances on the equivalent widths of the lines used in our calculations. The chromium abundances deduced from lines of neutral atoms and from ion lines are in agreement, within the accuracy of the method. This provides evidence that the atmospheric surface gravity estimated from the condition of ionization balance for iron atoms is correct. In general, the internal agreement between the parameters suggests that the homogeneous model atmospheres used are suitable for computing weak lines in the LTE approximation. We obtained the following model-atmosphere parameters for the star illuminating the nebula AFGL 2688: $T_{\rm eff} = 6500$ K, log$g = 0.0$, $\xi_t = 6.0$ km s^{-1}, and [Fe/H] = –0.59. Our experience of quantitatively interpreting echelle spectra in the above model approximation suggests that the typical accuracy of determining the model parameters for a star with a temperature of ~6500 K is, on the average, $\Delta T_{\rm eff} \approx 200$, $\Delta \log g \approx 0.3$ dex, and $\Delta\xi_t \approx 0.5$ km s^{-1}.

We emphasize that our deduced "spectroscopic" effective temperature matches the value obtained by an independent method of modeling the source's spectral energy distribution in a wide spectral range, from the optical to the far infrared [24].

As we see from Table 3, which gives the results of our abundance determinations, the scatter of elemental abundances deduced from the set of lines is small, with the error of the mean δ being typically no larger than 0.10 dex for more than 6–8 lines.

Table 2. Atomic data (lower-level excitation potentials EP, oscillator strengths *gf*), equivalent widths *W* of spectral lines in AFGL 2688, and the chemical composition *A*(*X*) [at hydrogen abundance *A*(*H*) = 0] calculated with model parameters $T_{\rm eff}$ = 6500 K, log*g* = 0.0, and ξ_t = 6.0 km s^{-1}

λ	Species	EP, eV	log*gf*	*W*, mÅ	*A*(*X*)	λ	Species	EP, eV	log*gf*	*W*, mÅ	*A*(*X*)
6707.75	L II	0.00	–0.43	25	–8.61	6122.23	Ca I	1.89	–0.32	133	–6.25
4817.37	C I	7.48	–2.51	52	–3.68	6163.75	Ca I	2.52	–1.29	22	–5.77
5039.05	C I	7.48	–2.10	170	–3.27	6169.56	Ca I	2.52	–0.48	37	–6.32
5817.70	C I	7.68	–2.87	12	–3.86	6439.08	Ca I	2.52	0.39	175	–6.15
5912.58	C I	9.00	–2.62	12	–3.02	6449.81	Ca I	2.52	–0.50	16	–6.71
5969.40	C I	7.95	–3.08	18	–3.24	6471.67	Ca I	2.52	–0.69	12	–6.65
6014.84	C I	8.64	–1.71	40	–3.65	6499.65	Ca I	2.52	–0.82	22	–6.25
6108.53	C I	8.85	–2.58	15	–3.08	6717.69	Ca I	2.71	–0.52	32	–6.20
6292.44	C I	9.00	–2.19	29	–3.02	7148.15	Ca I	2.71	0.14	109	–6.16
6587.62	C I	8.54	–1.22	222	–2.85	8254.68	Ca II	7.50	–0.38	92	–6.54
6605.80	C I	8.85	–2.31	25	–3.09	5318.37	Sc II	1.36	–2.04	79	–9.09
6671.82	C I	8.85	–1.65	38	–3.54	5357.19	Sc II	1.51	–2.21	19	–9.51
6711.30	C I	8.54	–2.47	24	–3.21	5552.24	Sc II	1.45	–2.27	68	–8.88
7100.30	C I	8.64	–1.60	101	–3.17	5640.99	Sc II	1.50	–1.01	192	–9.32
7108.94	C I	8.64	–1.68	100	–3.10	5667.15	Sc II	1.50	–1.20	166	–9.28
7111.48	C I	8.64	–1.32	103	–3.44	5669.04	Sc II	1.50	–1.09	220	–9.06
7113.18	C I	8.65	–0.93	192	–3.22	5684.20	Sc II	1.51	–1.01	225	–9.11
7115.19	C I	8.64	–0.90	176	–3.37	5336.78	T III	1.58	–1.70	240	–7.87
7116.99	C I	8.65	–1.08	106	–3.65	5418.80	T III	1.58	–2.17	236	–7.44
7119.67	C I	8.64	–1.31	100	–3.47	5928.89	V II	2.52	–1.59	31	–8.74
7423.64	N I	10.33	–0.61	233	–2.39	6028.27	V II	2.49	–1.98	15	–8.72
7442.29	N I	10.33	–0.31	250	–2.57	5345.77	Cr I	1.00	–0.98	86	–6.74
7468.31	N I	10.34	–0.13	228	–2.91	5409.78	Cr I	1.03	–0.72	69	–7.11
8216.34	N I	10.34	0.16	398[1]	–2.73	5702.30	Cr I	3.45	–0.67	7	–6.18
8242.39	N I	10.34	–0.21	374[1]	–2.49	7355.93	Cr I	2.89	–0.29	35	–6.30
6155.98	O I	10.74	–0.66	55	–3.27	5097.33	Cr II	3.71	–2.64	152	–6.38
6156.77	O I	10.74	–0.44	55	–3.49	5246.76	Cr II	3.71	–2.45	138	–6.67
6158.18	O I	10.74	–0.29	102	–3.19	5249.43	Cr II	3.76	–2.62	126	–6.54
5682.65	Na I	2.10	–0.71	55	–5.89	5308.46	Cr II	4.07	–1.81	176	–6.76
5688.22	Na I	2.10	–0.40	85	–5.95	5310.73	Cr II	4.07	–2.28	72	–6.98
6154.23	Na I	2.10	–1.57	21	–5.51	5334.88	Cr II	4.07	–1.89	212	–6.44
6160.75	Na I	2.10	–1.27	27	–5.69	5502.07	Cr II	4.17	–1.99	178	–6.49
7362.28	Al I	4.02	–0.96	8	–5.64	6053.48	Cr II	4.74	–2.16	35	–6.91
5978.93	S III	10.07	–0.06	68	–4.50	6129.23	Cr II	4.75	–2.44	50	–6.45
5696.63	S I	7.87	–1.21	12	–4.95	5049.82	Fe I	2.28	–1.42	120	–5.20
5700.24	S I	7.87	–0.98	20	–4.94	5090.78	Fe I	4.26	–0.40	62	–4.93
6041.92	S I	7.87	–1.00	22	–4.87	5150.84	Fe I	0.99	–3.07	74	–5.00
6045.99	S I	7.87	–0.79	64	–4.53	5151.91	Fe I	1.01	–3.32	69	–4.77
6052.63	S I	7.87	–0.63	44	–4.90	5194.94	Fe I	1.56	–2.09	94	–5.34
6743.58	S I	7.87	–0.70	29	–5.04	5215.18	Fe I	3.27	–0.80	68	–5.33
6748.79	S I	7.87	–0.44	37	–5.17	5232.94	Fe I	2.94	–0.19	182	–5.46
5588.76	Ca I	2.52	0.36	101	–6.59	5247.05	Fe I	0.09	–4.95	5	–5.21
5594.47	Ca I	2.52	0.10	58	–6.67	5250.64	Fe I	2.20	–2.05	33	–5.39
5598.49	Ca I	2.52	–0.09	54	–6.51	5253.46	Fe I	3.28	–1.67	18	–5.12
5601.29	Ca I	2.52	–0.52	30	–6.38	5302.30	Fe I	3.28	–0.88	106	–4.96
5857.46	Ca I	2.93	0.24	56	–6.47	5339.93	Fe I	3.27	–0.68	92	–5.27
6102.73	Ca I	1.88	–0.79	105	–5.98	5364.87	Fe I	4.45	0.22	80	–5.25

Table 2. (Contd.)

λ	Species	EP, eV	log*gf*	*W*, mÅ	*A*(*X*)	λ	Species	EP, eV	log*gf*	*W*, mÅ	*A*(*X*)
5365.40	Fe I	3.57	–1.28	36	–4.93	6494.98	Fe I	2.40	–1.27	72	–5.61
5367.47	Fe I	4.41	0.35	124	–5.10	6592.91	Fe I	2.73	–1.60	25	–5.54
5369.96	Fe I	4.37	0.35	161	–4.90	6593.88	Fe I	2.43	–2.42	14	–5.25
5371.49	Fe I	0.96	–1.64	216	–5.56	6609.12	Fe I	2.56	–2.69	5	–5.34
5373.71	Fe I	4.47	–0.86	10	–5.18	5100.66	Fe II	2.81	–4.37	173	–4.60
5389.48	Fe I	4.41	–0.41	38	–5.05	5325.56	Fe II	3.22	–2.60	233	–5.62
5393.17	Fe I	3.24	–0.91	75	–5.19	5414.05	Fe II	3.22	–3.79	202	–4.64
5397.13	Fe I	0.91	–1.99	212	–5.28	5991.37	Fe II	3.15	–3.74	117	–5.30
5398.29	Fe I	4.45	–0.67	30	–4.88	6084.10	Fe II	3.20	–3.98	165	–4.72
5400.50	Fe I	4.37	–0.16	59	–5.11	6113.33	Fe II	3.22	–4.31	51	–5.18
5405.77	Fe I	0.99	–1.84	226	–5.27	6149.25	Fe II	3.89	–2.92	247	–4.61
5410.91	Fe I	4.47	0.28	150	–4.81	6238.38	Fe II	3.89	–2.87	96	–5.66
5415.20	Fe I	4.39	0.50	181	–4.90	6369.46	Fe II	2.89	–4.36	99	–5.03
5424.07	Fe I	4.32	0.52	172	–5.03	6383.72	Fe II	5.55	–2.27	97	–4.81
5429.70	Fe I	0.96	–1.88	227	–5.25	6416.92	Fe II	3.89	–2.85	227	–4.83
5445.04	Fe I	4.39	–0.02	76	–5.09	6432.68	Fe II	2.89	–3.74	148	–5.35
5446.92	Fe I	0.99	–1.93	196	–5.38	6446.40	Fe II	6.22	–2.16	26	–5.09
5506.78	Fe I	0.99	–2.80	61	–5.40	7479.69	Fe II	3.89	–3.88	23	–5.42
5554.89	Fe I	4.55	–0.44	50	–4.77	7711.71	Fe II	3.90	–2.74	225	–4.95
5565.71	Fe I	4.61	–0.29	15	–5.45	5105.55	Cu I	1.39	–1.51	72	–7.71
5586.76	Fe I	3.37	–0.21	141	–5.34	5218.21	Cu I	3.82	0.27	48	–7.61
5679.02	Fe I	4.65	–0.92	9	–5.02	4810.54	Zn I	4.08	–0.17	50	–8.09
5686.53	Fe I	4.55	–0.63	22	–4.99	6362.35	Zn I	5.79	0.27	6	–8.09
5753.12	Fe I	4.26	–0.76	16	–5.25	5119.11	Y II	0.99	–1.36	202	–9.45
5775.09	Fe I	4.22	–1.23	15	–4.85	5200.41	Y II	0.99	–0.57	320[1]	–9.40
5852.19	Fe I	4.55	–1.33	8	–4.75	5289.82	Y II	1.03	–1.85	102	–9.53
5859.61	Fe I	4.55	–0.60	13	–5.26	5728.89	Y II	1.84	–1.12	106	–9.53
5862.36	Fe I	4.55	–0.38	25	–5.18	5853.67	Ba II	0.60	–1.00	192	–10.21
5905.67	Fe I	4.65	–0.72	15	–4.99	6141.71	Ba II	0.70	–0.08	380[1]	–9.78
5930.17	Fe I	4.65	–0.23	56	–4.83	6496.90	Ba II	0.60	–0.38	371[1]	–9.70
5934.66	Fe I	3.93	–1.17	25	–4.92	5377.06	La II	2.29	0.40	9	–11.43
5983.68	Fe I	4.55	–0.71	18	–5.01	5808.31	La II	0.00	–2.08	7	–11.16
5984.80	Fe I	4.73	–0.31	32	–4.97	6262.25	La II	0.40	–1.45	15	–11.10
5987.06	Fe I	4.80	–0.59	17	–4.94	6320.41	La II	0.17	–1.42	13	–11.41
5997.78	Fe I	4.61	–1.05	11	–4.84	6390.48	La II	0.32	–1.49	17	–11.09
6003.03	Fe I	3.88	–1.12	26	–5.00	6526.95	La II	0.23	–1.58	9	–11.37
6007.96	Fe I	4.65	–0.76	22	–4.77	5274.24	Ce II	1.04	0.32	77	–10.65
6055.99	Fe I	4.73	–0.46	17	–5.12	5472.30	Ce II	1.24	–0.18	21	–10.63
6078.49	Fe I	4.80	–0.38	34	–4.82	6043.38	Ce II	1.20	–0.17	11	–11.01
6136.61	Fe I	2.45	–1.40	94	–5.27	5219.03	Pr II	0.79	–0.24	12	–11.25
6137.69	Fe I	2.59	–1.40	106	–5.07	5089.83	Nd II	0.20	–1.17	29	–10.42
6151.62	Fe I	2.18	–3.30	10	–4.74	5092.80	Nd II	0.38	–0.63	16	–11.08
6180.22	Fe I	2.73	–2.78	4	–5.19	5234.21	Nd II	0.55	–0.33	87	–10.39
6230.73	Fe I	2.56	–1.28	80	–5.40	5293.17	Nd II	0.82	–0.06	36	–10.88
6232.64	Fe I	3.65	–1.33	27	–4.97	5361.51	Nd II	0.68	–0.46	32	–10.68
6252.55	Fe I	2.40	–1.69	31	–5.63	5416.38	Nd II	0.86	–0.93	10	–10.58
6265.13	Fe I	2.18	–2.55	51	–4.72	5485.71	Nd II	1.26	–0.12	10	–11.03
6301.50	Fe I	3.65	–0.59	39	–5.52	5740.88	Nd II	1.16	–0.55	19	–10.42
6380.75	Fe I	4.19	–1.40	9	–4.95	6031.31	Nd II	1.28	–0.70	11	–10.42
6408.02	Fe I	3.69	–1.00	39	–5.08	6049.51	Eu II	1.28	–0.80	11	–11.35
6411.65	Fe I	3.65	–0.82	56	–5.11	6437.64	Eu II	1.32	–0.28	14	–11.74
6430.85	Fe I	2.18	–2.01	31	–5.51						

[1] The lines were not used to determine the mean elemental abundance.

4. DISCUSSION

Let us consider in more detail some of the features that were identified by analyzing both published medium-resolution optical spectra and our high-resolution spectra.

4.1 Spectral Features in AFGL 2688

The near-infrared (1.1–2.4 μm) spectrum of AFGL 2688 is formed by continuum emission and by molecular C_2 and CN emission transitions, with an addition of molecular hydrogen lines on the periphery, which were used to estimate the excitation temperature T_{ex} = 1600 K [25]. The first low-resolution spectroscopic observations [26, 27] revealed principal features of the optical spectrum for AFGL 2688. Of fundamental importance was the identity of the spectra for both components of the bipolar nebular, F5 Iab [26] and F2 Ia [27], which confirmed the hypothesis of scattering as the mechanism of their radiation. In addition, strong blue absorption features, whose positions coincided with the rarely observed molecular C_3 bands, and emission features identified with the molecular C_2 Swan bands were detected. Cohen and Kuhi [27] pointed out that the molecular C_2 bands were observed in emission, but in polarized light these bands were in absorption. It was thus proven that the C_2 emission bands originate in the gas–dust shell polarizing the light from the central star. Note that the molecular spectrum of the cold shell appears to have been observed in polarized light for the first time (at the atmospheric temperatures typical of an F supergiant, no value of O/C can ensure the observed intensities of the C_2 and C_3 absorption bands), but no significance was attached to this. The phenomenon of an absorption molecular shell around post-AGB stars was rediscovered by Klochkova and Panchuk [5] and Bakker *et al.* [28].

Based on their spectropolarimetric observations of the blend composed of unresolved components of the Na I D lines, Cohen and Kuhi [27] showed that the nebula emits in the Na I D line, identified the atmospheric, shell, and interstellar doublet components, and concluded that the interstellar extinction could reach 4^m, i.e., virtually all of the absorption of the photospheric spectrum is produced by external (relative to the nebula) matter. Using ten spectrograms with 7 Å resolution, Cohen and Kuhi [29] showed that the scattered photospheric absorption spectrum did not change appreciably from point to point within the nebula's visible image, but the relative intensity in the blue part of the spectrum increased with distance from the nebula's center. This can be interpreted as a decrease of the mean grain size with increasing distance. The small differences in the intensities of the molecular C_2, C_3, and SiC_2 absorption bands from point to point were interpreted as the flooding of absorption features with emission components. Correlations were found between the emission features identified by subtracting the spectrogram with the deepest absorption features from each of the nine spectra. Apart from the above bands, the sodium resonance doublet emission has thus been rediscovered. We emphasize that the emission features were identified by assuming that the spectrum with the deepest absorption features contains no contribution from emission components. The intensities of the C_2 emission bands with a common upper level derived in this way were used to estimate the reddening; the mean extinction was $8\overset{m}{.}1$ and $11\overset{m}{.}5$ for the northern and southern lobes of the nebula, respectively. The discrepancy between this estimate and the extinction estimated from the interstellar sodium doublet component (4^m) served as a basis for the assumption [29] that the intensity ratio of the C_2 emission bands was distorted by graphite dust within the nebula (note that this dust cannot produce an additional weakening of the photospheric spectrum, whose absorption in the nebula is $3–5^m$). Thus, interpreting the spectroscopic data gives internally inconsistent extinction estimates (from Na I D and C_2), which disagree with an estimate based on broadband photometry [15].

Using several spectroscopic criteria, Hrivnak [30] estimated the spectral type of AFGL 2688 from spectra with ~3 Å resolution to be Sp = F5 Iae and noted a weakening of the Hα line. We emphasize that the Hα profile in the spectra of post-AGB stars is partly distorted by emission, which generally varies with time. Portions of our spectra for AFGL 2688 with Hα are shown in Fig. 1. Clearly, the contribution of unresolved emission components in medium-resolution spectra will cause the equivalent width of the hydrogen absorption feature to decrease.

4.2 The Intensities of Molecular C_2 Swan Bands

AFGL 2688 belongs to a group of systems where the central part (the star and the inner regions of its circumstellar shell) undergoes strong absorption in a gas–dust torus (or disk), while the light from this central part is scattered by dust grains of the bipolar structure. Clearly, objects with a different orientation of the dust disk, for which the object's central part is not obscured from the observer, can be encountered, and the extinction of the central star decreases (compared to AFGL 2688) several tens of times. Both the torus (or disk) and the scattering lobes in the neighborhood of the bright star then become barely detectable optically, and no bipolar nebula is observed. The spectrum of the central star in a system with such an orientation can no longer contain molecular emission bands, because the emission in these bands is "drowned" against the background of the photospheric emission. Indeed, 6-m telescope spectra revealed emission bands of different (relative to continuum) intensities belonging to the molecular C_2 Swan system in IRAS 04296+3429 [10], IRAS 22223+4327 [2], and IRAS 23304+6147 [31], which belong to the group of carbon-rich PPN with the 21-μm feature.

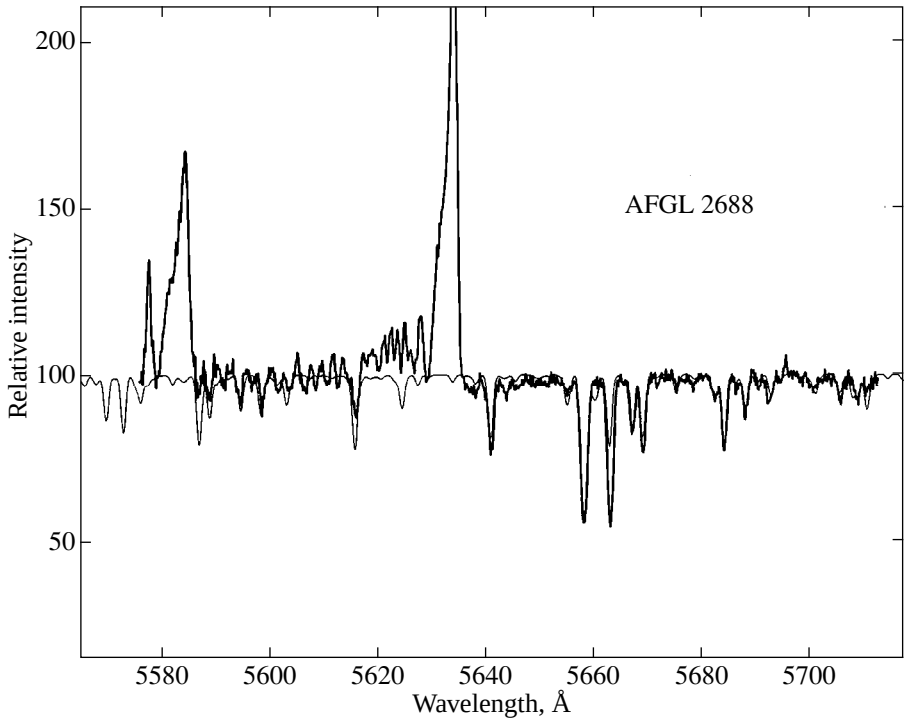

Fig. 2. The molecular C_2 Swan 5585.5 (1;2) and 5635.5 (0;1) emission bands in the spectrum of AFGL 2688 identified by comparison with a theoretical atmospheric spectrum (thin line) for the central star.

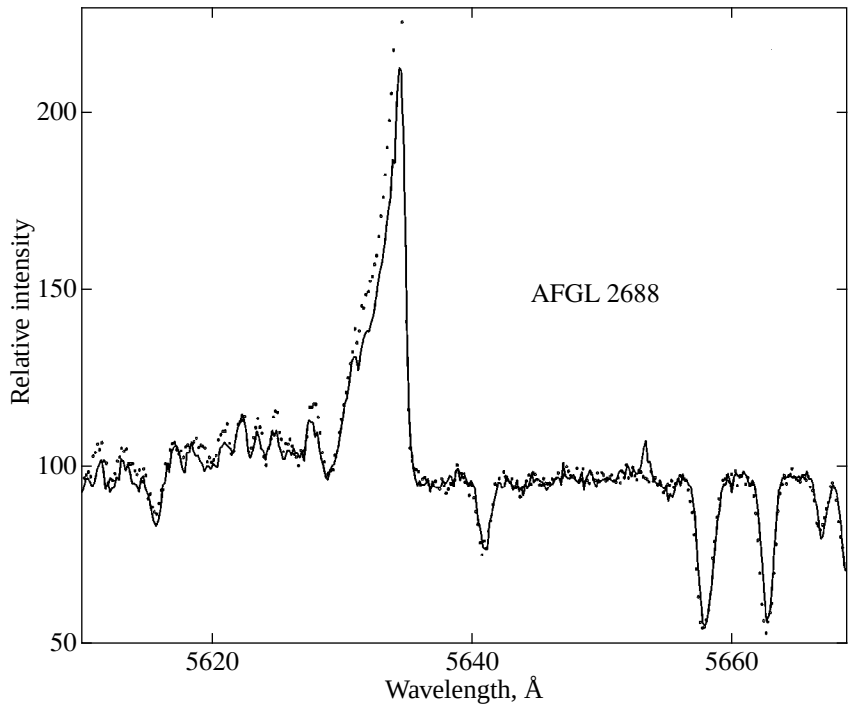

Fig. 3. The molecular C_2 Swan 5635 Å (0;1) emission band in the spectrum of AFGL 2688 for two epochs of observations: JD = 2450677.4 (solid line) and JD = 2450764.2 (dots).

Figure 3 from [11] shows portions of the spectra for these objects with the molecular C_2 Swan (0;1) band. We showed in [10, 31] that the intensity ratio of different molecular C_2 Swan emission bands in the spectrum of IRAS 04296 + 3429 corresponded to the mechanism of resonance fluorescence. In Fig. 2, the observed spectrum near the (0;1) and (1;2) bands is compared with the synthetic spectrum computed from our derived

model parameters and atmospheric chemical composition of AFGL 2688. The dips in the intensity distribution of rotational lines are seen to essentially coincide with photospheric absorption lines. It would be unreasonable to expect a close coincidence of the dip and line positions, because one might expect second-order effects (relative to the mechanism of resonance fluorescence) similar to Greenstein's effect [32] to show up here because of the velocity difference between the atmosphere and the matter emitting in the C_2 bands. It thus follows from Fig. 2 that the intensity distribution of rotational lines also suggests that the mechanism of resonance fluorescence is at work.

Figure 3 shows profiles of the molecular C_2 Swan (0;1) band in the spectrum of AFGL 2688 for two epochs of observations.

In total, up to eight emission bands are observed in the echelle spectrum of AFGL 2688: λ5097.7 Å (2; 2), λ5129.4 Å (1; 1), λ5165.2 Å (0; 0), λ5540.7Å (2; 3), λ5585.5 Å (1; 2), λ5635.5 Å (0; 1), λ6122.2 Å (1; 3), and λ6191.3 Å (0; 2). We emphasize that the bands of the $\Delta\upsilon = -2$ (6122.2 and 6191.3) sequence are clearly observed, whereas in the short-wavelength part of the spectrum there is no emission band of the $\Delta\upsilon = +1$ sequence, for example, the 4737.1 (1;0) band. Let us show that this pattern of behavior of the emission bands is also consistent with the mechanism of resonance fluorescence by using spectrophotometric and spectropolarimetric measurements (Fig. 2 from [27]). In polarized light, the intensity ratio of the (1; 0), (0; 0), and (0; 1) absorption bands resembles the Boltzmann one with a low vibrational temperature typical of a cold shell [the intensity of the (0; 0) band is a factor of 2 or 3 higher than that of the other two bands]. The rapid decline in intensity of the absorption bands of the diagonal sequence (5165.2, 5129.4, and 5097.7) also provides evidence for the low vibrational temperature. A third argument for the low vibrational temperature is that, based on six transitions of the C_2 spectrum and four transitions of the CN spectrum, Bakker *et al.* [28] estimated the shell rotational temperature to be $T_{rot} = 56 \pm 8$ and 18 ± 3 K, respectively. In unpolarized light, the intensity ratio of the emission bands with a common vibrational level is a non-Boltzmann one (the bands with a longer wavelength are brighter). As we already pointed out above, the hypothesis of Cohen and Kuhi [27] that the population of molecular C_2 vibrational levels in the nebular lobe is nevertheless the Boltzmann one and that the band intensity ratio is distorted by strong reddening leads to an unusually large interstellar reddening. If we abandon this hypothesis in favor of the resonance fluorescence mechanism, then the intensity ratio of the emission bands can be qualitatively explained as follows.

The photospheric radiation that passed through the cold molecular shell is weakened near the (1;0), (0;0), and (0;1) band heads, with the weakening being greater near the (0;0) band. Subsequently, the spectrum in the central region of the dust cocoon suffers a strong reddening, which reaches $3–5^m$, as estimated by Ney *et al.* [15]. It is these two effects that produce the highly nonuniform emission exciting the molecular C_2 vibrational levels; i.e., it is no longer needed to explain the intensity ratio of the emission bands by an additional, external (relative to the nebula) reddening. An analysis of the intensity ratio of the diagonal-sequence bands in polarized and unpolarized light provides evidence for this explanation (the hypothesis of a strong reddening is unsuitable for explaining their intensity ratio, because the band heads are close together and the differential reddening is negligible).

There is yet another argument for the hypothesis of a non-Boltzmann molecular C_2 level population in the nebular lobes. Assuming the Boltzmann population of rotational levels, Bakker *et al.* [28] obtained statistically differing rotational temperatures for a circumstellar shell producing the C_2 and CN absorption bands (see above). Since vibrational–rotational transitions in the ground electronic state for homonuclear molecules are forbidden, the Boltzmann approximation for C_2 in a low-density medium yields an estimate of the rotational temperature exceeding the kinetic temperature [33]. The nebular lobe regions where unpolarized C_2 emission bands originate are much farther from the star that the circumstellar shell, in which the C_2 and CN absorption bands are formed at significant departures from local thermodynamic equilibrium. Consequently, there are no grounds for using the Boltzmann approximation in these regions.

4.3 Radial Velocities

Based on their submillimeter CO and HCN observations, Young *et al.* [34] identified three outflow-velocity components: 18, 40, and 100 km s^{-1}; the slow expansion is attributable to the wind characteristic of an AGB star. The mechanical momentum of the low-velocity wind component is a factor of 7 larger than the mechanical momentum provided by radiation pressure [35]. The mechanical momentum of the high-velocity wind component is two orders of magnitude larger than its value that can be explained by radiation pressure by assuming a maximum luminosity for an AGB star [34]. The age of the medium-velocity wind component estimated by assuming a constant outflow velocity is about a thousand years, in agreement with evolutionary tracks for a post-AGB star of mass 0.8–1.0 $M_\odot$ [36]. Based on the distance of the H_2-emitting regions from the nebula center and on the dust outflow velocity (44 km s^{-1} perpendicular to the disk plane) and assuming the distance to the object to be 1 kpc, Jura and Kroto [37] estimated the time when the star left the asymptotic giant branch, about 200 years ago.

The radial velocities measured from individual spectrograms are listed in Table 1. In particular, this table gives the radial velocities corresponding to the absorption component of the Hα profile and the blue-

Table 3. Chemical composition $\log\epsilon(X)$ of AFGL 2688 [for $\log\epsilon(X) = 12.0$]. Here, n is the number of lines used, and δ is the error in the mean abundance derived for a given number of lines. The elemental abundances in the solar photosphere were taken from [41]; for lithium, its meteoritic abundance was used

Sun		AFGL 2688				
X	$\log\epsilon(X)$	X	$\log\epsilon(X)$	n	δ	[X/Fe]
Li	3.31	Li I	2.99	1		+0.27
C	8.55	C I	8.69	19	0.06	+0.73
N	7.97	N I	9.38	3	0.15	+2.00
O	8.87	O I	8.68	3	0.09	+0.40
Na	6.33	Na I	6.24	4	0.10	+0.50
Al	6.47	Al I	6.36	1		+0.48
Si	7.55	Si II	7.50	1		+0.54
S	7.21	S I	7.09	7	0.07	+0.47
Ca	6.36	Ca I	5.66	15	0.07	–0.11
		Ca II	5.46	1		–0.31
Sc	3.17	Sc II	2.82	7	0.08	+0.24
Ti	5.02	Ti II	4.34	2		–0.09
V	4.00	V II	3.27	2		–0.14
Cr	5.67	Cr I	5.42	4	0.21	+0.34
	5.67	Cr II	5.38	9	0.07	+0.30
Fe	7.50	Fe I	6.88	69	0.03	+0.03
		Fe II	6.95	15	0.09	–0.04
Cu	4.21	Cu I	4.34	2		+0.72
Zn	4.60	Zn I	3.91	2		–0.10
Y	2.24	Y II	2.50	3	0.03	+0.85
Ba	2.13	Ba II	1.79	1		+0.25
La	1.22	La II	0.74	6	0.06	+0.11
Ce	1.55	Ce II	1.24	3	0.12	+0.28
Pr	0.71	Pr II	0.75	1		+0.63
Nd	1.50	Nd II	1.34	9	0.09	+0.43
Eu	0.51	Eu II	0.46	2		+0.54

shifted emission feature. The radial velocity measured from the emission component depends both on the emission position in the atmospheric absorption wing and on the position of the absorption line center in the high-lying layers (relative to the center of the emission component), as well as on the intensity ratio of all three components. We therefore do not interpret the changes in the position of the Hα emission component literally as changes in the radial velocity of the emitting layer alone. As follows from the data of Table 1, the position of the Hα absorption component agrees, within the above accuracy, with the positions of metal lines.

The mean velocity, $V_{lsr} = -4.8$ km s^{-1}, derived from numerous (from 26 to 99 lines in each spectrum) unblended metal lines for all epochs of our observations differ from $V_{lsr} = -28.8 \pm 8$ km s^{-1} obtained by Crampton *et al.* [26] from medium-resolution spectra. This value cannot be compared with $V_{lsr} = -34.5 \pm 1$ km s^{-1} determined from the shift of the molecular CO line profile center [38], because the angular aperture of such radio observations completely "covers" the nebula, whereas at optical wavelengths we record the spectrum of one of the nebular regions where the moving dust scatters the light from the central star.

The significant difference between our velocity and that published by Crampton *et al.* [26] suggests radial-velocity variability with time. For the nature of this variability to be elucidated, several homogeneous spectroscopic observations must be carried out.

The positions of asymmetric molecular C_2 emission band heads at a given spectral resolution are determined with a lower accuracy, but, as follows from the data of Table 1, we can assert with confidence that the regions producing the molecular emission move outward faster (by approximately 60 km s^{-1}) than do the formation regions of photospheric absorption features.

Humphreys *et al.* [39] identified an emission component of the sodium resonance doublet profile with a heliocentric velocity of –50 km s^{-1} in an underexposed echelle spectrogram of AFGL 2688. Figure 4 shows a portion of spectrum s22301 in which the atmospheric,

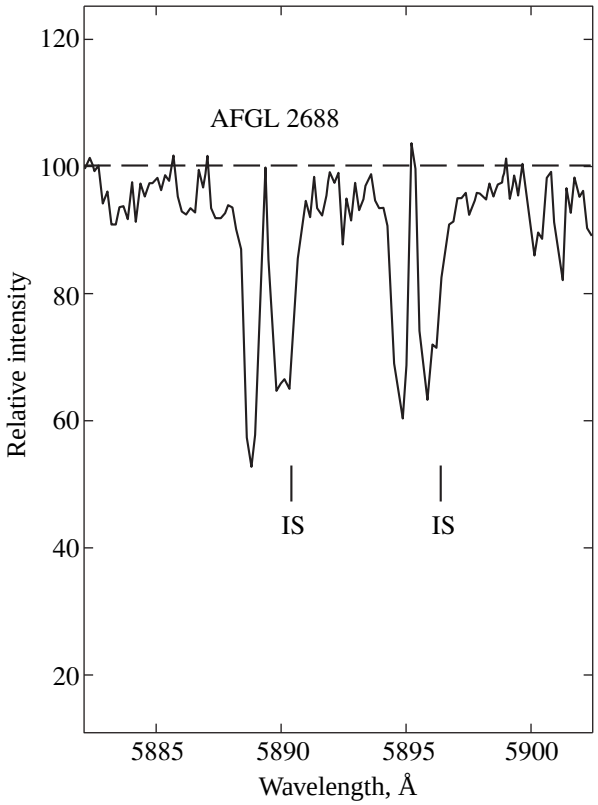

Fig. 4. The sodium doublet in the spectrum of AFGL 2688 for the epoch of observations JD = 2451185.2. The vertical bars mark the positions of interstellar components.

shell, and interstellar components of both doublet lines are clearly resolved. The absorption feature at –70 km s^{-1} appears to originate in the shell (see the corresponding radial velocities of the Hα emission components and the C_2 emission band heads in Table 1). The absorption feature at –19 km s^{-1} is photospheric in origin (the radial velocity deduced from metal lines is –20 km s^{-1}). The feature that Humphreys *et al.* [39] considered as an emission component lies between the shell and photospheric absorption features and does not extend significantly beyond the continuum neither in Fig. 3 of the above paper nor in our Fig. 4. Finally, the absorption feature at a heliocentric velocity of –1.5 km s^{-1} appears to originate in the interstellar medium of the Cygnus arm (the mean heliocentric velocity for this direction in the Galaxy determined by Georgelin and Georgelin [40] from the spectra of H II regions is nearly zero).

It should be emphasized that there is agreement between the radial velocities measured from the Swan emission bands and from the emission component in the Hα profile. The Na I doublet lines also contain the corresponding absorption component, allowing the shell expansion velocity to be estimated (~60 km s^{-1} relative to the velocity measured from photospheric lines); i.e., the existence of the high-velocity stellar wind from AFGL 2688 that was previously detected by Young *et al.* [34] is confirmed.

4.4 Chemical Composition

The final elemental abundances $\log\epsilon(X)$ averaged over the set of measured lines and errors $\pm\delta$ of the means are given in Table 3. The second column in this table gives the corresponding data [41] for the solar atmosphere; we used them to determine

$$[X/\mathrm{Fe}] = [\log\epsilon(X) - \log\epsilon(\mathrm{Fe})]_\star - [\log\epsilon(X) - \log\epsilon(\mathrm{Fe})]_\odot,$$

which are required to analyze the abundance curve at various metallicities. Below, we consider the abundance pattern in the stellar atmosphere in more detail.

Note first the reduced atmospheric metallicity of the object relative to the Sun: [Fe/H] = –0.59. It is also important to note that [Zn/Fe], [Ca/Fe], and [Sc/Fe] are close to their normal values, suggesting that the selective separation of chemical elements in AFGL 2688 is inefficient. The enhanced sulfur abundance, [S/Fe] = +0.47, corresponds to a sulfur overabundance in the atmospheres of unevolved stars of similar metallicity [42]. Consequently, given the normal [Zn/Fe] ratio, we may assert that our derived abundances of iron and other chemical elements subject to condensation on dust grains (primarily Ca and Sc) also reflect the actual chemical composition of the stellar atmosphere.

Enhanced (relative to iron) carbon and nitrogen abundances, [C/Fe] = +0.73 and [N/Fe] = +2.00, were reliably detected (the rms deviations are σ = 0.27 and 0.20 for carbon and nitrogen, respectively) by a large set of spectral lines of these elements. For unevolved stars, [C/Fe] ~ –0.2 and [N/Fe] ~ 0.0 [42, 43]. The large carbon overabundance in the AFGL 2688 atmosphere is consistent with the presence of strong spectral features of carbon-containing molecules in the circumstellar shell. The oxygen overabundance, [O/Fe] = 0.40, was determined by using the equivalent widths of three lines near a wavelength of 6155 Å without regard for the infrared oxygen triplet sensitive to luminosity effects. The C/N/O abundance ratios suggest the detection of evidence for the third mixing and the dredge-up of the material processed during hydrogen and helium burning in the stellar atmosphere. A combination of the reduced metallicity with the CNO abundance pattern (C/O > 1) allows AFGL 2688 to be considered as an old-disk object at the post-AGB evolutionary stage.

The conclusion that the object is at the post-AGB stage is also confirmed by the overabundance (relative to iron) of heavy metals: the s-process elements yttrium and barium (for them, the mean [*X*/Fe] = +0.55), as well as the lanthanides La, Ce, Pr, and Nd ([la/Fe] = +0.26). It should be noted that, for AFGL 2688 studied here, the overabundance of these heavy metals synthesized mostly neutron-capture reactions at low neutron fluxes is small compared to such record-holders as IRAS 07134+1005 [1], IRAS 05341+0852 [44], and IRAS 23304+6147 [11]; in these objects, the average abundances of the above heavy metals are enhanced relative to iron by more than one order of magnitude. In

the spectrum of IRAS 23304+6147, the Ba II lines are the strongest spectral features even in low-spectral-resolution spectra: they are comparable in intensity to the hydrogen lines. In the case of AFGL 2688, however, the barium overabundance relative to iron is at the error level ([Ba/Fe] = +0.25), but we are inclined to believe that this slight overabundance is real, because it is confirmed both by the barium abundance derived from strong lines at λλ6141 and 6496 Å (see Table 2) and by the overabundance of other s-process elements.

AFGL 2688 is occasionally placed into a very limited sample of PPN with carbon-rich shells whose infrared spectra exhibit the 21-μm emission feature. Buss *et al.* [45] found evidence of the corresponding spectral feature in AFGL 2688. However, the intensity of this as yet unidentified band in the spectrum of AFGL 2688 is very weak compared to that for the remaining objects from the sample [46]. Using the UKIRT infrared spectrometers, Justtanont *et al.* [47] detected only a continuum in AFGL 2688 in this region without evidence of the emission feature.

Decin *et al.* [48] and Klochkova [49] conclude that the presence of an emission feature near 21 μm in the infrared spectra of stars at the PPN phase is related to manifestations of the heavy-metal overabundance in their atmospheres. Our results for AFGL 2688 strengthen this conclusion, because this object is characterized both by a slight overabundance of s-process elements and by a virtually indistinguishable 21 μm band against the background of the monotonically increasing infrared continuum.

The ratio of the s-process heavy and light elements [hs/ls] is an important neutronization parameter. For AFGL 2688, this ratio is very low: [Ba/Y] = –0.6; [la/Y] = –0.6 for the group of lanthanides as a whole. According to the calculations by Busso *et al.* [50], this value of [hs/ls] is indicative of an exceedingly low neutron exposure, $\tau_0 \sim 0.15$ mbarn^{-1}. A similar conclusion was reached by Decin *et al.* [48] for IRAS 22223+4327.

Note also the significant europium overabundance relative to iron, [Eu/Fe] = +0.5, was found for AFGL 2688. Such an overabundance of europium, which is synthesized at a high neutron flux density, is typical of metal-poor post-AGB supergiants with enhanced s-process elements: IRAS 07134+1005 [1], IRAS 05341+0852 [44], IRAS 04296+3429 [48, 31], IRAS 22223+4327 [48], and IRAS 23304+6147 [11]. The enhanced [Eu/Fe] is consistent with the behavior of this quantity, depending on stellar metallicity [51].

As follows from Table 2, the spectrum of AFGL 2688 exhibits the Li I 6707 Å resonance doublet line, which leads to an overabundance of this element. Similar results have previously been obtained for two more supergiants identified with infrared sources: IRAS 05341+0852 [44] and IRAS 04296+3429 [31]. It should be emphasized that all three objects are very similar in physical parameters and metallicity. The synthesis of Li nuclei at the AGB stage is possible for a narrow range of luminosities M_{bol} (from –6 to –7 [52]), in agreement with spectroscopy of AGB stars in the Magellanic Clouds [53, 54]. Recall that broadband photometry for AFGL 2688 yields its luminosity $M_{bol} = -5.9$ [15]. Note that an aluminum overabundance was also detected for these three objects (IRAS 05341+0852, IRAS 04296+3429, AFGL 2688) and for IRAS 07134+1005 [1]; this confirms that the lithium overabundance is real, because model calculations [52, 55] predict the production of lithium and aluminum in the envelopes of relatively massive (5–6 $M_\odot$) AGB stars and the dredge-up of these elements to the surface by the third mixing.

The enhancement of the odd α-process element sodium relative to iron, [Na/Fe] = +0.50, was reliably determined from four lines and is confirmed by a similar enhancement of aluminum, whose abundance was estimated less reliably from a single line. In low-luminosity stars with metallicity in the range 0 to –1 dex, [Na/Fe] and [Al/Fe] are nearly zero [42]. The atmospheric sodium overabundance in a supergiant, which, as follows from data on the CNO elements, underwent mixing, can be produced in principle by the dredge-up of sodium accumulated during the previous evolution of the star. However, as was shown by Mashonkina *et al.* [56], the effect of "overrecombination," which is disregarded in LTE calculations of the sodium abundance, contributes to the observed sodium overabundance in the case of high-luminosity stars. An additional factor that strengthens the effects of departures from LTE is the reduced stellar metallicity [57].

4.5 Does AFGL 2688 Belong to the Cyg OB4 Association?

Crampton *et al.* [26] noted that AFGL 2688 probably belongs to the Cyg OB4 association. At the assumed distance of 1 kpc, the object is offset by 110 pc from the Galactic plane. Assuming the infrared emission to be isotropic, Ney *et al.* [15] estimated the bolometric absolute magnitude for the distance of 1 kpc to be $M_b = -5.9$, in good agreement with the luminosity estimated from the spectrum.

Skinner *et al.* [24] estimated the mass-loss rate to be $\dot{M} = 4 \times 10^{-3}\ M_\odot$ yr^{-1}. This value exceeds the mean mass-loss rate for PPN by three orders of magnitude and, as was pointed out by these authors, suggests a high initial mass of AFGL 2688 compared to typical parameters of stars evolving toward the planetary-nebula phase. The evolution rate of a post-AGB star strongly depends on its initial mass: a star of initial mass 5 $M_\odot$ passes through the post-AGB stage a factor of 10 faster than does a 3 $M_\odot$ star [58]. The high initial mass of AFGL 2688 provides evidence for the hypothesis that it belongs to the stellar association.

The assumption of a high initial mass implies that this phenomenon occurs rarely in the Galaxy. However, we know several objects that are morphologically similar to the nebula AFGL 2688. AFGL 2688 belongs to a

small subgroup of bipolar reflection nebulae, which consists of AFGL 618 [59], AFGL 915 [60], and M 1-92 [61].

Our conclusion about the reduced atmospheric metallicity of the central star casts doubt on the hypothesis that AFGL 2688 belongs to the Cyg OB4 association. Humphreys [62] believes the supergiant HD 202850 with $A_v = 0.36$ and radial velocity $V_r = -4.1$ km s^{-1} to be a member of this association. Interferometric observations of the sodium doublet with resolution $R = 600\,000$ [63] reveal from four to six interstellar components in the spectrum of HD 202850 in the range of radial velocities –20 to –2 km s^{-1}, which gives the heliocentric velocity $V_r = -12$ km s^{-1} for the convolution to $R = 15\,000$. The total equivalent width of the interstellar sodium doublet lines in the spectrum of HD 202850, as measured by Hobbs [64], is 0.74 Å. Our radial-velocity determinations for the interstellar medium toward AFGL 2688 yield $V_r = -1.5$ km s^{-1}, and the total equivalent width of the interstellar sodium doublet absorption lines is 0.49 Å. Thus, it cannot be inferred from measurements of the characteristics of the interstellar sodium doublet components that AFGL 2688 belongs to the Cyg OB4 association.

The estimates of interstellar extinction are less reliable. Cohen and Kuhi [27] estimated the total equivalent width of the interstellar sodium doublet absorption lines to be 0.25 Å with an uncertainty of 0.1 Å. This value was subsequently used to determine the interstellar extinction from the correlation between $W(D_1 + D_2)$ and $E(B - V)$ published by Bromage and Nandy [65]. The large interstellar extinction ($A_v = 4.0$) yielded by this procedure is erroneous, because, using the figures from [65] digitized in picometers, Cohen and Kuhi [27] overestimated the equivalent width of the interstellar sodium doublet component in the spectrum of AFGL 2688 by a factor of 10. Actually, an interstellar extinction of even one magnitude is difficult to obtain at $W(D_1 + D_2) = 0.49$ Å, and it should be remembered that the intensity of saturated interstellar sodium doublet lines poorly correlates with the interstellar extinction in continuum.

5. CONCLUSION

Based on echelle spectra obtained with the 6-m telescope, we have analyzed the chemical composition and radial velocities of the northern components of the bipolar structure identified with the intense infrared source AFGL 2688. The reduced (relative to the Sun) atmospheric metallicity, [Fe/H] = –0.59, allows us to classify this object as belonging to the old-disk population and does not confirm that it belongs to the Cyg OB4 association.

The enhanced (relative to iron) carbon and nitrogen abundances, [C/Fe] = +0.73 and [N/Fe] = +2.00, suggest evolutionary changes in atmospheric chemical composition. A combination of the reduced metallicity and the CNO abundance pattern (C/O > 1) allows AFGL 2688 to be considered as a post-AGB object. The fact that it is at the post-AGB stage is also confirmed by a significant overabundance (relative to iron) of the s-process elements yttrium and barium (the mean for them is [X/Fe] = +0.55) and of the lanthanides La, Ce, Pr, and Nd (la/Fe] = +0.26). The abundance ratio of the s-process heavy and light elements suggests an exceedingly low neutron exposure, $\tau_0 \sim 0.15$ mbarn^{-1}.

The overabundance of lithium and aluminum is combined with the object's high luminosity and is consistent with model calculations [52, 55]; these calculations predict the production of lithium and aluminum in the envelopes of relatively massive (5–6 $M_\odot$) AGB stars and the dredge-up of these elements to the surface by the third mixing.

We use the object under study as an example and a set of spectra for related objects to show that the cold circumstellar shells, which manifest themselves in molecular absorption lines, are very extended and can also exhibit molecular emission features. The expansion velocities of the AFGL 2688 shell measured from the absorption (sodium doublet) and emission (Hα and C_2) spectra are essentially the same.

ACKNOWLEDGMENTS

We wish to thank the Russian Federal Program "Astronomy" (project no. 1.4.1.1), the Russian Foundation for Basic Research (project no. 99-02-18339), and the Polish State Research Committee (project nos. 2.P03D.026.09, 2.P03D.002.13, and 2.P03D.002.017) for supporting the spectroscopic study of anomalous supergiants with infrared excesses.

REFERENCES

1. V. G. Klochkova, Mon. Not. R. Astron. Soc. **272**, 710 (1995).
2. V. G. Klochkova, Bull. Spec. Astrophys. Obs. **44**, 5 (1998).
3. L. Zaĉs, V. G. Klochkova, and V. E. Panchuk, Mon. Not. R. Astron. Soc. **275**, 764 (1995).
4. L. Zaĉs, V. G. Klochkova, V. E. Panchuk, and R. Spẽlmanis, Mon. Not. R. Astron. Soc. **282**, 1171 (1996).
5. V. G. Klochkova and V. E. Panchuk, Bull. Spec. Astrophys. Obs. **41**, 5 (1996).
6. V. G. Klochkova and V. E. Panchuk, Pis'ma Astron. Zh. **24**, 754 (1998) [Astron. Lett. **24**, 650 (1998)].
7. V. G. Klochkova and T. V. Mishenina, Bull. Spec. Astrophys. Obs. **44**, 83 (1998).
8. V. G. Klochkova, E. L. Chentsov, and V. E. Panchuk, Astron. Astrophys. **323**, 789 (1997).
9. V. G. Klochkova, E. L. Chentsov, and V. E. Panchuk, Mon. Not. R. Astron. Soc. **292**, 19 (1997).
10. V. G. Klochkova, R. Szczerba, and V. E. Panchuk, Astrophys. Space Sci. **255**, 485 (1997).
11. V. G. Klochkova, R. Szczerba, and V. E. Panchuk, Pis'ma Astron. Zh. **26**, 115 (2000) [Astron. Lett. **26**, 88 (2000)].

12. S. Kwok, Ann. Rev. Astron. Astrophys. **31**, 63 (1993).
13. M. Forestini and C. Charbonnel, Astron. Astrophys., Suppl. Ser. **123**, 241 (1997).
14. E. P. Ney, Sky Telesc. **49**, 21 (1975).
15. E. P. Ney, K. M. Merrill, E. E. Beklin, *et al.*, Astrophys. J. Lett. **198**, L129 (1975).
16. W. J. Forrest, K. M. Merrill, R. W. Russell, and B. T. Soifer, Astrophys. J. Lett. **199**, L181 (1975).
17. E. W. Gottlieb and W. Liller, Astrophys. J. Lett. **207**, L135 (1976).
18. G. D. Schmidt, J. R. P. Angel, and E. A. Beaver, Astrophys. J. **219**, 477 (1978).
19. V. E. Panchuk, I. D. Najdenov, V. G. Klochkova, *et al.*, Bull. Spec. Astrophys. Obs. **44**, 127 (1998).
20. B. Gustafsson, R. A. Bell, K. Eriksson, and A. Nordlund, Astron. Astrophys. Suppl. Ser. **42**, 407 (1975).
21. R. E. Luck, Astrophys. J., Suppl. Ser. **75**, 579 (1991).
22. C. Waelkens, H. van Winkel, E. Bogaert, and N. R. Trams, Astron. Astrophys. **251**, 495 (1991).
23. S. Giridhar, N. K. Rao, and D. Lambert, Astrophys. J. **437**, 476 (1994).
24. C. J. Skinner, M. Meixner, M. J. Barlow, *et al.*, Astron. Astrophys. **328**, 290 (1997).
25. J. L. Hora and W. B. Latter, Astrophys. J. **437**, 281 (1994).
26. D. Crampton, A. Cowley, and R. Humphreys, Astrophys. J. Lett. **198**, L135 (1975).
27. M. Cohen and L. V. Kuhi, Astrophys. J. **213**, 79 (1977).
28. E. J. Bakker, E. F. van Dishoeck, L. B. F. M. Waters, and T. Schoenmaker, Astron. Astrophys. **323**, 469 (1997).
29. M. Cohen and L. V. Kuhi, Publ. Astron. Soc. Pac. **92** (549), 736 (1980).
30. B. J. Hrivnak, Astrophys. J. **438**, 341 (1995).
31. V. G. Klochkova, R. Szczerba, V. E. Panchuk, and K. Volk, Astron. Astrophys. **345**, 905 (1999).
32. J. L. Greenstein, Astrophys. J. **128**, 106 (1958).
33. O. V. Dobrovol'skiĭ, *Comets* (Nauka, Moscow, 1966).
34. K. Young, G. Serabyn, T. G. Phillips, *et al.*, Astrophys. J. **385**, 265 (1992).
35. G. R. Knapp, Astrophys. J. **311,** 731 (1986).
36. D. Schönberner, Astrophys. J. **272**, 708 (1983).
37. M. Jura and H. Kroto, Astrophys. J. **351**, 222 (1990).
38. K. Y. Lo and K. P. Bechis, Astrophys. J. Lett. **205**, L21 (1976).
39. R. M. Humphreys, J. W. Warner, and J. S. Gallagher, Publ. Astron. Soc. Pac. **88**, 380 (1976).
40. Y. P. Georgelin and Y. M. Georgelin, Astron. Astrophys. **6**, 349 (1970).
41. N. Grevesse, A. Noels, and A. J. Sauval, Astron. Soc. Pac. Conf. Ser. **99**, 117 (1996).
42. F. X. Timmes, S. E. Woosley, and T. A. Weaver, Astrophys. J., Suppl. Ser. **98**, 617 (1995).
43. J. C. Wheeler, C. Sneden, and J. W. Truran, Jr., Ann. Rev. Astron. Astrophys. **27**, 279 (1989).
44. B. E. Reddy, M. Parthasarathy, G. Gonzáles, and E. J. Bakker, Astron. Astrophys. **328**, 331 (1997).
45. R. H. Buss, A. G. G. M. Tielens, M. Cohen, *et al.*, Astrophys. J. **415**, 250 (1993).
46. A. Omont, S. H. Moseley, P. Cox, *et al.*, Astrophys. J. **454**, 819 (1995).
47. K. Justtanont, M. J. Barlow, C. J. Skinner, *et al*., Astron. Astrophys. **309**, 612 (1996).
48. L. Decin, H. van Wickel, C. Waelkens, and E. J. Bakker, Astron. Astrophys. **332**, 928 (1998).
49. V. G. Klochkova, *Bukov's Lectures,* Ed. by O. Verkhodanov (Spets. Astrofiz. Observ., Nizhniĭ Arkhyz, 1998), p. 19.
50. M. Busso, D. L. Lambert, L. Beglio, *et al.*, Astrophys. J. **446**, 775 (1995).
51. V. M. Woolf, J. Tomkin, and D. I. Lambert, Astrophys. J. **453**, 660 (1995).
52. I.-J. Sackmann and A. I. Boothroyd, Astrophys. J. Lett. **392**, L71 (1992).
53. V. V. Smith and D. L. Lambert, Astrophys. J. Lett. **345**, L75 (1989).
54. V. V. Smith and D. L. Lambert, Astrophys. J. Lett. **361**, L69 (1990).
55. N. Mowlavi, *The Light Elements Abundances*, Ed. by P. Crane (Springer-Verlag, New York, 1995), p. 297.
56. L. I. Mashonkina, V. V. Shimanskiĭ, D. Ivanova, and N. A. Sakhibullin, Astron. Zh. (1999) (in press).
57. D. Baumüller, T. Butler, and T. Gehren, Astron. Astrophys. **338**, 637 (1998).
58. T. Blöker, Astron. Astrophys. **299**, 755 (1995).
59. W. E. Westbrook, E. E. Becklin, K. M. Merrill, *et al.*, Astrophys. J. **202**, 407 (1975).
60. M. Cohen, C. M. Anderson, A. Cowley, *et al.*, Astrophys. J. **196**, 179 (1975).
61. G. H. Herbig, Astrophys. J. **200**, 1 (1975).
62. R. M. Humphreys, Astrophys. J., Suppl. Ser. **38**, 309 (1978).
63. L. M. Hobbs, Astrophys. J. **157**, 135 (1969).
64. L. M. Hobbs, Astrophys. J. **191**, 381 (1974).
65. G. E. Bromage and K. Nandy, Astron. Astrophys. **26**, 17 (1973).

Translated by V. Astakhov

Astronomy Letters, Vol. 26, No. 7, 2000, pp. 452–459. Translated from Pis'ma v Astronomicheskiĭ Zhurnal, Vol. 26, No. 7, 2000, pp. 525–534.

A Photometric Study of the Star V1016 Ori

N. I. Bondar'[1], É. A. Vitrichenko[2]*, and M. M. Zakirov[3]

[1] *Crimean Astrophysical Observatory, p/o Nauchnyĭ, Crimea, 334413 Ukraine*
[2] *Space Research Institute, Russian Academy of Sciences, ul. Profsoyuznaya 84/32, Moscow, 117810 Russia*
[3] *Astronomical Institute, Academy of Sciences of Uzbekistan, Astronomicheskaya ul. 33, Tashkent, 700052 Uzbekistan*

Received July 8, 1999; in final form, December 23, 1999

Abstract—New photoelectric *UBVRI* observations of the eclipsing variable V1016 Ori have been obtained with the AZT-11 telescope at Crimean Astrophysical Observatory and with the Zeiss-600 telescope at Mount Maidanak Observatory. Light curves are constructed from the new observations and from published and archival data. We use a total of 340, 348, 386, 185, and 62 magnitude estimates in the bands from *U* to *I*, respectively. An analysis of these data has yielded the following results. The photometric elements were refined; their new values are Min I = JDH 2441966.820 + $65^{d}.4331E$. The *UBVRI* magnitudes outside eclipse were found to be $5^{m}.95$, $6^{m}.77$, $6^{m}.75$, $6^{m}.68$, and $6^{m}.16$, respectively. No phase effect was detected. We obtained two light-curve solutions: (1) assuming that the giant star was in front of the small one during eclipse, we determined the stellar radii, $r_s = 0.0141$ and $r_g = 0.0228$ (in fractions of the semimajor axis of the orbit); and (2) assuming that the small star was in front of the giant one, we derived $r_g = 0.0186$ and $r_s = 0.0180$ for the *V* band. The brightness of the primary star in the bands from *U* to *I* is $L_1 = 0.96$, 0.92, 0.90, 0.89, and 0.88, the orbital inclination is $i = 87^{\circ}.1$, and the maximum eclipse phase is $\alpha_0 = 0.66$. In both cases, we accepted the *U* hypothesis, assumed the orbit to be elliptical, and took into account the flux from the star Θ^1 Ori E that fell within the photometer aperture. The first solution leads to a discrepancy between the primary radius determined by solving the light curve and the radial-velocity curve and its value estimated from the luminosity and temperature. This discrepancy is eliminated in the second solution, and it turns out that, by all parameters, the primary corresponds to a normal zero-age main-sequence star. © *2000 MAIK "Nauka/Interperiodica"*.

Key words: *stars—variable and peculiar*

INTRODUCTION

The eclipsing system V1016 Ori (=HD 37020 = Θ^1 Ori A = P1865 = Bond 619) is a member of the Orion Trapezium. Its orbital period is 65.4 days, the magnitude at maximum is $V = 6^{m}.7$, and the spectral type of the primary star is B0 V. Lohsen [1] discovered photometric variability and established the eclipsing nature of this variability. This author also constructed the first radial-velocity curve [2]. Vitrichenko *et al.* [3] refined the spectroscopic orbital elements. A study of the stellar continuum over a wide wavelength range has revealed four sources of radiation: a B0 V primary, an A0 V secondary, dust with temperature $T_d = 1600$ K, and an infrared source with $T_{eff} \sim 3000$ K [4]. The star Θ^1 Ori A1 lying $0''.2$ north of the binary system could be this infrared source [5]. It was discovered by speckle interferometry.

This star is of interest primarily because it is young. Since the age of the Orion Trapezium is estimated to be 10^5–10^6 years, studying V1016 Ori can broaden our knowledge about the earliest stages of stellar evolution.

The star exhibits several peculiarities.

Bossi *et al.* [6] found that the primary radius estimated from the light and radial-velocity curves was abnormally small, and that its value disagreed with the radius determined from the temperature and luminosity.

According to the light-curve solution obtained by Zakirov [7] by assuming a total eclipse, the components are comparable in brightness ($L_s = 0.58$). In that case, however, the spectrum of the cooler secondary component must be seen, which is not observed. The above properties of V1016 Ori suggest that the secondary is not a normal star.

A cloud of gas emitting radiation at wavelengths of 2 and 6 cm was discovered in the vicinity of V1016 Ori [8, 9]. There is no such cloud around other Orion Trapezium stars. An outburst of this cloud was recorded. The fine structure of the cloud was studied during elongation of the components, and two features, which coincided with the components' positions calculated from the spectroscopic orbital elements, were detected.

* E-mail address for contacts: vitrich@nserv.iki.rssi.ru

It is thus concluded that two clouds of gas are localized near each of the components.

X-ray emission was detected from the Orion Trapezium region [10, 11]. An X-ray flare was recorded near V1016 Ori [10]. X-ray emission was also detected from other star-forming regions [12]. This finding is especially interesting, because it cannot be interpreted in terms of the current theory of stellar evolution.

Vitrichenko and Klochkova [13] analyzed the stellar spectrum. Two-dimensional spectral classification yielded the following atmospheric parameters: $T_{\rm eff}$ = 29700 K and $\log g = 4.4$. The projected rotational velocity is $V\sin i = 60$ km s^{-1}. An abundance analysis shows that the iron abundance is nearly solar; He, C, O, Mg, Al, and Si are underabundant, while Ne, S, and Zn are overabundant.

Meanwhile, the star has not been studied adequately. No complete light curve has been constructed, because most of the photoelectric observations were obtained near primary minimum. Many observers disregarded the flux from the star Θ^1 Ori E that fell within the photometer aperture.

The eclipse geometry is still a controversial issue. Some observers believe the eclipse to be total, while others suggest a partial eclipse. The light curve was solved under three distinct assumptions. In the first case, the orbit was assumed to be circular [7]. However, an analysis of the radial-velocity curve yielded a large eccentricity, $e \sim 0.7$ [3]. In the second case, orbital ellipticity was taken into account [14]. In the third case, it was assumed that the secondary star was surrounded by a dust shell, and that the eclipse was mainly produced by this shell and, only partly, by the secondary [15]. These three assumptions yield inconsistent results.

Here, our objectives are as follows: (1) to determine the brightness of Θ^1 Ori E in order to allow for the flux from this star; (2) to construct a complete light curve and to study the system's brightness outside eclipse; (3) to refine the depth of the primary minimum; (4) to estimate the spectral type of the secondary star from the depths of the minima in several bands; and (5) to solve the light curve for an elliptical orbit and a partial eclipse, but using the eclipse pattern with the small star lying in front of the giant one. We seek for this solution in an effort to resolve the paradox with the radius of the primary star.

OBSERVATIONS AND THEIR ANALYSIS

In 1990–1991, 68 *UBVR* magnitude estimates of the star were obtained with the Zeiss-600 telescope at Mount Maidanak. Star E did not fall within the photometer aperture during the exposure. These observations were carried out by one of us (M. Zakirov) and are called below the new observations to distinguish them from previously published ones [7].

In 1995–1999, 62 *UBVRI* magnitude estimates of the star were obtained with the AZT-11 telescope at Crimean Astrophysical Observatory. The observers were N. Bondar' and É. Vitrichenko. V361 Ori and V372 Ori served as the comparison and check stars, respectively, whose brightness was constant [16]. The observing and reduction techniques are described in the above paper. The only peculiarity of the data reduction technique was that we took into account the flux from Θ^1 Ori E (below called star E), which was located at 4″ from V1016 Ori and fell within the photometer aperture. On nights with the best seeing, the brightness of star E was measured many times. An analysis of these measurements shows that star E is constant, and that its magnitudes in the bands from *U* to *I* are, respectively,

$$m = 9^m.2(1),\quad 10^m.10(7),\quad 9^m.91(5),\quad 9^m.01(3),\quad 8^m.45(6). \qquad (1)$$

Table 1. Photoelectric observations of V1016 Ori

Author, reference	N	Band
Lohsen [1]	43	*UBV*
Walker [23]	3	*V*
Walker [24]	3	*UBV*
Caton *et al*. [25]	70	*UBV*
Franz [26]	28	*UBV*
Zakirov [7]	38	*UBVR*
Sowell and Hall [27]	21	*UBV*
Shevchenko	10	*UBVR*
This paper	130	*UBVRI*

We collected all the available published and archival photoelectric measurements of V1016 Ori. They are given in Table 1. Here, *N* is the number of magnitude estimates. We used a total of 340, 348, 386, 185, and 62 magnitude estimates in the bands from *U* to *I*, respectively.

Brief explanations for Table 1 are given below.

We did not find Lohsen's measurements of V1016 Ori [1] in the literature in tabular form and took individual measurements from the graph in the original paper.

The measurements by Sowell and Hall [27] are stored at the Astronomical Data Center (ADS), whose staff kindly provided them at our request.

V.S. Shevchenko provided us with *UBVR* magnitude estimates from his personal unpublished archive. The observations were performed at Mount Maidanak Observatory.

The last row in Table 1 gives the number of our observations.

The magnitude estimates in Table 1 are highly inhomogeneous in the method of allowance for background and for the light from star E. In all these observations, except Lohsen's studies [1] and Zakirov's new measurements, star E fell within the aperture, and its flux was disregarded. We reanalyzed these observations and subtracted the flux from star E. The observers used different comparison stars; the authors often provide magnitude differences relative to the comparison star, and

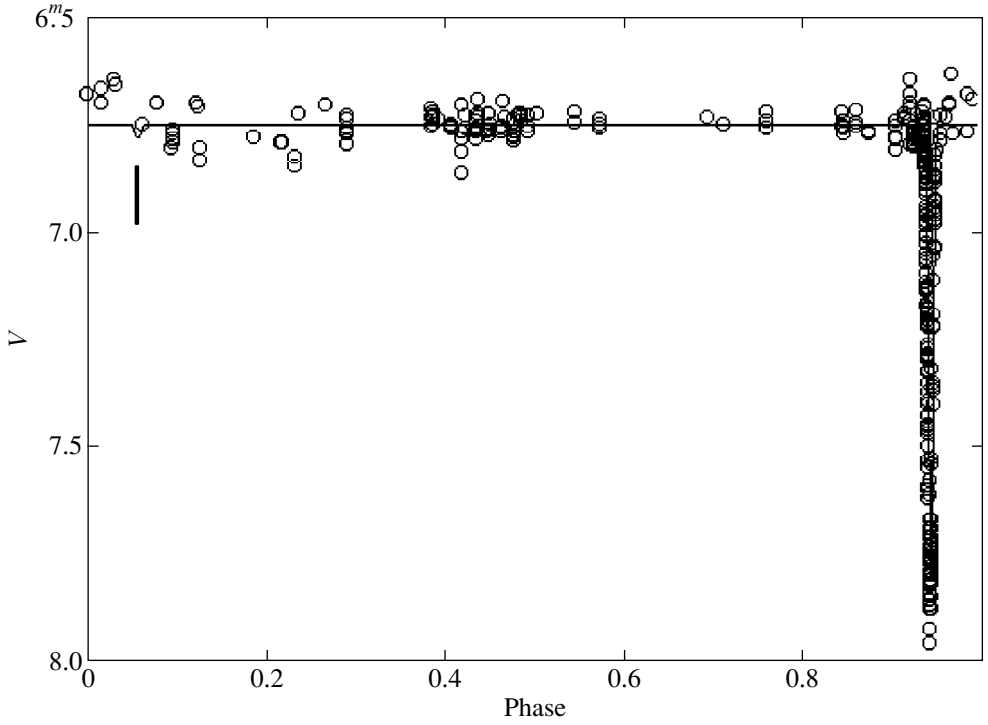

Fig. 1. Complete *V* light curve for V1016 Ori. The observations are indicated by circles; the solid line represents the theoretical light curve. The phase is measured from the stars' periastron passage. The bar marks the position of the secondary minimum.

we had to reduce all observations to a single system. The corrections to the observations of different authors taken to reduce the observations to a single system are mainly of the order of a few hundredths of a magnitude, and we took them into account. However, there are two special cases associated with instability of the light curve.

The first case refers to the Lohsen's *U* observations [1]. These observations were obtained near totality, but they disagree with the observations of other authors. The star turns out to be brighter by $0^m.26$, which is considerably larger than the observational errors. There is no such effect in *B* and *V*. We failed to account for this phenomenon. We can only assume that either the star was in the state of enhanced brightness in *U* alone, or a systematic error was made when reducing the observations.

The second case refers to Zakirov's new observations. His previous observations [7] and the observations by other authors are in good agreement with the *R* magnitude outside eclipse of $6^m.68$. However, the 1991–1992 observations show that $R = 6^m.33$ at that time. The star proved to be brighter by $0^m.35$, which cannot be explained by random errors. At the same time, the *UBV* observations are in good agreement with those of other authors. In this regard, the same two assumption as those for Lohsen's observations can be made.

We do not give the star's observations here because they take much space, but they were sent to the Astronomical Data Center as the file v1016ori.obs.

THE BRIGHTNESS OUTSIDE ECLIPSE AND AT MINIMUM

Figure 1 shows a complete *V* light curve. The rms error of a single measurement in this band for the entire set of measurements is $0^m.027$. The relatively large error stems from the fact that the star lies low above the horizon ($z > 50°$), and that the star is observed in winter, when the weather is unstable. For the other bands, the error is of the same order of magnitude.

When we constructed this curve, the need for adjusting the photometric elements arose. Their new values are

$$\mathrm{MinI} = \mathrm{JDH}\ 2441966.820(1) + 65^d.4331(2) \cdot E. \quad (2)$$

In what follows, the errors given in parentheses are estimates, because we used the trial-and-error method when analyzing the observations.

Similar light curves were also constructed for the other bands.

It can be inferred from an examination of Fig. 1 that there is no phase effect. An attempt to calculate this effect by using classical formulas yields reflection and ellipticity coefficients of $\sim 0^m.01$, which, in order of magnitude, matches the errors in these coefficients.

However, the classical formula does not apply to this case anyway because of the orbital ellipticity. Determining the rectification coefficients with allowance for orbital ellipticity also shows them to be insignificant. One would expect the rise in brightness attributable to the reflection effect to be more appreciable near the secondary minimum and in the *U* band. However, no such brightness rise was detected. It would be unreasonable to expect any phase effect, because the stellar radii (in fractions of the relative orbit) are small. The system is detached.

No evidence of flare activity is seen on the light curve. The check star shows the same error of a single measurement as does the star under study. The two examples of brightness rise given above are long-term rises in brightness rather than flares with a time scale of ~2 h, which are observed in the star BM Ori [17].

In Fig. 1, the rectilinear segment indicates the location of the secondary minimum. Its depth must be $\sim 0^m.03$. We see from the scatter of observations that this minimum cannot be detected at the given accuracy of observations. It should be borne in mind that the theoretical curve was calculated for an ordinary eclipse: the star occults the star. If the eclipse were produced by the surrounding dust cloud, then the depth of the secondary minimum would be even smaller.

We see from Fig. 1 that many observations concentrate near phase 0.5 relative to the primary minimum. This is because many observers searched for the secondary minimum precisely at this location, while at the location on the light curve where the minimum must actually be (marked by the segment), there are virtually no observations. Obtaining new highly accurate observations near the secondary minimum is therefore an important observational task.

The weighted (by the number of observations) mean magnitudes outside eclipse are listed in Table 2. The abnormal *R* magnitudes (Zakirov's new observations) were excluded. The magnitudes from [18] are given for comparison. The agreement between both determinations is satisfactory, with the exception of the star's *R* magnitude, which can be explained by well-known difficulties in reproducing the standard system or by stellar variability in this band.

Figure 2 shows the observations near the minimum for the case where the giant star was in front of the small one during eclipse (GS hypothesis). We see from an examination of this figure that, after the reduction described above, there is satisfactory agreement between the observations of all authors. Individual outlying observations were reported by the authors to have been performed during bad weather.

We singled out the range of phases from 0.9455 to 0.9475 near the central eclipse phase and averaged all observations in this range in an effort to estimate the observed depth of the minimum. Its values are given in the next-to-last row of Table 2. The depths of the minima from [7] are listed in the last row. The difference goes far outside the error limits, which can be explained by the fact that the author did not reduce the observations to allow for the contribution of star E, whose magnitudes had not been known at that time.

Figure 3 shows the primary-minimum region, but the theoretical curve was drawn for the case where the small star was in front of the giant one (SG hypothesis). A comparison of Figs. 2 and 3 indicates that both hypotheses are in satisfactory agreement with the observations. In Fig. 3, there is an appreciable systematic difference between the observed and theoretical light curves at the beginning of the descending branch, but it can be explained either by reduction errors in the observations of different authors or by the neglect of limb darkening in the primary star. The influence of errors in the solution of the spectroscopic orbit is also possible.

In Table 3, both solutions are compared with each other. The most important result of this comparison is that the radius of the primary star for the SG hypothesis turns out to be a factor of 1.3 larger than that for the other hypothesis. This allows better agreement between the primary radius determined from the temperature and luminosity and its value calculated from the elements of the radial-velocity and light curves to be achieved [13]. The paradox with the primary radius, which was first pointed out by Bossi *et al.* [6], is thus resolved. In this sense, the light-curve solution for the SG hypothesis is more credible than that for the GS hypothesis.

If we accept the SG hypothesis, then all parameters of the primary (radius, mass, absolute magnitude, and temperature) correspond to a normal zero-age main-sequence (ZAMS) star.

ESTIMATING THE SPECTRAL TYPE OF THE SECONDARY STAR

Vitrichenko [19] proposed a method of determining the maximum eclipse phase, the components' brightness ratio, and the spectral type of the secondary from the observed depths of the minimum in several bands. The basic equation to be solved by the least-squares method is

$$\beta_i = (\alpha_i a_1 + 1)/(\alpha_i a_2 + 1), \quad (3)$$

where $\beta = 10^{-0.4\Delta m}$ is the star's brightness at the central eclipse phase for each of the *UBVRI* bands, Δm is the observed depth of the minimum, $\alpha = F_1/F_2$ is the flux ratio of the primary and secondary stars for the *UBRI* bands in the case where these fluxes in *V* are equal, and a_1 and a_2 are the sought-for parameters; $a_1 = (1 - \alpha_0)a_2$, where α_0 is the maximum eclipse phase.

The spectral type of the primary star was estimated from the spectrum to be Sp_1 = B0(1) [13], in agreement with Sp_1 = B1 V obtained by Ismailov [20]. We chose the spectral type of the secondary in such a way that the

Table 2. Magnitudes outside eclipse and the depths of the minima

Quantity	*U*	*B*	*V*	*R*	*I*
Magnitude outside eclipse	$5^m.95(3)$	$6^m.77(2)$	$6^m.75(1)$	$6^m.68(2)$	$6^m.16(1)$
Lee [18]	5.86	6.72	6.72	6.41	6.20
Depth of minimum	1.10(3)	1.02(2)	1.00(1)	0.98(2)	0.95(2)
Zakirov [7]	1.02(1)	0.95(1)	0.93(1)	0.82(1)	

rms residual between the observed and calculated depths of the minima was at a minimum. Sp_2 = B8(2) is in best agreement with the observations, which is inconsistent with Ismailov's assumption [20] that the spectral type of the secondary is later than F2. However, it agrees well with Zakirov's estimate of the spectral type [7] and with the estimate obtained by Bossi *et al.* [6] from the secondary mass $M_2 = 2.6(1)\ M_\odot$.

Solving the set of equations (3) by the least-squares method yielded the following results:

$$\alpha_0 = 0.66(3),$$
$$L_1 = 0.96(2), 0.92(2), 0.90(2), 0.89(2), 0.88(2) \quad (4)$$

for the *UBVRI* bands, which corresponds to the magnitude difference between the components in these bands

$$\Delta m = 3^m.45(2),\quad 2^m.96(2),\quad 2^m.39(2),\quad 2^m.27(2),\quad 2^m.16(2). \quad (5)$$

These data are in satisfactory agreement with those of Bossi *et al.* [6] but are in conflict with Zakirov's results [7]. It should be borne in mind that the solution to the set of equations (3) is unstable, because the energy distribution for B0 and B8 stars are closely correlated. For this reason, the error can be considerably larger than that given here.

The maximum eclipse phase $\alpha_0 = 0.74(3)$ in Table 3 taken from [14] is in satisfactory agreement with its value obtained by analyzing the depths of the minima [see (4)]. The discrepancy can be explained by the fact that the set of equations (3) is ill-conditioned because of the close correlation between the energy distributions for the primary and secondary stars. Therefore, $\alpha_0 = 0.74$ is more credible.

In Fig. 4, the depth of the minimum is plotted against wavelength. When constructing the theoretical dependence, we assumed the B8 star to obscure 66% of the area of the B0 star. Given the observational errors, the agreement between observations and theory may be considered satisfactory. The rms deviation of the observations from the theoretical curve is $0^m.008$.

The time interval between the central eclipse phase and the stars' periastron passage is $\Delta Ep = 3.67(1)$ days. At conjunction, the separation between the stellar centers is 0.564 of the semimajor axis of the orbit.

The information about the star obtained here allows the absolute magnitudes to be estimated for the system

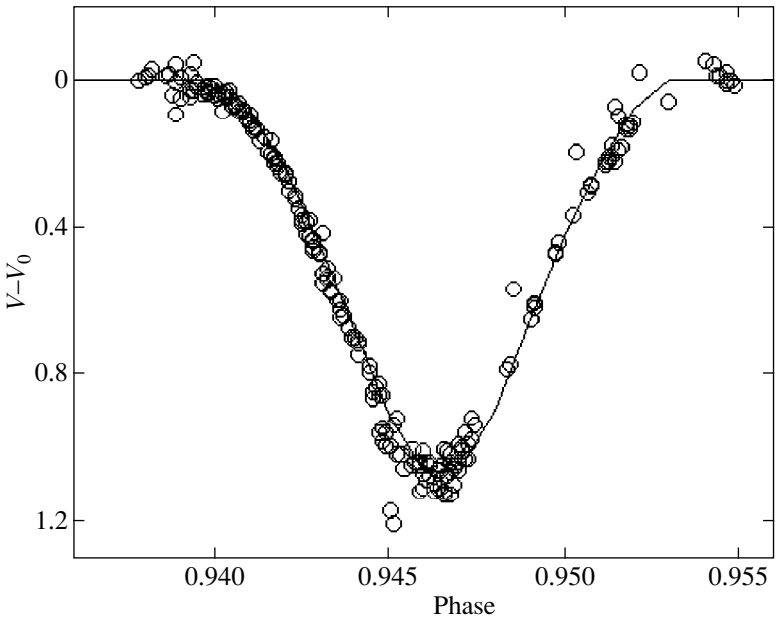

Fig. 2. Region of the primary minimum of the *V* light curve for V1016 Ori (GS hypothesis). The notation is the same as in Fig. 1.

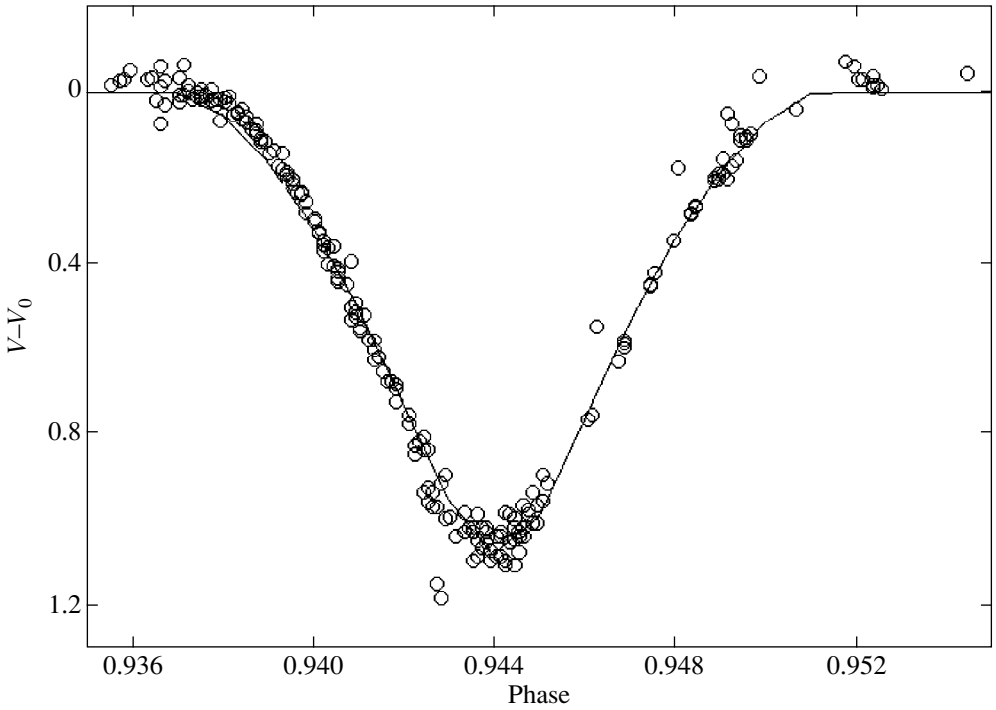

Fig. 3. Region of the primary minimum of the *V* light curve for V1016 Ori (SG hypothesis).

as a whole and for each component. For the system, we have

$$M_v = V - (m - M) - A_v$$
$$= 6^m.75 - 8^m.22 - 0^m.85 = -2^m.32(5),$$

where $V = 6^m.75(1)$ is the star's magnitude outside eclipse, $m - M = 8^m.22(5)$ is the distance modulus for the system, and $A_v = 0^m.85(5)$ is the interstellar extinction [4]. The error in M_v is attributable to the errors in the assumed distance modulus and in the interstellar reddening.

For the absolute magnitude of the primary star to be estimated, the secondary's contribution $\Delta m = 0^m.11$ to the total flux must be taken into account. We then have

$$M_v(\text{prim}) = M_v + \Delta m = -2^m.21(5),$$

in agreement with the spectral type B1 ZAMS, for which $M_v = -2^m.3$ [21].

The secondary has the absolute magnitude

$$M_v(\text{sec}) = M_v(\text{prim}) + \Delta m_1 = +0^m.07(5),$$

where $\Delta m_1 = 2^m.39$ is our previously determined magnitude difference between the secondary and primary stars. For the main sequence, this value corresponds to the spectral type B8.5 [21], in good agreement with the spectral type estimated by analyzing the depths of the minima. Bossi *et al.* [6] believe the secondary to be an active T Tau star but give no convincing arguments for this suggestion. Alluding to an estimate of its mass, Zakirov [7] believes the secondary to be of spectral type B8 V.

According to Van Altena *et al.* [22], all stars in the Orion Nebula region with spectral types earlier than A0 closely fall near the ZAMS line if the distance is assumed to be 440 pc. In that case, both the primary and the secondary may be assumed to also belong to the ZAMS. Their photometric and spectroscopic characteristics are consistent with this assumption. Both stars were plotted on the Hertzsprung–Russell diagram [4], and it turned out that the primary star lay exactly on the ZAMS, while the secondary star was near the ZAMS but had not yet reached it.

Table 3. Photometric elements

Quantity	GS hypothesis	SG hypothesis
r_s	0.0141(5)	0.0180(5)
r_g	0.0228(5)	0.0186(5)
i, deg	87.05(3)	88.4(1)
L_s, *V*	0.90(2)	0.96(2)
α_0	0.74(3)	0.66(3)

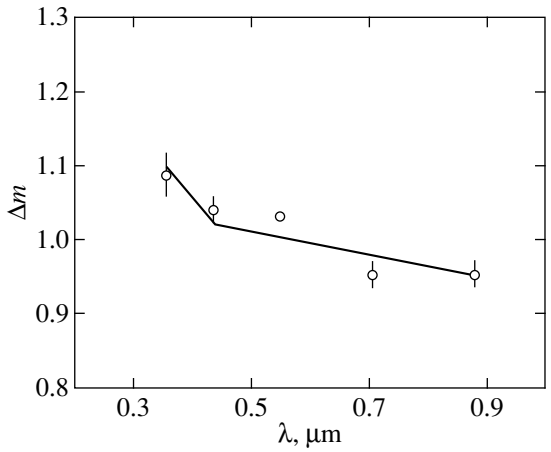

Fig. 4. Depth of the minimum versus wavelength. The observations are indicated by circles; the solid line represents the theoretical curve for the case where a B8 star obscures a B0 star with the maximum eclipse phase $\alpha_0 = 0.66$. The observational errors are indicated by bars.

DISCUSSION

As has already been pointed out above, the key question is the pattern of eclipse: Is it total or partial? Is the eclipse ordinary (star occults star) or is the secondary star unusual in nature?

There are two strong arguments for a partial eclipse.

If we accept the hypothesis of a total eclipse, then it follows from the light-curve solution that both components are comparable in brightness. In that case, however, lines of the secondary, definitely cooler component must be observed in the spectrum outside eclipse as well. We have two spectrograms of the star at our disposal, which were taken by V.G. Klochkova using the 6-m telescope with a signal-to-noise ratio of ~200 and ~0.4 Å resolution in the wavelength range from 4165 to 7000 Å [13]. We compared these spectra with the spectrum of a B8 star and found no clear evidence for lines of this type of star. It may thus be concluded that $L_s/L_g \geq 10$, in agreement with the above brightness estimates for the components but inconsistent with the hypothesis of a total eclipse. For a total eclipse, $L_s/L_g \sim 1$ [7].

The star reddens during an eclipse. On the one hand, this implies that the secondary is cooler than the primary, but, on the other hand, the change in color suggests that the eclipse can be only partial. For example, the observed *U–B* color changes by $0^m.05$. If, however, an F star obscures a B1 star (as assumed by Ismailov [20]), then the change in *U–B* must be $\sim 1^m$, which is not observed. If we take our estimated spectral types of the stars, then the change in this color will be $0^m.65$ for a total eclipse, which is not observed either.

Thus, the hypothesis of a total eclipse is untenable.

Let us consider the question of whether the eclipse can be ordinary, i.e., star eclipses star (GS hypothesis). We assume the effective temperatures of the primary and secondary stars to be $T_1 = 30\,000$ K and $T_2 = 11\,500$ K, in accordance with their spectral types [3]. The ratio of the stellar radii is $k = r_s/r_g = 0.5$. The brightness ratio of the stars can then be estimated by using the standard formula

$$L_s/L_g = (T_1/T_2)k^2 = 0.65. \quad (6)$$

The magnitude difference is $\sim 0^m.5$; the primary turns out to be fainter than the secondary, in conflict with both spectroscopic and photometric observations. The spectrum exhibits lines of the B0 star alone. It follows from the radial-velocity curve that the B0 star lies behind the secondary during eclipse. Finally, the star's reddening at minimum light also implies that the cooler star is in front of it. This contradiction can be resolved by assuming that the secondary radius obtained by solving the light curve refers not to the secondary star but to a semitransparent dust shell around it. The eclipse is produced by this dust shell.

However, the difficult question of whether dust can survive near a hot (secondary) star in the radiation field of an even hotter primary star arises under this assumption. This question was considered by Vitrichenko [15], who showed that dust cannot consist of graphite particles, as they evaporate. However, if dust particles are transparent in the visible (for example, SiO_2, SiC, Al_2O_3), then such dust does not evaporate. Vitrichenko [15] also solved the light curve for V1016 Ori by assuming that the eclipse was mainly produced by the dust shell and, in part, by the secondary disk. This solution is consistent with observations.

Here, we have shown that the hypothesis that the small cool star lies in front of the giant one during eclipse is consistent with observations. This hypothesis allows us to resolve the paradox with the primary radius and to avoid introducing a dust shell around the secondary star. However, a new problem arises in this case: if the dust shell emits no radiation, then to what source can the infrared excess be attributed? Yet another object emitting infrared radiation may fall within the photometer aperture. The star Θ^1 Ori A1 could be this object [5].

One of the most important observational tasks is to obtain a spectrum at the central eclipse phase. More than a hundred spectra were taken for the star, with none of them at minimum light. One might expect that it is easier to find secondary lines at minimum light, which will make it possible to elucidate its nature and thus the pattern of eclipse.

CONCLUSION

We have constructed complete *UBVRI* light curves by using our new observations, as well as published and unpublished archival data. Both the complete light curves and the *I* observations have been obtained for the first time. We measured the brightness of Θ^1 Ori E

in five bands and took into account the flux from this star when reducing the observations. This caused the depth of the minima to increase by $\sim 0^m.1$. The proper light curves near the primary minimum may be considered to have been also obtained for the first time.

An analysis of the light curves yielded the following information about the star.

The period and epoch were refined; their accuracy was improved by a factor of ~2.

The light curve exhibits no flare activity similar to that detected in BM Ori (with a time scale of ~2 h and with an increase in the flare amplitude to shorter wavelengths), but temporary brightness rises were found in the *U* and *R* bands.

No phase effect was detected, suggesting that the system is not close. This is in agreement with the small relative radii of the stars.

Two light-curve solutions were obtained. In the first solution, we assume that the giant star lies in front of the small star and that the eclipse is partial and take into account orbital ellipticity; however, the photometric elements disagree with those obtained by assuming a total eclipse and a circular orbit [7]. Given that the brightness of star E has not been known previously and, hence, has not been taken into account, the light-curve solution may be considered to have been obtained for the first time. In the second solution, the small star is assumed to lie in front of the giant one. In this case, the radius of the primary star turns out to be a factor of 1.3 larger than that in the first solution. We can thus reconcile the radii of the primary star calculated by two independent methods [13], and these radii correspond to the other parameters of a B0 ZAMS star.

Two arguments force us to accept the hypothesis of a partial eclipse. One of them is the absence of secondary lines in the spectrum (in the case of a total eclipse, secondary lines must also be seen outside eclipse), and the other is an exceedingly small reddening of the star during totality (in the case of a total eclipse, the reddening must be larger).

The entire set of data on V1016 Ori obtained here, by Vitrichenko and Klochkova [13], who analyzed the spectrum, and by Vitrichenko [15], who studied the dust shell around the secondary star, leads us to conclude that the primary and the secondary are B0(1) V and B8(2) V stars, respectively. The primary lies on the ZAMS, while the secondary is on the way from the birth line to the main sequence [4].

ACKNOWLEDGMENTS

We wish to thank V.S. Shevchenko for providing the observational data and for a helpful discussion, the Astronomical Data Center (CDS) for sending us unpublished observations, and V.G. Klochkova for providing high-quality spectrograms of the star. We are also grateful to the referees, V.L. Khokhlova and A.A. Tokovinin, for constructive remarks, which helped improve the article.

REFERENCES

1. E. Lohsen, Inf. Bull. Var. Stars, No. 988 (1975).
2. E. Lohsen, Inf. Bull. Var. Stars, No. 1211 (1976).
3. É. A. Vitrichenko, V. G. Klochkova, and S. I. Plachinda, Pis'ma Astron. Zh. **24**, 352 (1998) [Astron. Lett. **24**, 295 (1998)].
4. É. A. Vitrichenko, Pis'ma Astron. Zh. **25**, 220 (1999) [Astron. Lett. **25**, 179 (1999)].
5. M. G. Petr, V. Coude de Foresto, S. V. W. Beckwith, *et al.*, Astrophys. J. **500**, 825 (1998).
6. M. Bossi, A. Gaspani, M. Scardia, and M. Tadini, Astron. Astrophys. **222**, 117 (1989).
7. M. M. Zakirov, Perem. Zvezdy **21**, 223 (1979).
8. M. Felli, M. Massi, and E. Churchwell, Astron. Astrophys. **217**, 179 (1989).
9. M. Felli, M. Massi, and M. Catarzi, Astron. Astrophys. **248**, 453 (1991).
10. M. Gagne, J.-P. Caillault, and J. R. Stauffer, Astrophys. J. **445**, 280 (1995).
11. S. Yamauchi, K. Koyama, M. Sakano, and K. Okada, Publ. Astron. Soc. Jpn. **48**, 719 (1996).
12. K. Koyama, K. Hamaguchi, S. Ueno, *et al.*, Publ. Astron. Soc. Jpn. **48**, L87 (1996).
13. É. A. Vitrichenko and V. G. Klochkova, Pis'ma Astron. Zh. **26**, 133 (2000) [Astron. Lett. **26**, 104 (2000)].
14. N. I. Bondar' and É. A. Vitrichenko, Preprint No. 1992 (Space Research Institute, Russian Academy of Sciences, Moscow, 1998).
15. É. A. Vitrichenko, Pis'ma Astron. Zh. **24**, 708 (1998) [Astron. Lett. **24**, 611 (1998)].
16. N. I. Bondar' and É. A. Vitrichenko, Astron. Zh. **74**, 701 (1997) [Astron. Rep. **41**, 621 (1997)].
17. N. I. Bondar' and É. A. Vitrichenko, Pis'ma Astron. Zh. **22**, 257 (1996) [Astron. Lett. **22**, 229 (1996)].
18. T. A. Lee, Astrophys. J. **152**, 913 (1968).
19. É. A. Vitrichenko, Pis'ma Astron. Zh. **22**, 587 (1996) [Astron. Lett. **22**, 523 (1996)].
20. N. Z. Ismailov, Pis'ma Astron. Zh. **14**, 327 (1988) [Sov. Astron. Lett. **14**, 138 (1988)].
21. V. Straizis and G. Kuriliene, Astrophys. Space Sci. **80**, 353 (1981).
22. W. F. van Altena, J. T. Lee, J.- F. Lee, *et al.*, Astron. J. **95**, 1744 (1988).
23. M. F. Walker, Inf. Bull. Var. Stars, No. 1080, 1 (1976).
24. M. F. Walker, Inf. Bull. Var. Stars, No. 1148, 1 (1976).
25. D. B. Caton, F. W. Fallon, and R. E. Wilson, Publ. Astron. Soc. Pac. **89**, 530 (1977).
26. O. G. Franz, Inf. Bull. Var. Stars, No. 1274 (1977).
27. J. R. Sowell and D. S. Hall, Inf. Bull. Var. Stars, No. 2076 (1982).

Translated by V. Astakhov

Astronomy Letters, Vol. 26, No. 7, 2000, pp. 460–472. Translated from Pis'ma v Astronomicheskiĭ Zhurnal, Vol. 26, No. 7, 2000, pp. 535–548.

UV Cas: Photometry, Polarization, and Spectrum near Maximum Light

V. T. Doroshenko*, Yu. S. Efimov, and A. É. Rosenbush

Sternberg Astronomical Institute, Universitetskiĭ pr. 13, Moscow, 119899 Russia
Crimean Astrophysical Observatory, p/o Nauchnyĭ, Crimea, 334413 Ukraine
Main Astronomical Observatory, National Academy of Sciences of Ukraine, Goloseevo, Kiev, 252127 Ukraine

Received June 28, 1999; in final form, October 18, 1999

Abstract—The *UBV* observations of UV Cas during 1996–1999 show mostly irregular light variations. The *VB* light variations on time scales from one day to two weeks have a smaller amplitude than those on longer time scales. The amplitude of the *UBV* light variations on time scales from 20 to 200 days reaches $0\overset{m}{.}4$, $0\overset{m}{.}3$, and $0\overset{m}{.}2$, respectively. The colors of UV Cas do not correspond to G5 supergiants, but are more similar to the colors of G0 I stars at substantial *U–B* color excesses. A comparison of the energy distribution for UV Cas, as constructed from the broadband *UBVRI* observations in 1982, with the energy distribution for G0 supergiants reveals enhanced near-infrared and ultraviolet emission, which can be attributed to unusual chemical composition of the star. The polarization of light from UV Cas in quiescence is mainly interstellar in origin, although the presence of weak intrinsic polarization produced by the gas–dust circumstellar medium cannot be ruled out either. The strength of C I lines in the spectrum of UV Cas confirms that it belongs to R CrB stars, as well as the conclusion of Orlov and Rodríguez that carbon is appreciably overabundant. The atmospheric metal underabundance in UV Cas may be larger than has been thought previously. The line broadening is $\sigma = 10.7$ km s^{-1}. The star's effective temperature appears to be higher than 5500 K. The radial velocity of UV Cas measured from metal and carbon lines is -31.17 ± 0.38 km s^{-1}. The Na I D lines have a split profile, with the two absorbing clouds observed toward UV Cas at distances < 1 kpc and 1.5–2.5 kpc from the Sun contributing to its components. © *2000 MAIK "Nauka/Interperiodica".*

Key words: *variable stars; photometric, polarimetric, and spectroscopic observations*

INTRODUCTION

R Coronae Borealis (R CrB) variability with profound nonperiodic fadings has been previously thought to be characteristic of hydrogen-deficient stars. In the last decade, however, variability of this type has been detected in a star with a normal hydrogen abundance (FG Sge) and in a star with a slight hydrogen underabundance (V854 Cen), which can be considered as initial evolutionary phases through the stage of an R CrB variable [1]. Adding new members to the variables of this type may open up a new page in their investigation.

The poorly studied star UV Cas, which belongs to the R CrB type but which ceased to exhibit profound fadings in the early 20th century, is of interest from this point of view. According to Orlov and Rodriguez [2], UV Cas is a G5 Ib supergiant with a large hydrogen underabundance and with a carbon abundance that is two orders of magnitude higher than the normal one. It is located near the Galactic plane at a distance of about 4 kpc in a region of the Galaxy with large interstellar extinction ($A_V \approx 2\overset{m}{.}4$) [3].

The reasons why sharp and dramatic fadings ceased can be sought either in complete or almost complete hydrogen depletion, or in a cessation of pulsations, which regulate the onset and completion of profound fadings and which can affect dust condensation in the immediate vicinity of the star [4–6], or in an insufficient mass-loss rate [7].

Hydrogen-deficient stars are generally believed to be the remnants of red giants that lost their hydrogen envelope during their evolution. Circumstellar dust, which can be detected by an infrared excess and/or by polarization of light, may exist around some stars of this type. Indeed, weak variable polarization was noticed in R CrB at its maximum light [8]. However, as yet there is no clear idea about the formation of dust or about the rate of mass loss in stars of this type, because the infrared excess associated with the dust shell can occasionally be absent [9, 10]. Polarization observations, along with photometric and spectroscopic ones, can therefore provide important information about the circumstellar medium of such stars.

Visual light pulsations in UV Cas were considered by Weiss *et al.* [11], who observed this star during 1991–1993. These authors noted a trend of the order of

* E-mail address for contacts: doroshen@sai.crimea.ua

$0^m.2$ in *V* and photometric variability on a time scale of 40 days with an amplitude of $0^m.04$. Apart from short-term optical pulsations, R CrB stars exhibit infrared variability on time scales of a thousand days or more [4]. Such variability in the visual band can be reflected in light variations in antiphase with infrared variations [7]. A permanent gas–dust shell can bear responsibility for such a behavior [7].

Here, we consider the photometric, polarimetric, and spectroscopic observations of UV Cas performed in the last several years when the star was in its normal, quiescent state.

1. OBSERVATIONS: PHOTOMETRY, POLARIZATION, AND SPECTRA

The photoelectric *UBV* observations of UV Cas were carried out in 1974–1975 and 1996–1999 with the 60-cm telescope at the Crimean Station of the Sternberg Astronomical Institute (SAI). BD+58°2530 with $V = 10^m.10$, $B = 10^m.37$, and $U = 10^m.55$ taken from Nicolet's catalog [12] was a comparison star. BD + 58°2529 and BD + 58°2536 were used as check stars; their magnitudes were also taken from the same catalog [12]. The errors calculated from pulse statistics in the signal integration time corrected for sky background were, on the average, $\sigma_V = 0^m.01$, $\sigma_B = 0^m.01$, and $\sigma_U = 0^m.04$.

In addition, several photometric magnitude estimates were obtained in September–November 1982, while the polarization observations of UV Cas were carried out in November 1982 with the photometer–polarimeter designed by Piirola (Finland), which was mounted at the Cassegrain focus of the 125-cm Crimean Astrophysical Observatory (CrAO) telescope. The observations were performed in the *UBVRI* bands centered at wavelengths of 0.36, 0.44, 0.53, 0.69, and 0.83 μm, respectively, through a 10″ aperture (see [13] for a detailed description of the instrumentation).

The results of our photometric observations are presented in Table 1, where the first column gives evening dates of observations. Polarization data are given in Table 2, where, for completeness, we collected all the published data on polarization of light from this star, together with our observations. Below, we discuss the polarization data in more detail.

Figure 1 shows *UBV* light curves for the period of our observations from 1996 until 1999. We also constructed an overall *V* light curve starting from 1958 (Fig. 2); apart from our observations, we used data from different sources [9–11, 14–18] to construct this curve. The points on the overall light curve between October 13, 1958, and November 10, 1964, were obtained from photographic data of the sky patrol at the Main Astronomical Observatory (National Academy of Sciences of Ukraine) with a two-camera astrograph in the photographic and photovisual bands. Note that the observations by Tempesti [15] and Daube [16] are also photographic, while all the remaining observations are photoelectric. It turned out that the observations by Tempesti [15], on the one hand, and by Fernie *et al.* [14] and Zavatti [17], on the other hand, have eight common dates and correlate well with each other. The coefficient of correlation between m_{pg} and *V* is $r = 0.82$. We were therefore able recalculate the photographic magnitudes from [15] to *V* magnitudes by using the eight common dates of observations. In addition, to standardize the data of Weiss *et al.* [11], we referenced their comparison star SAO 35058 = BD+58°2527 to BD +58°2530, BD +58°2529, and BD+58°2536. The following *UBV* magnitudes were obtained for this star: $V = 9^m.79 \pm 0^m.01$, $B = 10^m.11 \pm 0^m.01$, and $U = 10^m.31 \pm 0^m.01$.

The spectroscopic observations were carried out at the coude focus of the 2.6-m CrAO telescope with a 1024 × 480-pixel AT200 CCD Camera System array. A ≈60 Å wide spectrum near Na I D was taken during two 30-min exposures on October 20, 1998 (JDh = 2451107.24–.27). The spectral resolution was 0.15 Å. The signal-to-noise ratio averaged over the two spectra was S/N ≈ 35. We reduced the spectra by using the SPE software package, which was developed by S.G. Sergeev (CrAO). The wavelength scale was specified by the comparison spectrum of an argon–thorium lamp with a hollow cathode. The accuracy of fitting the dispersion curve by a linear polynomial using nine lines in the comparison spectrum was 0.008 Å. To eliminate water lines from the UV Cas spectrum, we observed the B0.5 IV star 1 Cas. The UV Cas continuum was fitted by a third-degree polynomial. The average spectrum of UV Cas normalized to the continuum is shown in Fig. 3.

The synthetic spectra for a model with $T_{\rm eff} = 5500$ K and $\log g = 0.00$ at the abundances He/H = 0.7 dex and C/H = 0.026 dex retrieved from the International Data Center in Strasbourg [19] were used to identify spectral lines. In the wavelength range 5864–5928 Å, the split Na I D lines are the strongest absorption features in the UV Cas spectrum. Metal (Fe I, V II, Ti II) lines can be noted among the weaker absorption lines. There are many C I absorption lines in the spectrum, with the λλ5864.963, 5870.660, 5875.447+5875.856, 5877.341, and 5912.579 Å features being most prominent. It is hard to tell whether He I λ5876 is certain to be present because of its possible blending with the fairly strong C I λλ5875.447 and 5875.856 absorption lines.

2. DISCUSSION

2.1. Spectrophotometry

According to our spectrograms, the line broadening in UV Cas corrected for the instrumental profile corresponds to a standard deviation of 0.21 Å or 10.7 km s^{-1}. Consequently, the gas motions responsible for the line broadening, be it rotation or turbulent motions of a ther-

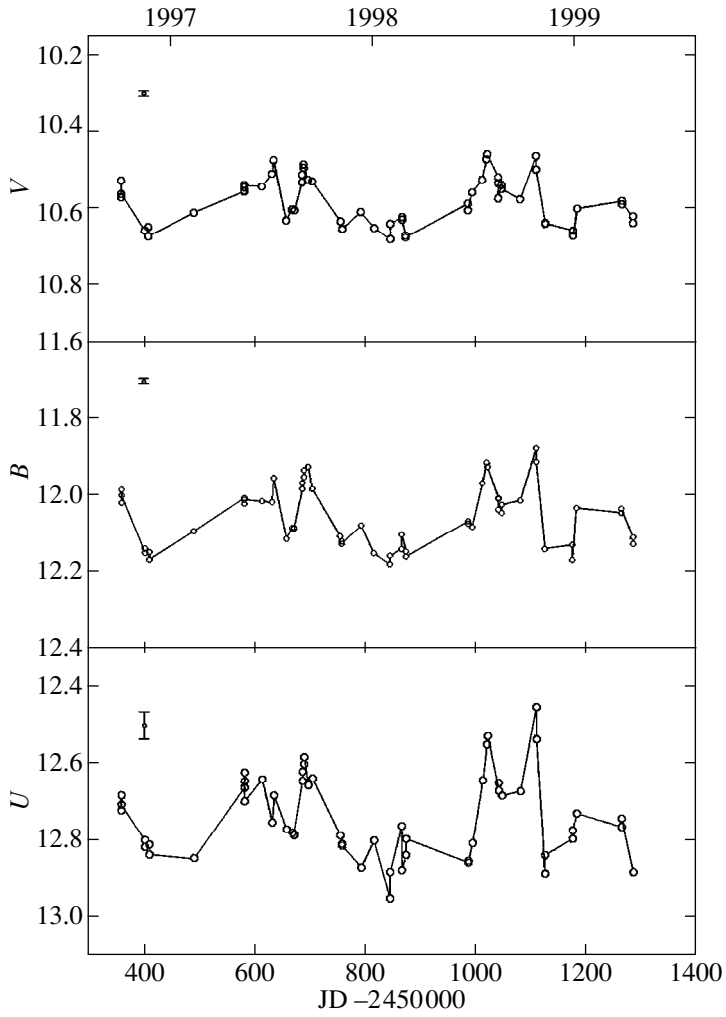

Fig. 1. The *UBV* light curves, as constructed from the 1996–1999 observations

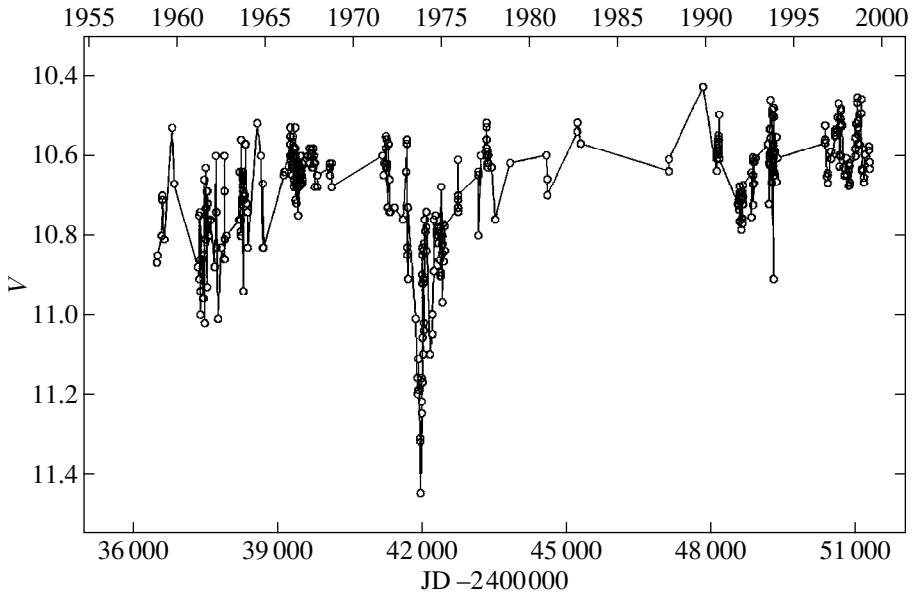

Fig. 2. The overall *V* light curve of UV Cas for a period of 40 years, as constructed from the data of different authors.

Table 1. *UBV* magnitude estimates for UV Cas

Date, yy.mm.dd	JDh (2440000+)	*V*	σ*V*	*B–V*	σ(*B–V*)	*U–V*	σ(*U–B*)
Nov. 25, 1974	2377.3535	10.86	0.03	1.55	0.04	0.54	0.05
Dec. 02, 1974	2384.4243	10.89	0.02	1.53	0.03	0.71	0.05
Dec. 02, 1974	2384.4444	10.90	0.02	1.57	0.03	0.84	0.05
Jan. 13, 1975	2426.3528	10.97	0.01	1.52	0.02	0.73	0.02
Jan. 14, 1975	2427.2729	10.84	0.01	1.52	0.02	0.67	0.02
Feb. 13, 1975	2457.2139	10.87	0.02	1.54	0.02	0.74	0.05
Feb. 23, 1975	2467.2215	10.84	0.02	1.52	0.03	0.55	0.07
Feb. 13, 1975	2467.2361	10.78	0.02	1.56	0.03	0.53	0.06
Sep. 09, 1982[1]	5222.2940	10.54	0.02	1.48	0.02	0.77	0.03
Sep. 13, 1982[2]	5226.5579	10.52	0.02	1.47	0.02	0.78	0.03
Nov. 28, 1982[3]	5302.3383	10.57	0.02	1.47	0.02	0.73	0.03
Oct. 02, 1996	10359.2896	10.57	0.00	1.45	0.01	0.74	0.02
Oct. 02, 1996	10359.3056	10.53	0.00	1.46	0.01	0.74	0.03
Oct. 02, 1996	10359.3118	10.56	0.01	1.44	0.01	0.75	0.03
Nov. 14, 1996	10402.2979	10.66	0.00	1.50	0.01	0.69	0.02
Nov. 14, 1996	10402.3035	10.66	0.00	1.48	0.01	0.72	0.02
Nov. 21, 1996	10409.1743	10.65	0.01	1.50	0.01	0.70	0.02
Nov. 21, 1996	10409.1812	10.67	0.00	1.49	0.01	0.71	0.02
Feb. 11, 1997	10491.1896	10.61	0.01	1.48	0.01	0.81	0.04
Dec. 05, 1997	10581.4736	10.55	0.01	1.45	0.01	0.71	0.04
May 12, 1997	10581.4792	10.54	0.01	1.46	0.01	0.69	0.03
May 13, 1997	10582.4778	10.55	0.00	1.47	0.01	0.66	0.03
May 13, 1997	10582.4847	10.54	0.00	1.47	0.00	0.74	0.02
June 14, 1997	10614.5028	10.54	0.01	1.47	0.01	0.67	0.05
July 01, 1997	10631.5076	10.51	0.01	1.51	0.02	0.78	0.05
July 05, 1997	10635.5035	10.47	0.01	1.48	0.01	0.77	0.04
July 28, 1997	10658.3736	10.63	0.01	1.48	0.01	0.70	0.02
Aug. 07, 1997	10668.4875	10.60	0.00	1.48	0.01	0.73	0.03
Aug. 11, 1997	10672.4285	10.60	0.01	1.48	0.01	0.73	0.02
Aug. 11, 1997	10672.4292	10.60	0.01	1.48	0.01	0.74	0.02
Aug. 26, 1997	10687.4896	10.53	0.00	1.45	0.00	0.70	0.03
Aug. 26, 1997	10687.4965	10.51	0.01	1.45	0.01	0.69	0.03
Aug. 29, 1997	10690.4896	10.49	0.01	1.46	0.01	0.69	0.03
Aug. 29, 1997	10690.4958	10.48	0.01	1.45	0.01	0.69	0.03
Sep. 05, 1997	10697.5785	10.52	0.01	1.40	0.01	0.78	0.03
Sep. 13, 1997	10705.5819	10.53	0.00	1.45	0.01	0.70	0.02
Nov. 03, 1997	10756.2792	10.63	0.00	1.47	0.01	0.72	0.02
Nov. 06, 1997	10759.2785	10.65	0.00	1.47	0.01	0.72	0.02
Nov. 06, 1997	10759.2819	10.65	0.00	1.47	0.01	0.72	0.02
Dec. 10, 1997	10793.2701	10.61	0.01	1.47	0.01	0.84	0.04
Jan. 03, 1998	10817.2882	10.65	0.00	1.50	0.01	0.70	0.02
Feb. 01, 1998	10846.1882	10.68	0.01	1.50	0.01	0.82	0.02
Feb. 01, 1998	10846.1979	10.64	0.01	1.52	0.01	0.78	0.02
Feb. 22, 1998	10867.1972	10.62	0.01	1.52	0.01	0.68	0.04
Feb. 22, 1998	10867.2021	10.63	0.01	1.47	0.02	0.83	0.04
Mar. 01, 1998	10874.2028	10.67	0.02	1.48	0.03	0.76	0.07
Mar. 03, 1998	10874.2076	10.67	0.01	1.49	0.01	0.70	0.04
June 22, 1998	10987.3208	10.59	0.00	1.48	0.01	0.86	0.05

Table 1. (Contd.)

Date, yy.mm.dd	JDh (2440000+)	V	σV	$B–V$	$\sigma(B–V)$	$U–V$	$\sigma(U–B)$
June 22, 1998	10987.3278	10.60	0.01	1.47	0.01	0.84	0.06
June 29, 1998	10994.4910	10.56	0.01	1.52	0.01	0.77	0.02
July 18, 1998	11013.3132	10.52	0.01	1.44	0.01	0.73	0.03
July 25, 1998	11020.5215	10.47	0.01	1.44	0.01	0.67	0.03
July 26, 1998	11021.5257	10.46	0.00	1.46	0.01	0.64	0.04
Aug. 15, 1998	11041.2611	10.52	0.01	1.49	0.02	0.71	0.06
Aug. 15, 1998	11041.2681	10.53	0.00	1.47	0.01	0.69	0.06
Aug. 15, 1998	11041.2708	10.57	0.00	1.46	0.01	0.68	0.02
Aug. 22, 1998	11048.2639	10.54	0.01	1.51	0.02	0.68	0.05
Aug. 22, 1998	11048.2708	10.55	0.00	1.47	0.02	–	–
Sep. 24, 1998	11081.5861	10.58	0.01	1.44	0.01	0.71	0.03
Oct. 23, 1998	11110.1743	10.46	0.01	1.41	0.01	0.62	0.03
Oct. 23, 1998	11110.1819	10.50	0.00	1.41	0.01	0.66	0.02
Nov. 08, 1998	11126.1660	10.64	0.01	1.50	0.01	0.78	0.02
Nov. 08, 1998	11126.1743	10.64	0.01	1.50	0.01	0.74	0.03
Dec. 28, 1998	11176.4688	10.66	0.01	1.47	0.03	0.75	0.10
Dec. 28, 1998	11176.4750	10.67	0.01	1.50	0.02	0.70	0.08
Jan. 05, 1999	11184.2687	10.60	0.01	1.43	0.02	0.74	0.02
Mar. 26, 1999	11264.5528	10.58	0.01	1.46	0.02	0.79	0.05
Mar. 26, 1999	11264.5590	10.59	0.00	1.44	0.01	0.78	0.03
Apr. 16, 1999	11285.5486	10.62	0.01	1.49	0.01	0.83	0.04
Apr. 16, 1999	11285.5507	10.64	0.01	1.49	0.01	0.81	0.03

[1] 82.09.09, $R = 9\overset{m}{.}33 \pm 0\overset{m}{.}01$, $I = 8\overset{m}{.}39 \pm 0\overset{m}{.}02$.

[2] 82.09.13, $R = 9\overset{m}{.}40 \pm 0\overset{m}{.}01$, $I = 8\overset{m}{.}34 \pm 0\overset{m}{.}02$.

[3] 82.11.28, $R = 9\overset{m}{.}45 \pm 0\overset{m}{.}01$, $I = 8\overset{m}{.}41 \pm 0\overset{m}{.}02$.

Table 2. Polarization in UV Cas

Date	JD –2440000	λ, μm	P, %	σ_P, %	$\Theta°$	$\sigma_{\Theta°}$	References
Mar. 10, 1974	2117	0.35–0.70	3.95		58.5		Orlov *et al*. [28]
Oct. 11, 1974	2332	0.35–0.70	3.72		58.5		Orlov *et al*. [28]
Sept. 21, 1975	4238	0.35–0.70	3.71		56.5		Orlov *et al*. [28]
Nov. 28, 1982	5302.34	0.36	2.77	1.12	54.2	11.0	This paper
		0.44	4.17	0.25	55.4	1.7	This paper
		0.53	4.05	0.20	57.3	1.4	This paper
		0.69	3.67	0.05	55.0	0.4	This paper
		0.83	3.23	0.12	56.0	1.1	This paper
Dec. 20, 1984	6055.19	0.44	5	0.6	52		Raveendran *et al*. [26]
		0.55	4.2	0.2	48		Raveendran *et al*. [26]
		0.69	3.9	0.2	48		Raveendran *et al*. [26]
		0.83	3.9	0.2	53		Raveendran *et al*. [26]
Nov. 01, 1989	7832.4	0.55	3.5	0.2	56	1	Rosenbush *et al*. [27]
Nov. 02, 1989	7833.2	0.55	3.7	0.2	58	1	Rosenbush *et al*. [27]

mal nature, have velocities of ~10–11 km s^{-1}. It is unclear how the R CrB supergiants rotate, and rotation in these stars is believed to be of little importance. The intense motions observed in the photospheres of these stars are primarily attributable to macro- and microturbulence. Since our estimate satisfactorily matches the microturbulent velocity of 11 km s^{-1} estimated by Orlov and Rodriguez [2] by analyzing curves of growth for UV Cas, the microturbulent velocity can be assumed to be a crucial velocity that determines the widths of fairly strong absorption lines. Below, we use this estimate to compute a synthetic spectrum.

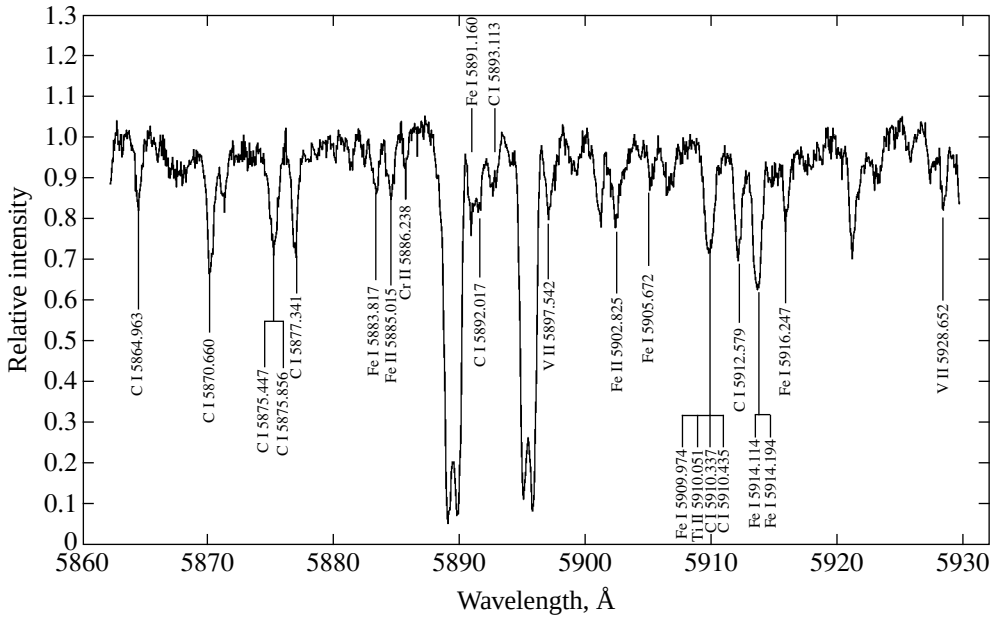

Fig. 3. The spectrum of UV Cas near Na I D with line identification.

The significant strength of C I lines is not typical of G5 Ib supergiants. However, the spectra of R CrB stars are known to be characterized by weak hydrogen lines and strong C I and He I lines. The strength of C I lines in the spectrum of UV Cas confirms that it belongs to R CrB stars and lends support to the conclusion of Orlov and Rodriguez [2] that carbon is overabundant in this star compared not only to normal stars but also to the R CrB star itself. Our line identification is shown in Fig. 3.

Based on C I and metal lines, which are more or less free from blends, we determined the star's radial velocity. These are rather weak lines, with their residual intensities lying in the range 0.69–0.96. The radial velocities estimated from different lines are listed in Table 3; its successive columns give the species and the corresponding laboratory wavelength, the measured wavelength and the star's radial velocity corrected for the Earth's rotation and for the Earth's motion around the Sun. The star's radial velocity, as inferred from metal and C I lines, is, on the average, $V_r = -31.23 \pm 0.69$ and -31.14 ± 0.46 km s^{-1}, respectively. The mean radial velocity of the star (as deduced from all lines in the two spectra) is $V_r = -31.17 \pm 0.38$ km s^{-1}, with the error of a single radial-velocity measurement being $\sigma = 0.8$ km s^{-1}.

Note that we know two radial-velocity estimates for UV Cas [20], which were obtained on September 30, 1941, (–31.4 km s^{-1}) and December 5, 1941, (–23.1 km s^{-1}) from low-dispersion spectra. Radial-velocity variability can hardly be inferred from a comparison of these data with our data.

We also measured the radial velocity of the comparison star 1 Cas by using the He I λ5876 line. It was found to be –9 km s^{-1}, in close agreement with the cataloged value [21]. Apart from the broad He I λ5876 absorption line, which clearly belongs to the star, the spectrum of 1 Cas exhibits two narrow Na I D absorption lines of interstellar origin. These lines closely coincide in position with the long-wavelength components of the Na I D lines in the spectrum of UV Cas, which is located in the plane of the sky within less than 1° of the comparison star 1 Cas (see Table 3). The radial velocity measured from the interstellar Na I D lines in 1 Cas is -15.0 ± 0.5 km s^{-1}. The long-wavelength absorption peaks of the Na I D lines in UV Cas correspond to a radial velocity of -15.6 ± 0.2 km s^{-1}. Thus, the long-wavelength components of the Na I D lines in the UV Cas spectrum can be assumed to be affected by the interstellar medium.

As for the short-wavelength components of the Na I D lines in UV Cas, they appear to be also affected by the interstellar medium. Indeed, 1 Cas, which is 350 pc away, has only one component in the interstellar Na I D lines, whose radial velocity (–15 km s^{-1}) and intensity (237 mA) are in satisfactory agreement with Münch's estimates [22]. On the other hand, the other two stars from [22], namely, HD 216411 and HD 216927, which are further away (their distance moduli are 11.8 and 13.3, respectively, while the distance modulus of UV Cas is 11.3–12.8) and lie in the plane of the sky within slightly more than 1° of UV Cas, exhibit at least two peaks in the interstellar lines at radial velocities of –15 and –50 km s^{-1}; there may also be a third peak at $V_r = -60$ km s^{-1}. The equivalent widths of these interstellar lines are larger than those in 1 Cas, suggesting the large-scale structure of the interstellar absorbing matter toward UV Cas associated with the spiral pattern of the Galaxy [22]. Indeed, at least two large absorbing com-

Table 3. Radial-velocity estimates for UV Cas

Species	λ_{lab}	UV Cas, λ_{obs}		UV Cas, V_r, km s^{-1}	
		spectrum 1	spectrum 2	spectrum 1	spectrum 2
C I	5864.963	5867.449	5864.444	–29.40	–29.67
C I	5864.963	5864.449	5864.444	–29.40	–29.67
C I	5870.660	5870.147	5870.085	–29.32	–32.52
C I	5870.660	5870.128	5870.079	–30.27	–32.85
C I	5877.342	5876.842	5876.818	–29.63	–29.89
Fe I	5883.817	5883.287	5883.294	–30.13	–29.81
C I	5893.113	5892.544	5892.565	–32.08	–31.02
V II	5897.542	5896.930	5896.956	–34.22	–32.95
C I	5912.579	5911.960	5911.981	–34.51	–33.48
C I	5912.579	5912.010	5911.981	–31.96	–33.51
Fe I	5916.247	5915.716	5915.749	–30.03	–28.39
V II	5928.862	5928.282	5928.295	–32.47	–31.84
		1 Cas		1 Cas	
		λ_{obs}		V_r, km s^{-1}	
Na I D_1	5889.951	5889.726		–14.46	
Na I D_2	5895.924	5895.678		–15.51	
He I	5875.690	5875.577		–9.02	

plexes were detected in the direction with Galactic coordinates $l = 110°$ and $b = -0.°4$: one at a distance of less than 1 kpc and the other at a distance of 1.5–2.5 kpc [23]. The radial velocity determined from the short-wavelength absorption component of the Na I D lines in UV Cas is $V_r = -51.6 \pm 0.4$ km s^{-1}, a value that is very close to the radial velocity of the second components of the interstellar Na I D lines in the neighboring stars mentioned above. Consequently, it may well be that the second peak of the Na I D absorption lines in UV Cas is also significantly affected by interstellar matter.

The stellar component of the Na I D lines for G stars is very intense. We verified this by constructing synthetic spectra in the wavelength range 5860–5930 Å. We used the SYNTH code [24] to compute the synthetic spectra. Model atmospheres were computed by using Kurucz's ATLAS9 program [25]. The half-width of the instrumental profile was taken to be 0.18 Å. In addition, the spectral lines were broadened by rotation ($v \sin i$ = 5 km s^{-1}) and by microturbulence with two values: 2 and 10 km s^{-1}. The macroturbulent velocity was assumed to be 3 km s^{-1}. We considered LTE models with T_{eff} = 5000, 5500, 5750, 6000 K and log$g$ = 0.0, 1.0 for solar metallicity and for a metal underabundance of –0.5 dex. In all cases, we took a hydrogen underabundance [log(H) = 0.59], a helium overabundance [$(\log(N(\mathrm{He})/N(Z)) = -0.2$], and a carbon abundance that was a factor of 100 higher than the solar value, as derived by Orlov and Rodriguez [2]. Our objective was not to study the chemical composition of UV Cas but the desire to understand what intensity the stellar Na I D lines could have under conditions close to those in a G5 Ib star for unusual chemical composition. The stellar Na I D lines are very intense in all the synthetic spectra we considered. The LTE conditions for their formation are most likely satisfied. The Na I D line intensity depends only slightly on small variations in the abundances of the iron-peak elements (from Ca to Ni). However, models with a metal underabundance larger than –0.5 dex are in better agreement with the observed intensity of metal lines in the UV Cas spectrum. Models with T_{eff} = 5500 K and log$g$ = 1.0 are in better agreement with the observed spectrum than models with a lower effective temperature. The carbon abundance may exceed the solar value by more than a factor of 100.

Thus, the profiles of the stellar Na I D lines in UV Cas are difficult to judge, because the interstellar lines are superimposed on them.

2.2. Photometry

The star was mainly in quiescence over more than forty years of observations (see Fig. 2), with its brightness fluctuating about $V \approx 10.^m7$–$10.^m6$. During this period, the mean V brightness gradually increased by $\approx 0.^m15$–$0.^m10$. Only in late 1973 were two successive, more significant fadings by $0.^m89$ and $0.^m54$, when measured from the nearest level of maximum V light, observed. These fadings lasted about 420 and 180 days, respectively. In the remaining time, erratic variability can be noted.

During the 1996–1999 observations (Fig. 1), the light variations exhibited two broad waves in all three bands, each with a duration of ~400 days. A periodicity of the variations is difficult to judge from these two waves. Our search for periodic or cyclic light fluctuations on time scales < 400 days by various methods revealed a distinct frequency of light variations at ν = 0.03628 cycles day^{-1} during our observations, which corresponds to 27.56 days. However, this value is very close to the sidereal month. It should be noted that there is no such frequency in the spectral window. Nevertheless, a statistically significant inference requires longer observations.

We analyzed the variability amplitudes for the 1996–1999 observations. To this end, we considered all possible pairs of observations at times t_i and t_j, calculated the magnitude differences (amplitudes) between all pairs of observations [$\Delta m = |m(t_i) - m(t_j)|$], and selected only significant amplitudes, i.e., those exceeding the observational errors by a factor of 3, from them. In Fig. 4, these differences are plotted against Δt. It can be seen from the figure that the variability amplitude in V and B is less than $0.^m1$ on time scales from one day to two weeks. On longer time scales, from 20 to 200 days, the variability amplitude generally increases, reaching

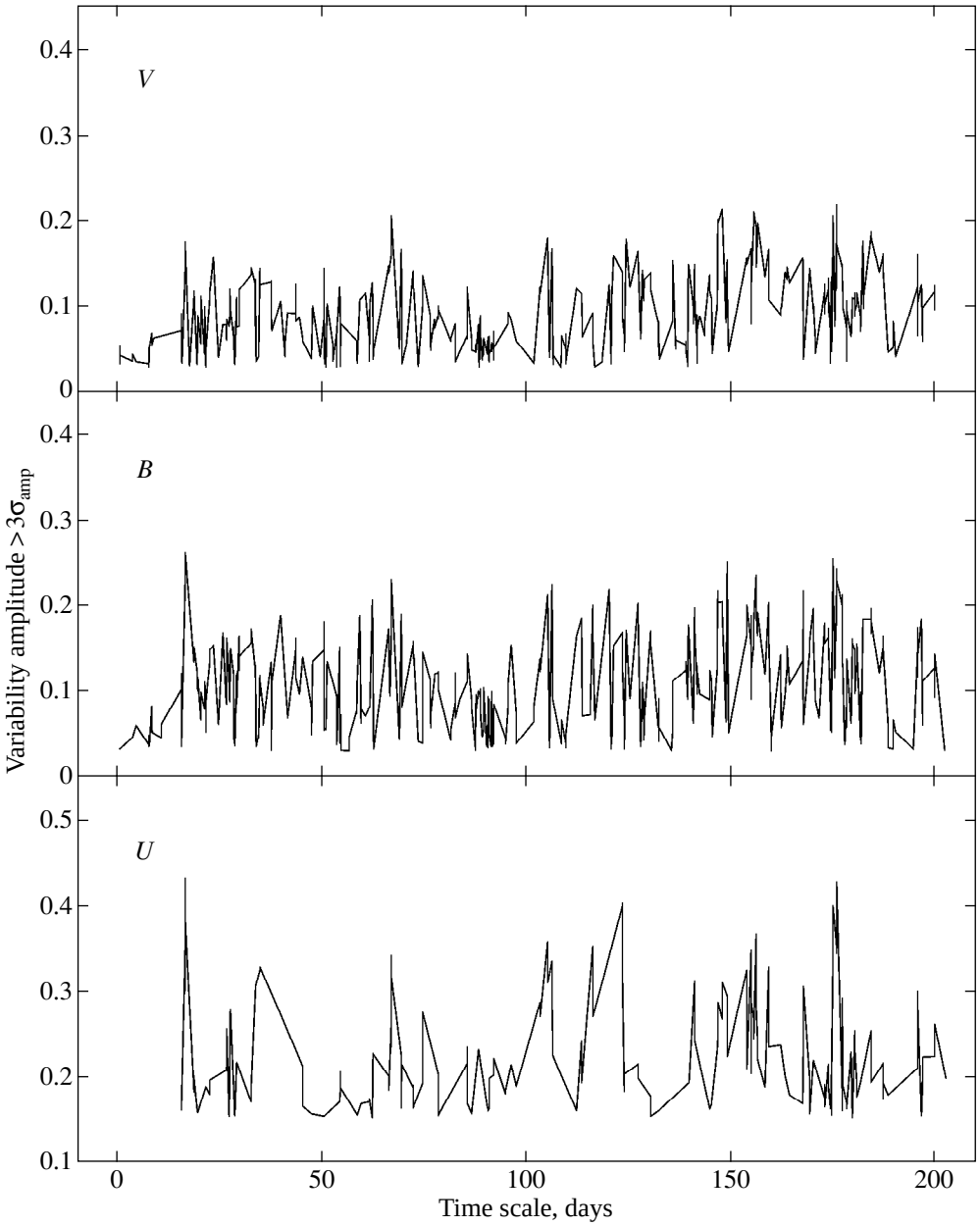

Fig. 4. Variability amplitude exceeding $3\sigma_{amp}$ versus time scale.

$0^m.4$, $0^m.3$, and $0^m.2$ in *UBV*, respectively; i.e., the variability amplitude in *U* is slightly larger.

Our *UBV* observations revealed no evidence of correlation between the light and color variations. However, the multicolor broad-band observations cover only intervals near maximum light. There are no multicolor observations during more significant fadings. We may therefore only note that there is no correlation between light and color in the star's quiescent state near maximum light at light fluctuations of $\Delta V \approx 0^m.2$.

2.3. Polarization

The observed polarization is known to be a superposition of intrinsic (stellar or circumstellar) and interstellar polarizations. Intrinsic polarization can be detected either by variability of the parameters of the observed polarization with time or by deviations of its wavelength dependence from the typical wavelength dependence for the interstellar medium.

Figure 5 compares variations in the brightness and in the polarization of light from UV Cas measured in different years. We see that our polarization measurements in 1982, along with the observations by Raveendran *et al.* [26] and Rosenbush and Rosenbush [27], refer to the star's quiescent state. Only the first polarization estimate for UV Cas in March 1974 [28] refers to a period when the star was recovering from a shallow minimum. The second measurement (in October 1974) was made when the star's brightness was still below its

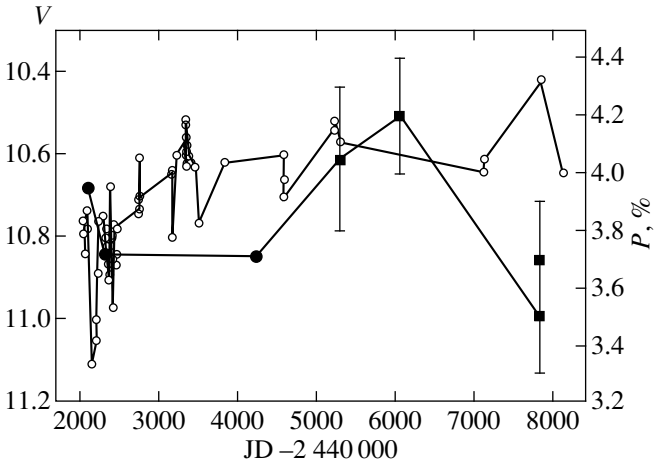

Fig. 5. *V* light and polarization [*P*(%)] variations in UV Cas. The filled circles and filled squares correspond to the degrees of polarization in white light and in *V*, respectively. The light variations are indicated by open circles.

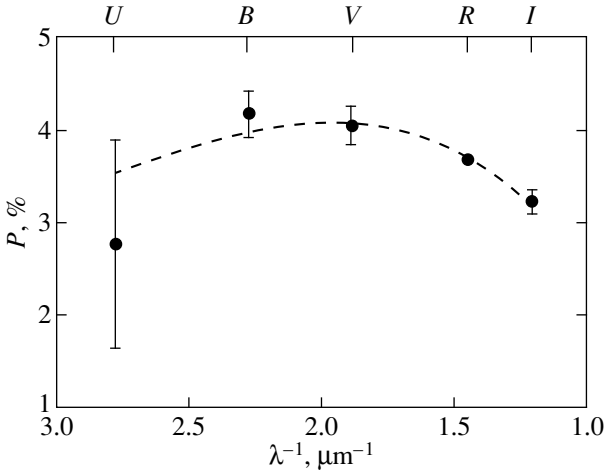

Fig. 6. The wavelength dependence of polarization, as derived from our 1982 observations (filled circles). The dashed line indicates the wavelength dependence of interstellar polarization calculated by using Serkowski's formula [30].

mean level, and the third measurement (in September 1976) was made when the star's brightness was almost normal.

As we see from Table 2, the orientation of the polarization plane is the same in all bands, within the limits of probable observational errors. The white-light observations by Orlov and Rodriguez revealed a fairly large polarization. Our observations in 1982 yielded a higher degree of polarization in the star than did the observations by Orlov and Rodriguez but a similar polarization angle. It could thus be concluded that the polarization in UV Cas is variable. However, this conclusion is wrong, because the observed polarization during white-light observations decreases due to the contribution from spectral regions with a lower polarization. Indeed, the polarization in white light can be estimated from the photometric and polarization observations of this star on November 28, 1982. A comparison of this estimate (P = 3.46%) with the observations by Orlov and Rodriguez [28] ($P \approx 3.7\%$) suggests that the difference between the degrees of polarization in 1977 and 1982 is attributable to the difference in the methods of its measurement. Nevertheless, an examination of the data in Table 2 and Fig. 5 shows that the degree of polarization in *V* in 1982–1984 (≈4.12%) is, on the average, higher than that in 1989 (3.6%), although this difference is only slightly outside the error limits. Note also the difference in the degrees of polarization in *I* between the observations by Raveendran *et al.* [26] and our measurements in 1982. All of these facts suggest that there may be a modest intrinsic polarization at maximum light of the star.

2.3.1. Interstellar polarization

The wavelength dependence of polarization, as deduced from the five-color observations in 1982, is indicated in Fig. 6 by filled circles. We see that the degree of polarization in UV Cas is at a maximum in the blue–yellow spectral region and rapidly drops at shorter and longer wavelengths. Since the star is faint in the ultraviolet, the accuracy of measuring the degree of polarization in *U* is low. In general, however, the wavelength dependence of polarization corresponds to that typical of interstellar polarization.

The position angle of the observed polarization falls into the region of orientations of the polarization vectors for stars in the immediate vicinity of UV Cas within about one degree of it. Unfortunately, few (3–5) distant stars were measured in this region. The orientation of the interstellar-polarization plane for UV Cas cannot be determined more accurately from the available data. Since the observed angle of the polarization plane is essentially independent of wavelength and since its differences between the data of different observers are small, we may assume with a fair degree of confidence that the observed orientation of the polarization plane coincides with the orientation of the interstellar polarization near UV Cas.

The star's position in a region with large interstellar extinction, the high degree of observed polarization in the star's quiescent state and the similarity of its wavelength dependence to that typical of interstellar polarization, the fact that the polarization plane of UV Cas is close to the orientation of the polarization vectors for field stars, and the lack of wavelength dependence of the polarization angle all suggest that the observed polarization in UV Cas is mainly interstellar in origin.

On the one hand, the statistical correlation between total-to-selective absorption ratio R and Galactic longitude l_{II}[$R = 3.08 + 0.17\sin(l_{II} + 175)$] and the statistical relation between R and λ_{max}[$R = 5.65\lambda_{max}$] [29] yield estimates of R = 2.92 and λ_{max} = 0.516 μm.

On the other hand, Serkowski's formula for interstellar polarization [30] can be used to refine the parameters of its wavelength dependence P_{max} and λ_{max}:

$$P_\lambda = P_{max}\exp[-1.15\ln^2(\lambda_{max}/\lambda)], \quad (1)$$

where P_λ is the degree of polarization at wavelength λ, P_{max} is the maximum degree of polarization, and λ_{max} is the wavelength of the polarization maximum.

The dashed line in Fig. 6 indicates Serkowski's wavelength dependence of polarization with the least-squares-fitted parameters $P_{max} = 4.08 \pm 0.30\%$ and $\lambda_{max} = 0.513 \pm 0.009$ μm. The parameter λ_{max} agrees with the value previously obtained from the statistical correlations and with $\lambda_{max} = 0.522$ μm typical of this Galactic region [29].

As we see from the figure, the observed wavelength dependence of the polarization in UV Cas can be satisfactorily described by the curve typical of interstellar polarization.

The multicolor *B*, *V*, *R*, *I* polarization observations by Raveendran *et al.* [26] also reveal an increase in the degree of polarization at shorter wavelengths from 4% in *V*, *R*, *I* to 5% in *B* for small variations in the polarization angle between 48° and 53°. However, the lack of *U* observations makes the data of Raveendran *et al.* [26] less suitable for analysis of the interstellar polarization. In general, however, our estimates for the degree of polarization and for the position angle of the polarization plane are in satisfactory agreement with the estimates of Raveendran *et al.* [26], within the limits of observational errors in BVRI. The similarity between our data and those of Orlov and Rogriguez [28] was pointed out above.

2.3.2. Intrinsic polarization in UV Cas

The difference between a theoretical curve for the interstellar polarization and the 1982 observations can give an estimate of the intrinsic polarization in the star. It was found to be, on the average, 0.08 ± 0.16 in *BVRI* with a steep rise in the ultraviolet, 0.77 ± 1.12. The most likely mechanism for the emergence of intrinsic polarization with a steep rise at short wavelengths is the Rayleigh scattering of starlight by small circumstellar dust grains, which varies as the fourth power of frequency. Given the measurement errors and the crudeness of the model, this result is consistent with the assumption that the increase in the degree of intrinsic polarization in the ultraviolet can actually be caused by the scattering of starlight by small dust grains in a stationary circumstellar envelope around UV Cas. It is hard to be more specific. However, for the differences in the degrees of polarization in UV Cas in *V* between 1982–1984 and 1989 noted above, we cannot rule out the possibility that there is weak (fractions of a percent) intrinsic polarization, which points to the existence of a circumstellar gas–dust envelope.

2.4. Estimating the Absorption, the Two-Color Diagram, and the Spectral Energy Distribution

Since UV Cas is a supergiant, lies far from the Sun, and is located in a region with strong interstellar absorption, it is difficult to determine its color excess $E(B–V)$. The above interstellar-polarization parameters can be used to estimate $E(B–V)$. It can be derived from a statistical relationship between the degree of interstellar polarization P_{max} and the color excess for stars near the Galactic plane [31]: $P_{max} = 5E(B–V)$. A color excess $E(B–V) \approx 0^m.82$ corresponds to the degree of polarization $P_{max} = 4.08\%$ deduced above for UV Cas. This value is slightly higher than Rosenbush's estimate [32], $E(B–V) = 0^m.66$, but matches the estimate from the General Catalog of Variable Stars [33] and is similar to Pugach's estimate $E(B–V) = 0^m.86$ [5], who used data on extinction in the Galaxy toward UV Cas and assumed the mean absolute magnitude for R CrB variables to be $M_V = -4^m.5$. Our estimates are not associated with any assumptions of a particular absolute magnitude for the star and are valid as much as the statistical relationships from [29] and [31] are valid. According to [31], the above statistical relationship holds good near the Galactic plane. We therefore assume our estimates to be just as accurate as the other ones and use below the mean of $E(B–V)$ estimated by Pugach [5], Rosenbush [32], and by us, $E(B–V) = 0^m.78$. For $R = 2.9$, which was determined above, the total absorption is then $A_V \approx 2^m.26$.

The color indices averaged over $\Delta V = 0^m.05$ intervals starting from $V = 10^m.43$ are shown in a two-color $(U–B)$–$(B–V)$ diagram (Fig. 7), and the numbers near filled circles correspond to the mean observed *V* magnitude. The colors of UV Cas were freed from interstellar absorption, $A_V = 2^m.26$. We see from Fig. 7 that the $U–B$ and $B–V$ colors bear no resemblance to the colors for a supergiant of spectral type G5 Ib, which was determined by Orlov and Rodriguez [2], even remotely. They are more likely similar to the colors of G5 V–G8 V stars at small color excesses or to those of G0 I stars at considerable $U–B$ excesses. Previously, having compared synthetic and observed spectra near the Na I D lines, we found the star's effective temperature to be ≥5500 K. Such a temperature better corresponds to a star of a spectral type earlier than G5 I. The positions of the color indices above the line for G0 supergiants can be explained by unusual chemical composition and primarily by a hydrogen underabundance. If we consider relative variations in the colors, then, although they do not correlate appreciably with brightness, we nevertheless see that the color indices slightly increase as the star dims from $V = 10^m.5$ to $V = 10^m.85$. At magnitudes

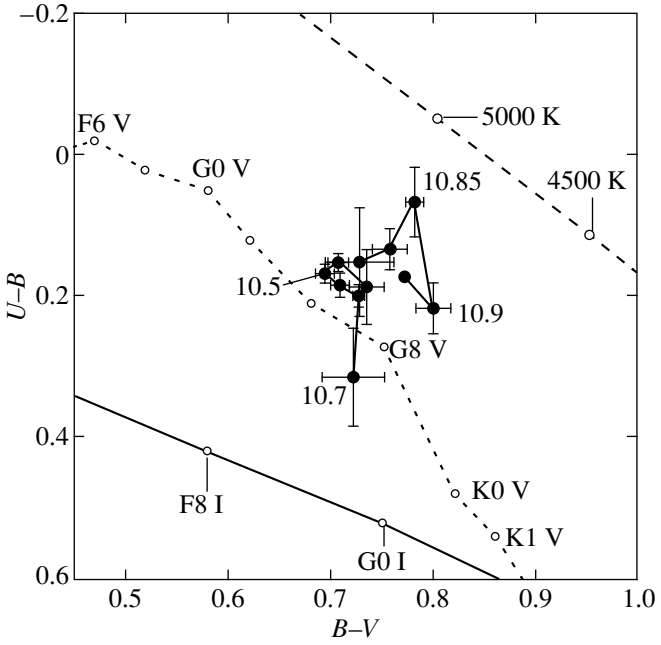

Fig. 7. A two-color (*U–B*)–(*B–V*) diagram. The filled circles represent the color indices of UV Cas averaged over $\Delta V = 0^m.05$ intervals starting from $V = 10^m.43$. The numbers near points denote the mean *V* magnitude. The colors were corrected for interstellar reddening with $A_V = 2^m.26$. The line with long dashes indicates the color variations for a black body. The line with short dashes represents the main sequence with an indication of the stellar spectral type. The solid line indicates the sequence of supergiants.

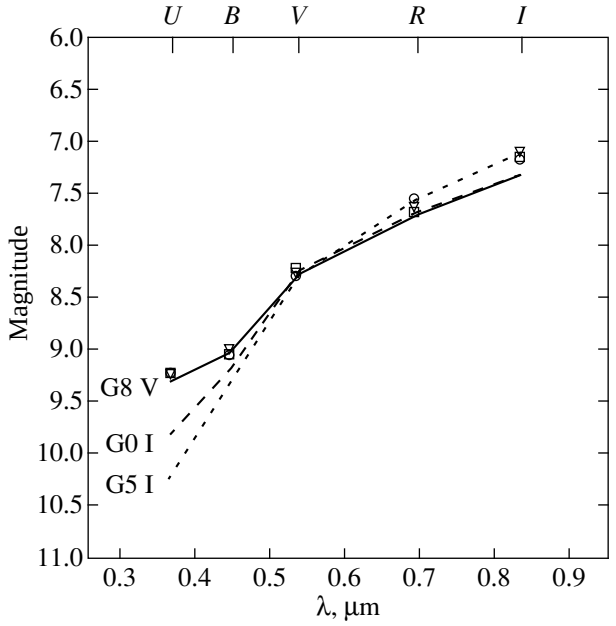

Fig. 8. Comparison of the energy distribution in UV Cas, as inferred from the *UBVRI* observations in 1982, with the energy distribution in supergiants and normal stars. The open circles, triangles, and squares represent the September 9, September 13, and November 28, 1982 observations, respectively.

fainter than $V = 10^m.7$, the *B–V* color indices are appreciably larger than those for $V \le 10^m.7$. This suggests that, for a fading by $0^m.4$ in *V*, the fading in *B* is larger, i.e., the star "reddens" even in a state close to maximum light. The permanent circumstellar envelope may manifest itself in this way.

The *UBVRI* observations in 1982 allow the energy distribution in UV Cas corrected for interstellar absorption to be compared with the energy distribution in supergiants or normal stars (Fig. 8). Among the supergiants, a G0 I star provides the best fit to the observed energy distribution; in this case, however, enhanced radiation in *U* and *I* shows up. If a comparison is made with normal stars, then a G8 V star provides the best fit, but the excess in *I* still remains. Consequently, although the star was at maximum light in 1982, there is enhanced near-infrared and ultraviolet radiation, which is apparently attributable to photospheric peculiarities at unusual chemical composition of the star.

2.5. On the Evolutionary Status of UV Cas

What can be the evolutionary status of UV Cas among the R CrB stars? We may propose, for example, the following sequence: FG Sge, RY Sgr, R CrB, UV Cas, and XX Cam. In fact, minimum visual light or R CrB variability result from the formation of a dust envelope, which is inner relative to the permanent envelope [7]. Stellar pulsations create conditions for dust condensation at distances of ten stellar radii or less [6]. In the case of regular pulsations, as in RY Sgr and FG Sge, minimum light is reached at pulsation minimum [34–36]. Multiperiodicity of pulsations can lead to a less significant controlling role of pulsations, when there will be no clear correlation between the onset of minimum and the pulsation phase [5]. The minimum can have a prolonged phase. R CrB serves as an example of such a situation. If there is no regularity in pulsations and if their amplitude is small, there can be no R CrB minima at all. UV Cas, whose pulsations, if present, have very small amplitudes ($\approx 0^m.04$) [11], can serve as an example of this situation. The sequence FG Sge, RY Sgr, R CrB, UV Cas is completed with XX Cam, which possesses no infrared excess, exhibits no R CrB minima, and shows no regular variability [11]. Next, we can place cool, hydrogen-poor carbon stars after XX Cam.

3. CONCLUSION

The overall light curve exhibits a small trend of the mean brightness in quiescence, $\Delta V \approx 0^m.15$–$0^m.10$ in forty years. The *UBV* observations of UV Cas in 1996–1999 have revealed mostly irregular light variations at that time. The presence of a distinct frequency (ν = 0.0363 cycle per day) in the light variations needs a fur-

ther confirmation using more extensive observational data. The *V, B* light variations on time scales from one day to two weeks have a smaller amplitude than those on longer time scales. The variability amplitude on time scales from 20 to 200 days in *UBV* reaches $0^m.4$, $0^m.3$, and $0^m.2$, respectively.

The positions of the color indices in a two-color (*U–B*)–(*B–V)* diagram in quiescence do not correspond to the spectral classification G5 Ib but correspond more closely to G0 I at a considerable *U–B* color excess. The *U–B* color excess can most likely be explained by unusual chemical composition and primarily by a hydrogen underabundance. It follows from an analysis of the two-color diagram that the star's effective temperature appears to be higher than that of G5 I stars. This is also confirmed by an analysis of spectroscopic data, which suggest $T_{\rm eff} \geq 5500$ K. The color indices of UV Cas corrected for interstellar absorption ($A_V = 2^m.26$) slightly increase as the brightness declines from $V = 10^m.5$ to $V = 10^m.7$; at magnitudes fainter than $V = 10^m.7$, the *B–V* color indices are appreciably larger than those for $V \leq 10^m.5$. This may be considered as evidence for the presence of a permanent circumstellar envelope.

A comparison of the energy distribution in UV Cas, as inferred from the broadband *UBVRI* observations in 1982, with the energy distribution in supergiants reveals enhanced near-infrared and ultraviolet radiation, which may also be associated with unusual chemical composition of the star.

The polarization of light from UV Cas in quiescence is mainly interstellar in origin, although the possibility that there is weak intrinsic polarization produced by the gas–dust circumstellar medium cannot be ruled out either.

The spectrum of UV Cas exhibits many C I lines. The strength of C I lines in the spectrum of UV Cas confirms that it belongs to R CrB stars and the conclusion of Orlov and Rodriguez [2] that carbon is overabundant in this star compared not only to normal stars but also to the star R CrB itself. The atmospheric metal underabundance in UV Cas may be larger than has been thought previously. The line broadening determined from the profiles of single lines in UV Cas corresponds to the standard deviation $\sigma = 10.7$ km s^{-1}, in satisfactory agreement with the microturbulence estimate (11 km s^{-1}) from [2]. The radial velocity of UV Cas measured on October 20, 1998, by using metal and C I lines is -31.17 ± 0.38 km s^{-1}. The Na I D lines have a split profile with the two absorbing clouds observed toward UV Cas at distances < 1 kpc and 1.5–2.5 kpc from the Sun contributing to its components.

ACKNOWLEDGMENTS

We wish to thank the administration and staff of the Crimean Astrophysical Observatory, T.M. Rachkovskaya, S.I. Rostopchin, and N.S. Polosukhina, for help and the opportunity to carry out observations with the 2.6-m telescope. We also wish to thank S.I. Plachinda and O.V. Kozlova for help in retrieving models from the Strasbourg Data Center and T.A. Ryabchikova for help in computing synthetic spectra. The spectroscopic observations described here became possible owing to grants nos. R2Q000 and U1C000 from the International Science Foundation and grant no. A05067 C&EE from the European Southern Observatory.

REFERENCES

1. J. Jurcsik, Acta Astron. **46**, 325 (1996).
2. M. Ya. Orlov and M. G. Rodríguez, Pis'ma Astron. Zh. **7**, 228 (1981).
3. B. E. Zhilyaev, M. Ya. Orlov, A. F. Pugach, *et al.*, *R Coronae Borealis Stars* (Naukova Dumka, Kiev, 1978), p. 10.
4. M. W. Feast, Astron. Soc. Pacif. Conf. Ser. **11**, 538 (1990).
5. A. F. Pugach, Inform. Bull. Var. Stars, No. 1277, 1 (1977).
6. P. Woitke, A. Goeres, and E. Sedlmayr, Astron. Astrophys. **313**, 217 (1996).
7. A. É. Rosenbush, Kinemat. Fiz. Nebesn. Tel **14**, 342 (1998).
8. G. C. Clayton, B. A. Whitney, M. R. Meade, *et al.*, Publ. Astron. Soc. Pacif. **107**, 416 (1995).
9. V. I. Shenavrin, Astron. Zh. **56**, 1228 (1979).
10. V. I. Shenavrin, Perem. Zvezdy **21**, 315 (1980).
11. A. Weiss, R. Fried, and E. C. Olson, Astron. Astrophys., Suppl. Ser. **116**, 31 (1996).
12. B. Nicolet, Astron. Astrophys., Suppl. Ser. **34**, 1 (1978).
13. V. Piirola, *Polarized Radiation of Circumstellar Origin*, Ed. by G. V. Coyne, A. M. Magalhaes, A. F. J. Moffat, *et al.* (Vatican Observatory, Vatican City State, 1988), p. 735.
14. J. D. Fernie, V. Sherwood, and D. L. Du Puy, Astrophys. J. **172**, 383 (1972).
15. P. Tempesti, Inform. Bull. Var. Stars, No. 1036 (1975).
16. I. Daube, Astron. Tsirk., No. 813, 6 (1974).
17. F. Zavatti, Inform. Bull. Var. Stars, No. 1027, 1 (1975).
18. A. É. Rosenbush, Perem. Zvezdy **23**, 255 (1994).
19. N. E. Piskunov, F. Kupka, T. A. Ryabchikova, *et al.*, Astron. Astrophys., Suppl. Ser. **112**, 525 (1995).
20. H. A. Abt, Astrophys. J., Suppl. Ser. **26**, 365 (1973).
21. D. Hoffleit, *The Bright Star Catalogue* (Yale University Observatory, New Haven, 1982).
22. G. Münch, Astrophys. J. **125**, 42 (1957).
23. Th. Neckel and G. Klare, Astron. Astrophys., Suppl. Ser. **42**, 251 (1980).

24. N. E. Piskunov, *Stellar Magnetism*, Ed. by Yu. V. Glagolevskij and I. I. Romanyuk (Nauka, St. Petersburg, 1992), p. 92.
25. R. L. Kurucz, Model Atmosphere Program ATLAS 9, Published on CDROM13 (1993).
26. A. V. Raveendran, N. K. Rao, *et al.*, *Proc. 8th Colloq. IAU Astrophys. Sp. Library*, Ed. by K. Hunger, D. Schönberner, and N. K. Rao (Dordrecht, 1986), Vol. 128, p. 167.
27. A. É. Rosenbush and V. K. Rosenbush, Inform. Bull. Var. Stars, No. 3439, 1 (1990).
28. M. Ya. Orlov and M. G. Rodríguez, Astron. Tsirk., No. 969, 3 (1977).
29. D. S. Whittet, Mon. Not. R. Astron. Soc. **180**, 29 (1977).
30. K. Serkowski, D. S. Mathewson, and V. L. Ford, Astrophys. J. **196**, 261 (1975).
31. I. McLean and D. Clarke, Mon. Not. R. Astron. Soc. **186**, 245 (1979).
32. A. É. Rosenbush, Astrometr. Astrofiz. **44**, 13 (1981).
33. P. N. Kholopov, *General Catalog of Variable Stars* (1985), Vol. 1.
34. V. P. Arkhipova, Pis'ma Astron. Zh. **22**, 828 (1996).
35. J. W. Menzies and M. W. Feast, Mon. Not. R. Astron. Soc. **285**, 358 (1997).
35. M. W. Feast, Astron. Soc. Pacif. Conf. Ser. **96**, 3 (1996).

Translated by V. Astakhov

Astronomy Letters, Vol. 26, No. 7, 2000, pp. 473–483. Translated from Pis'ma v Astronomicheskiĭ Zhurnal, Vol. 26, No. 7, 2000, pp. 549–560.

The Composition of Very Fine Dust in the Dust Shell of Comet Halley

E. N. Evlanov, O. F. Prilutskiĭ, B. V. Zubkov*, and M. I. Voĭskovskiĭ

Space Research Institute, Russian Academy of Sciences, ul. Profsoyuznaya 84/32, Moscow, 117810 Russia

Received July 13, 1999; in final form, November 12, 1999

Abstract—An analysis of the spectra from the PUMA dust-impact mass spectrometers onboard the Vega-1 and Vega-2 spacecraft shows that a large number of the observed, unidentified small-amplitude peaks are produced by impacts of very-low-mass (from 10^{-17} to 10^{-20} g) particles. The mass flux of very fine particles accounts for a few percent of the total dust mass flux from comet Halley. The elemental composition of the finest cometary particles is identical to the composition of large particles (10^{-12}–10^{-16} g), in agreement with present views about the nucleus of comet Halley as an aggregate of interstellar dust. *© 2000 MAIK "Nauka/Interperiodica".*

Key words: *Comet Halley, dust-impact mass spectrometer PUMA, finest particles*

According to present cosmogonical views, the cometary nuclei are closest to the primordial matter of the protoplanetary nebula, and their composition and structure have undergone no significant changes since their formation. The cometary nuclei are assumed to be conglomerates of interstellar dust grains held together by frozen volatile components (mainly by water ice). The heating of a cometary nucleus in the solar neighborhood is accompanied by the evaporation of volatile components and by the release of dust grains.

These views about the nature of comets were confirmed by in-situ measurements of the characteristics of the gas and dust components of the comet Halley's shell during the Vega and Giotto flybys at a distance of less than ten thousand kilometers from its nucleus. Of particular importance were in-situ measurements of the cometary-dust composition.

Here, we make an attempt to determine the elemental composition of the finest particles of the comet Halley's dust shell by using a new method of processing quasi-noise spectra from the PUMA dust-impact mass spectrometers onboard the Vega-1 and Vega-2 spacecraft [1].

Kissel *et al.* [1] identified the spectra of particles with masses exceeding 10^{-16} g. In addition, Sagdeev *et al.* [2] published the fluxes of the finest dust grains near comet Halley, but failed to determine their composition.

The limiting sensitivity of dust counters onboard the Vega and Giotto spacecraft was 10^{-16} g [3, 4]. The interplanetary dust is also known to contain considerably smaller grains with radii of several tens of angstroms and with masses down to 10^{-20} g. These data were obtained from ultraviolet observations of the interstellar extinction [5], from the infrared spectra of reflection nebulae [6], and from an analysis of quasi-noise spectra and unidentified mass peaks in the PUMA spectra [2]. Their detection in the cometary dust is an additional argument for the hypothesis of cometary nuclei as conglomerates of interstellar dust grains.

The PUMA instrument is a time-of-flight mass spectrometer [7]. A collision of dust particles with the instrument target (silver) at a velocity of 80 km s^{-1} gives rise to an ion cloud. The ion mass can be determined from the time of flight through the ion-optical system of the instrument. Ions are recorded by a secondary electron multiplier (SEM) whose sensitivity is enough for individual ions to be detected. The instrument operates in two modes, which differ in the energy scatter of detected ions. The energy windows in the NEW (narrow energy window) and WEW (wide energy window) modes are up to 10 and 100 eV wide, respectively. The modes are switched every 30 seconds.

The PUMA measured spectra of dust particles mostly exhibit two components: light ones (organic material) and heavy ones (silicates) [1, 8, 9]. Among the peaks of the major dominating elements in the PUMA-1 spectra, there are many unidentified small-amplitude peaks (Fig. 1a). Quasi-random peaks are present in the spectra where there are no peaks with a well-defined mass scale (Figs. 1b and 1c). In this case, the recording system is triggered not by impacts of large grains, but by random fluctuations of the triggering signals or automatically, after a lapse of specified time. These quasi-random spectra were observed far from the cometary nucleus (> 500 000 km), whereas the mass spectra of dust particles were recorded at distances $r < 2 \times 10^5$ km from the nucleus. In the PUMA-2

* E-mail address for contacts: bzubkov@romance.iki.rssi.ru

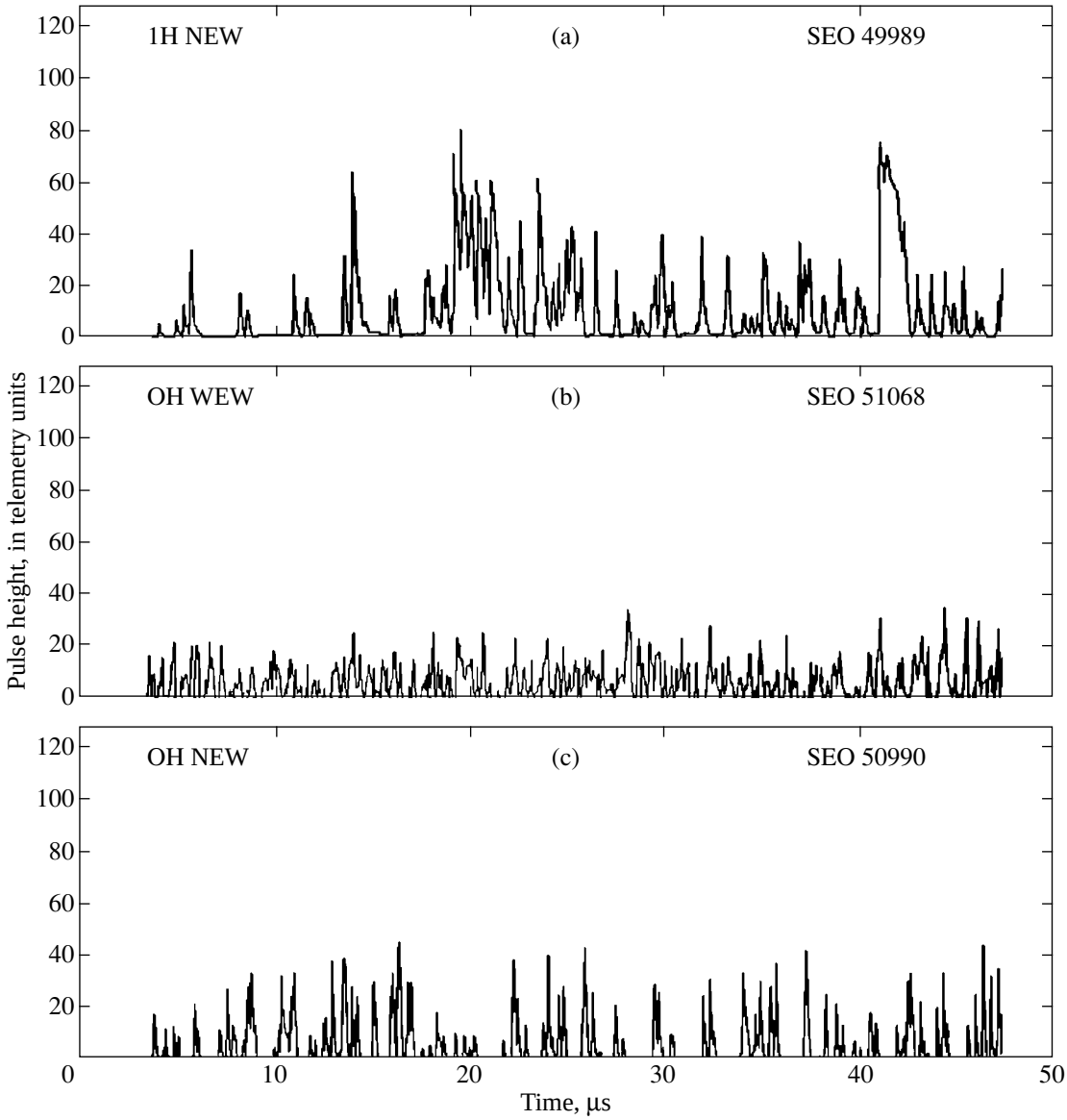

Fig. 1. Examples of PUMA-1 time-of-flight spectra: (a) the spectrum of a dust particle with mass 10^{-16} g (NEW), containing the peaks of dominating elements with a well-defined mass scale and unidentified low-amplitude peaks; (b) the quasi-noise spectrum (WEW); and (c) the quasi-noise spectrum (NEW).

instrument, quasi-noise events were recorded only at a rated voltage on the SEM (3300 V). When the SEM voltage spontaneously dropped to 2400 V at a distance of 2.5×10^5 km from the cometary nucleus, the small-amplitude peaks disappeared. When both instruments were switched on a day before the flyby, no quasi-noise pulses were recorded.

Characteristics of the set of quasi-noise events averaged over 30-s time intervals (corresponding to the switching of the recording modes) are shown in Figs. 2 (PUMA-1) and 3 (PUMA-2). The variations in spectrum characteristics during the motion along the flight trajectory and the dependence on recording modes (different modes of PUMA operation) suggest that the observed spectra are determined by external factors rather than by instrumental effects. The number of quasi-noise peaks in the spectrum increases as the spacecraft approaches the cometary nucleus, with their number in the wide energy window being a factor of 3 to 4 larger than that in the narrow one. At distances of less than 10^5 km from the nucleus, the saturation by the number of peaks in the spectrum begins to show up. As the spacecraft approaches the nucleus, the mean charge of the primary ions corresponding to these peaks also increases. At distances exceeding 3×10^5 km (before the flyby of the cometary nucleus) and 10^5 km (after the flyby), the amplitudes of the peaks are virtually the same in all windows and correspond to several elementary charges. In the trajectory region closer to the nucleus, the amplitude in the wide window is larger

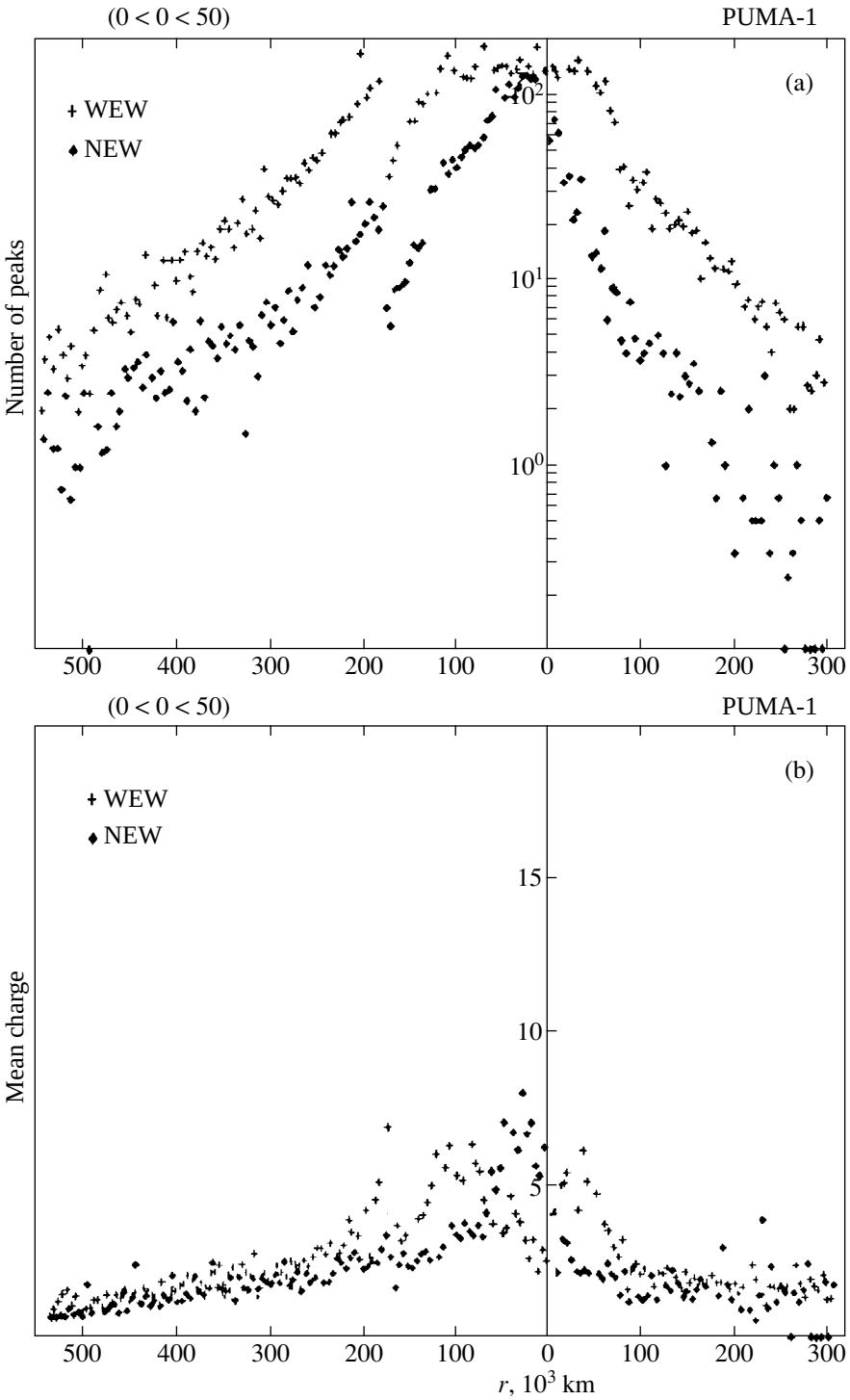

Fig. 2. PUMA-1. Characteristics of the quasi-noise spectra: (a) the number of peaks in the frame and (b) the mean charge as a function of the distance to the cometary nucleus.

than that in the narrow one until the SEM is overloaded [2]. The set of the above experimental data suggests that the quasi-random peaks in the noise spectra and the unidentified peaks in the normal spectra are produced by very small dust particles in comet Halley's dust shell [2].

The composition of fine dust grains was determined by analyzing the differences between the occurrence times of peaks with a specified combination of elements. We considered only combinations corresponding to different sets of two, three, and four elements from eight elements—H, C, O, Mg, Si, Ca, Fe, and Ag.

Table 1. Dominating combinations of elements in the PUMA-1 test spectra at the pulse discrimination levels $A_{min} = 20$ and $A_{min} = 30$

m	Window	Combinations
3	N	(C, O, Mg), (Mg, Si, Ca), (Mg, Ca, Fe)
	W	(H, C, Ag), (H, Mg, Ag), (H, Si, Ag), (C, Mg, Ag)
4	N	(Mg, Si, Ca, Fe), (O, Mg, Ca, Fe), (O, Mg, Si, Ca)
	W	(H, C, Mg, Ag), (H, C, Si, Ag), (H, C, O, Ag), (H, O, Si, Ag)
5	N	(Mg, Si, Ca, Fe, Ag), (O, Mg, Si, Ca, Fe)
	W	(H, C, Mg, Si, Ag), (H, C, O, Si, Ag), (H, C, O, Mg, Ag), (H, O, Mg, Si, Ag)

Figure 4 explains how this type of processing is performed. It shows the PUMA-2 quasi-noise spectrum (random start) with a rule (at the bottom) with the scale corresponding to the positions of the above elements in the normal spectrum of large particles ($>10^{-16}$ g) with allowance for the instrument operation mode (wide or narrow window). By moving this rule along the time axis of the quasi-noise spectrum, we can bring the rule scale, with some accuracy ν, into coincidence with peaks in the spectrum and, thus, determine the combinations of elements produced by the impact of a single particle, as well as establish the start time—when a dust particle hits the target.

Having determined the possible combinations in each spectrum in this way, we can estimate the occurrence probability of a given combination R_m consisting of *m* peaks:

$$P(R_m, \nu) = \frac{1}{n - r_m}\frac{1}{N}\sum_{i=1}^{N} S_i(R_m, \nu).$$

Here, *N* is the number of spectra; $S_i(R_m, \nu)$ is the number of occurrences of the combination R_m in the *i*th spectrum derived from experimental data; *n* is the spectrum length in time intervals; r_m is the separation between the first and the last peaks in the combination R_m; and ν is the accuracy of its determination in time intervals. In our calculations given below, we take $\nu = 3$.

The calculated probabilities were arranged in decreasing order within each group of combinations with the specified *m* ($m = 2$; $m = 3$; $m = 4$).

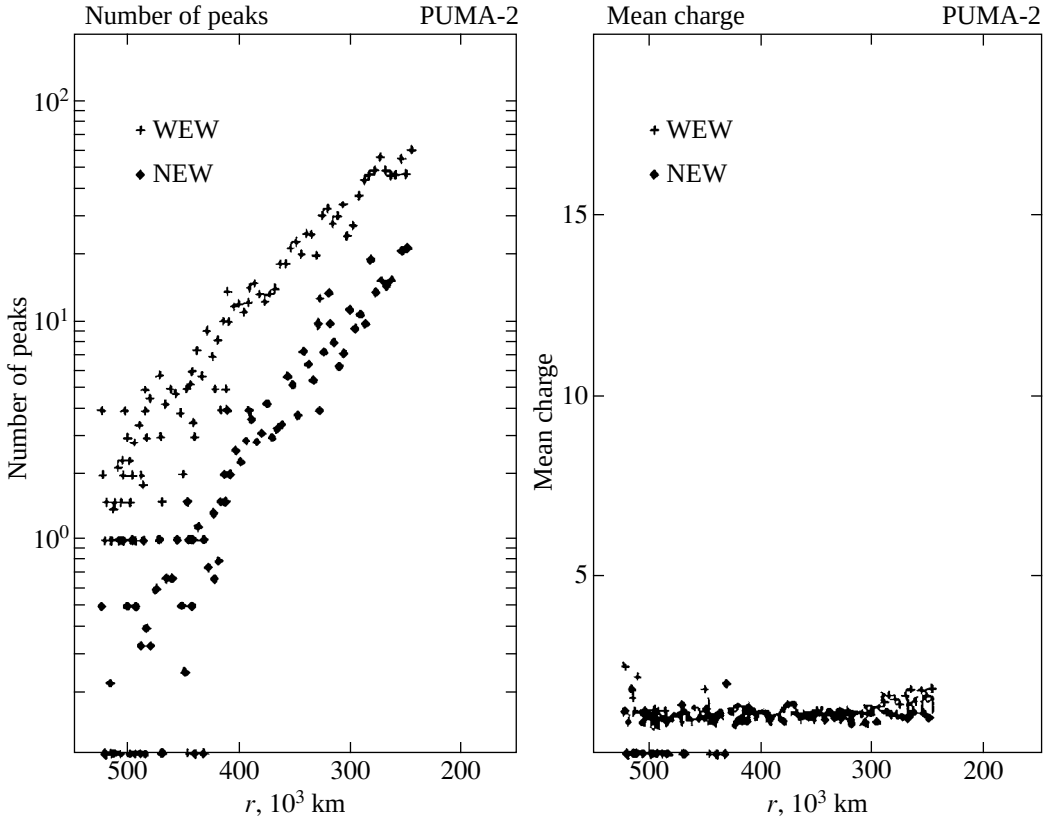

Fig. 3. PUMA-2. Characteristics of the quasi-noise spectra: the number of peaks in the frame and the mean charge as a function of the distance to the cometary nucleus.

Table 2. Dominating combinations of elements in the PUMA-1 quasi-noise spectra (the minimum distance to the comet is 255000 km) recorded at the pulse discrimination levels $A_{min} = 20$ and $A_{min} = 30$

m	Window	Combinations
3	N	(O, Si, Ca), (C, O, Si), (Mg, Ca, Ag), (O, Mg, Si), (C, Mg, Si)
	W	(H, Mg, Si), (Mg, Fe, Ag), (C, Fe, Ag), (H, O, Si), (H, Mg, Fe)
4	N	(C, O, Si, Ca), (C, O, Mg, Si), (O, Mg, Si, Fe), (H, O, Ca, Ag), (C, O, Si, Fe)
5	W	(H, C, Mg, Si), (H, Mg, Ca, Fe), (H, Mg, Si, Ca), (H, O, Mg, Si), (O, Mg, Fe, Ag)

Table 3. Dominating combinations of elements in the PUMA-2 quasi-noise spectra (the minimum distance of 404000 km to the comet) at the pulse discrimination levels $A_{min} = 0$ and $A_{min} = 5$

m	Window	Combinations
2	N	(Mg, Ag), (C, O), (Mg, Si), (O, Si), (Mg, Fe)
	W	(C, Ag), (Mg, Si), (C, O), (H, C), (Ca, Fe)
3	N	(C, O, Si), (H, C, O), (O, Mg, Si), (C, Mg, Si), (C, Mg, Ca)
		(H, C, Ag), (H, Si, Ag), (H, O, Ca), (H, O, Ag), (H, C, Ca)
4	N	(C, Mg, Si, Ca), (H, CO, Si), (H, C, Ca, Fe), (C, O, Mg, Si), (C, O, Si, Ca)
	W	(H, C, Si, Ag), (H, C, O, Ag), (H, O, Si, Ag), (H, C, Ca, Ag), (H, O, Ca, Fe)

To distinguish the most probable combinations of elements, we used a random-number generator to synthesize *N* artificial spectra, in which pulses occur with the same mean probability as those in actual quasi-noise spectra (see Appendix). In the synthesized spectra, we calculated $P'(R_m, \nu)$, the occurrence probability of the combination R_m, and the deviation $\Delta'(R_m, \nu) = P'(R_m, \nu)_{max} - P'(R_m, \nu)_{min}$. Assuming that the deviation $\Delta''(R_m, \nu) \le \Delta'(R_m, \nu)$ for actual spectra, we can determine the most probable combinations of elements, R_m, satisfying the condition

$$P''(R_m, \nu) > P''_{min}(R_m, \nu) + \Delta'(R_m, \nu).$$

For such values of $P''(R_m, \nu)$, the peaks in the spectra can no longer be considered as random.

This processing technique was initially tested on the PUMA-1 spectra in zero mode with a well-defined mass scale. The PUMA-2 spectra are unsuitable for this purpose because of the large width of the mass lines and, accordingly, the large error ($\nu = 6$).

The results of processing such test spectra by this method are presented in Fig. 5 (see Appendix for a detailed explanation of Figs. 5–7). In these figures, the occurrence probabilities $P''(R_m, \nu)$ and $P'(R_m, \nu)$ of combinations, respectively, in the test and synthesized spectra are plotted along the *y* axis. The values of $P''(R_m, \nu)$ are arranged in decreasing order in each group of combinations with a specified value of *m*. The vertical lines on the *x* axis mark the regions corresponding to each value of *m* ($m = 2$; $m = 3$; $m = 4$). The horizontal lines indicate the boundaries above which the most probable combinations of elements are located.

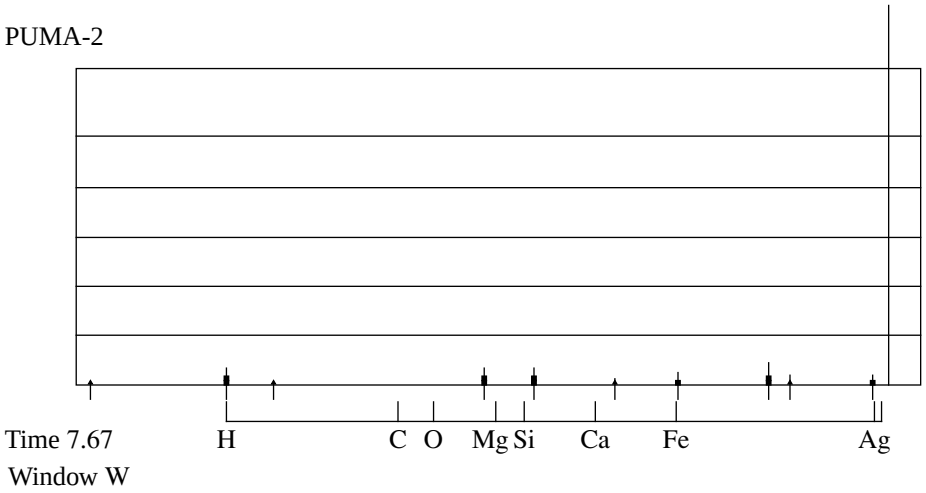

Fig. 4. The method for "manually" determining possible combinations of elements in the PUMA-2 quasi-random spectra. A close coincidence of H, Fe, and Ag is observed in the spectrum.

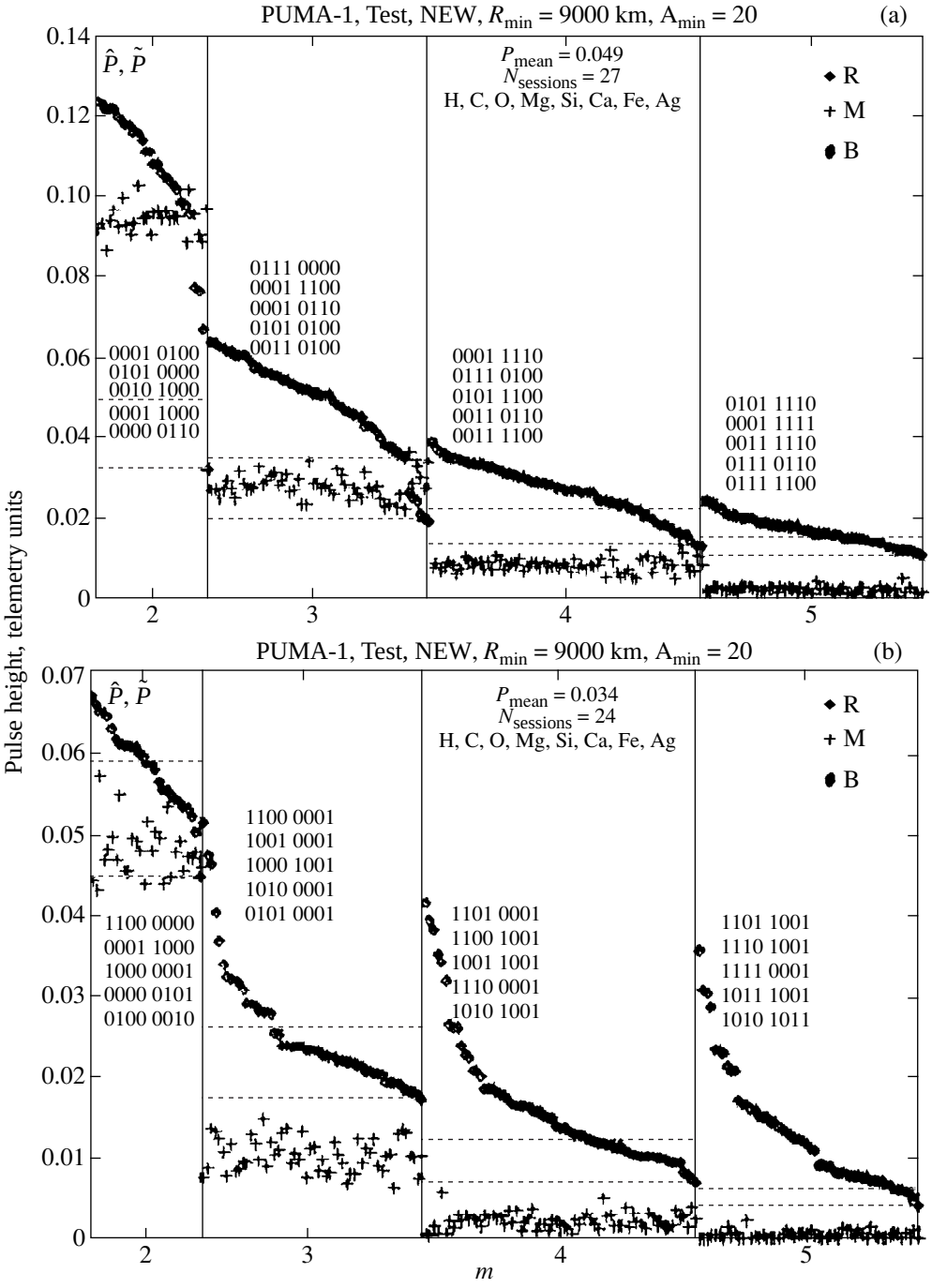

Fig. 5. The minimum pulse height A_{min} = 20 (telemetry units) in the spectrum. (R) The occurrence probabilities P'' of combinations of elements composed of m pulses (m = 2, 3, 4, 5) arranged in decreasing order for the PUMA-1 spectra with a well-defined mass scale: 27 spectra are for the narrow energy window (N); 24 spectra are for the wide energy window (W); (M) the occurrence probabilities P' of combinations for synthesized spectra; (B) is the dispersion boundary for P''.

The dominating combinations of elements H, C, O, Mg, Si, Ca, Fe, and Ag in the PUMA-1 test spectra are clearly distinguished at pulse discrimination levels A_{min} = 20 and A_{min} = 30 (Table 1).

The above data show that hydrogen is always present in the WEW recording mode in combinations with m = 3, 4, and 5 for A_{min} = 20–30 and absent in the NEW mode, in agreement with experimental data [8]. At a high discrimination level, A_{min} = 30, silver is also detected in all recording modes both in the narrow (N) and wide (W) windows. Thus, our procedure for distinguishing probable combinations of elements can be successfully used at a fairly small number of peaks in

the spectrum. A decrease in the number of peaks when processing the test PUMA-1 spectra is achieved by increasing the pulse-height discrimination level.

The combinations of elements, including hydrogen even at a high discrimination level (A = 20, Fig. 6), in the recording modes with narrow and wide energy windows are most probable in the PUMA-1 quasi-noise spectra (a minimum distance of 255 000 km to the comet). This is attributable to instability of the period of switching of the recording modes, i.e., to an improper identification of the recording mode. For a minimum distance to the comet of 9000 km, increasing the discrimination level to A = 20 yields the same

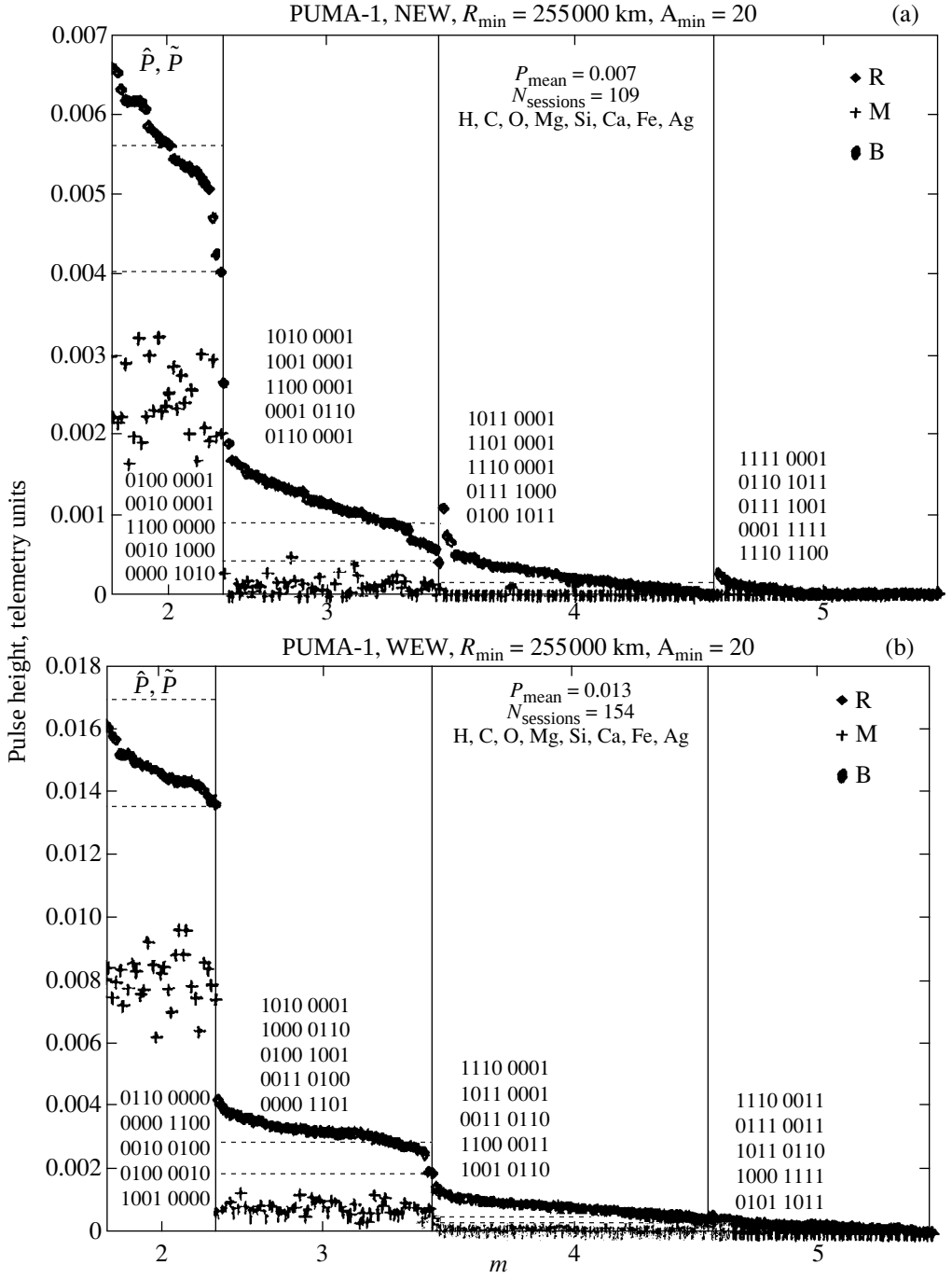

Fig. 6. The minimum pulse height A_{min} = 10 (telemetry units) in the spectrum; the minimum distance to the comet is 255 000 km. (R) The occurrence probabilities P'' of combinations of elements composed of m pulses (m = 2, 3, 4, 5) arranged in decreasing order for the PUMA-1 spectra: 161 spectra are for the narrow energy window (N); 183 spectra are for the wide energy window (W); (M) the occurrence probabilities P' of combinations for synthesized spectra; (B) is the dispersion boundary for P''.

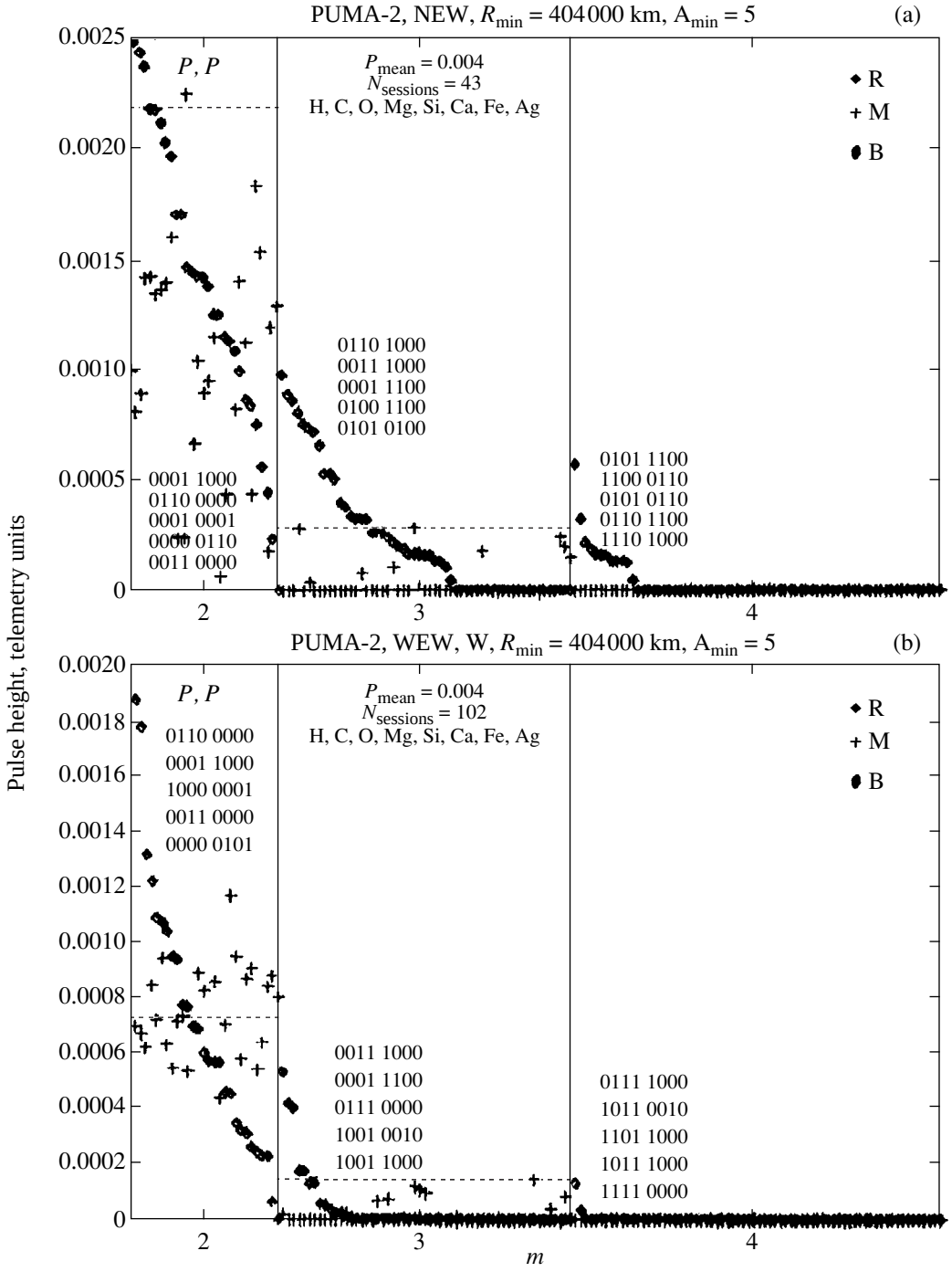

Fig. 7. The minimum pulse height A_{min} = 5 (telemetry units) in the spectrum; the minimum distance to the comet is 404 000 km. (R) The occurrence probabilities *P*'' of combinations of elements composed of *m* pulses (*m* = 2, 3, 4, 5) arranged in decreasing order for the PUMA-2 quasi-noise spectra: 99 spectra are for the narrow energy window (N); 138 spectra are for the wide energy window (W); (M) the occurrence probabilities *P*' of combinations for synthesized spectra; (B) is the dispersion boundary for *P*''.

results as those obtained when processing the test peaks.

In this case, hydrogen is also suppressed in the narrow energy window in almost all most probable combinations of elements. This is yet another confirmation (along with the change in the number and amplitude of peaks when switching the recording modes) that the finest dust particles actually exist.

The most probable combinations of elements for the finest particles are given in Table 2.

The results of processing the PUMA-2 quasi-noise spectra are shown in Fig. 7 (for a minimum distance to

Table 4. Coincident most probable combinations for the PUMA-1 test spectra and for the PUMA-2 quasi-noise spectra

m	Window	Minimum distance 255000 km	Minimum distance 404000 km
		combinations	combinations
2	N	(Mg, Si)	(Mg, Si), (O, Si)
	W	(H, Ag), (Mg, Si)	(H, C), (Mg, Si), (C, Ag), (H, Ag)
3	N	(Mg, Si, Ca)	(C, Mg, Ca)
	W	(H, Mg, Ag)	(H, C, Ag), (H, Si, Ag), (H, O, Ag)
4	N	(C, Mg, Si, Ca)	(C, Mg, Si, Ca)
	W	(H, C, O, Ag), (H, O, Si, Ag)	(H, C, O, Ag), (H, O, Si, Ag)

the comet of 404 000 km). These spectra were sorted out by the operating modes (narrow or wide energy window) and have a small number (about twenty) of pulses in the frame. For this reason, our method of distinguishing the most probable combinations of elements yields better results than does the processing of PUMA-1 quasi-noise spectra. As in the test spectra, hydrogen is absent in the most probable combinations of elements in the NEW recording mode, but is detected in the WEW mode. The most probable combinations of elements for a minimum distance to the comet of 404 000 km are given in Table 3. The most probable combinations in the PUMA-2 quasi-noise spectra are retained as the spacecraft approaches the comet.

The most probable combinations of elements for the PUMA-1 test spectra (Fig. 5) and PUMA-2 quasi-noise spectra (Fig. 7) coincide for the following combinations from Table 4.

Let us summarize the main results of processing the PUMA-1 and PUMA-2 quasi-noise spectra:

(1) The most probable combinations of elements in the quasi-noise and test spectra of large particles are identical: (Mg, Si), (H, C), (H, Si), (H, O), (H, C, O), (H, O, Si), and (C, Mg, Si). The most probable combinations of elements in the PUMA-1 and PUMA-2 quasi-noise spectra are retained along the entire flight path.

(2) The target material (silver) is present in the most probable combinations of elements in the quasi-noise spectra.

(3) Hydrogen is suppressed in the combinations of elements in the quasi-noise spectra in the NEW recording mode and is present in the combinations in the WEW mode. The same effect is observed in the spectra of "large" dust particles.

Our results [the presence of target material (silver) in the spectra and the suppression of hydrogen in the narrow energy window of the instrument] are yet another confirmation of the existence of very light ($<10^{-17}$ g) particles and suggest that the elemental composition of such dust grains is similar to that of "normal" dust particles (with $m > 10^{-16}$ g). The chemical composition of very fine dust grains may differ markedly from that of large grains, if only because the lifetime of these dust grains from the time of their escape from the nucleus to the time of measurement is longer by one or two orders of magnitude.

ACKNOWLEDGMENTS

This study was supported by grant no. 493 of the International Scientific and Technical Center.

REFERENCES

1. J. Kissel, R. Z. Sagdeev, J. L. Bertaux, *et al.*, Nature **321**, 280 (1986).
2. R. Z. Sagdeev, E. N. Evlanov, O. F. Prilutski, and B. V. Zubkov, Adv. Space Res. **9**, 263 (1989).
3. E. P. Masets, R. Z. Sagdeev, R. L. Aptekar, *et al.*, in *Proceedings of 20th ESLAB Symposium on the Exploration of Halley's Comet, 1986*, ESA SP-250, Vol. 2, p. 3.
4. J. A. M. McDonnell, J. Kissel, E. Grun, *et al.*, in *Proceedings of 20th ESLAB Symposium on the Exploration of Halley's Comet, 1986*, ESA SP-250, Vol. 2, p. 25.
5. S. S. Hong and J. M. Greenberg, Astron. Astrophys. **88**, 194 (1980).
6. K. Sellgren, Astrophys. J. **277**, 623 (1984).
7. *Description and Scientific Objectives of the Venera–Galileo Mission*, Ed. by V. M. Balebanov, G. A. Skuridin and É. A. Vorontsova (Lui-Jean, Paris, 1984), p. 108.
8. E. K. Jesberger, A. Christofilidis, and J. Kissel, Nature **332**, 691 (1988).
9. R. Z. Sagdeev, E. N. Evlanov, B. V. Zubkov, *et al.*, Kosm. Issled. **25**, 825 (1987).
10. M. N. Fomenkova and V. N. Khromov, Kosm. Issled. **25**, 825 (1987).

APPENDIX

After their preliminary processing, the PUMA-1 and PUMA-2 measurements are a sequence of realizations of a pulse random process.

Consider one realization containing n counts and L pulses at points $1 \le t_1 < t_2, \ldots, < t_L \le n$. Let some combination of m pulses be specified, in which the separation between the kth and the first pulses is r_k, $k = 2, m$. We denote this combination by $R_m = \{r_2, \ldots, r_m\}$.

We introduce events A_i that there is a pulse at point i and the random variables ξ_i are equal to unity if A_i is

Table 5. The dependence of the time of flight T on the ion mass M

	H	C	O	Mg	Si	Ca	Fe	Ag
M	1	12	16	24	28	40	56	108
T(N)	59.3	205.3	273.1	290.3	313.6	374.8	443.5	615.9
T(W)	56.2	194.8	224.9	275.5	297.6	355.7	420.8	584.4

true and zero otherwise. We say that the combination $\{r_2, \ldots, r_m\}$ occurs at point i if the random variable $\eta_i = \xi_i \xi_{i+r_2} \ldots \xi_{i+r_m}$ is unity.

The total number of combinations R_m occurring in one realization is

$$S(R_m) = \sum_{i=1}^{n-r_m} \eta_i.$$

Assume that the probability $\mathrm{Prob}(\eta_i = 1) = P(R_m)$ is independent of i. The mean value is then

$$E[S(R_m)] = (n - r_m)P(R_m).$$

If all ξ_i are independent and equal to unity with probability p, then

$$P(R_m) = p^m.$$

Consider now a real situation in which the pulse occurrence times are determined to within some integer number of counts $\nu \geq 0$. Let $A_i(\nu)$ be the event that there is at least one pulse in the ν-neighborhood of point i, i.e.,

$$A_i(\nu) = \sum_{k=-\nu}^{\nu} A_{i+k}.$$

We say that the combination R_m has occurred at point i with accuracy ν if the event $B_i(\nu) = A_i(\nu) A_{i+r_2}(\nu) \ldots A_{i+r_m}(\nu)$ is true.

Introduce the random variable $\eta_i(\nu)$ equal to unity if $B_i(\nu)$ is true and zero otherwise. The total number of occurred combinations R_m is then

$$S(R_m, \nu) = \sum_{i=1}^{n-r_m} \eta_i(\nu). \quad (1)$$

Assume that the probability $\mathrm{Prob}(B_i) = P(R_m, \nu)$ is independent of i. The mean value is then

$$E(S(R_m, \nu)) = (n - r_m)P(R_m, \nu). \quad (2)$$

Let us consider the case where ξ_i are independent and $\mathrm{Prob}(\xi_i = 1) = p$, $\mathrm{Prob}(\xi_i = 0) = 1 - p$. We then have

$$\mathrm{Prob}(A_i(\nu)) = 1 - (1 - p)^{2\nu+1} \equiv p(\nu).$$

Assume, in addition, that all $r_k > 2\nu$. The events $A_i(\nu)$, $A_{i+r_2}(\nu)$, and $A_{i+r_m}(\nu)$ are then independent and

$$\mathrm{Prob}(B_i(\nu)) = p^m(\nu),$$

and the formula for the mean value takes the form

$$E(S(R_m, \nu)) = (n - r_m)p^m(\nu). \quad (3)$$

Formulas (1) and (2) enable us to estimate $P(R_m, \nu)$ from the measurements in question.

Let there be N sessions, each being n counts long. The number $S_i(R_m, \nu)$ of occurred combinations R_m can be determined by exhaustion for the ith session and for the specified combination R_m. By taking an average over all sessions, we estimate $E(S(R_m, \nu))$ from formula (1). Subsequently, the probability $P(R_m, \nu)$ can be easily estimated from formula (2):

$$P(R_m, \nu) = \frac{1}{n - r_m} \frac{1}{N} \sum_{i=1}^{N} S_i(R_m, \nu). \quad (4)$$

In our calculations, we considered only the combinations corresponding to different sets (of 2, 3, etc.) from eight elements: H, C, O, Mg, Si, Ca. Fe, and Ag. For a fixed m, the number of different combinations R_m is clearly C_8^m. The experimental dependence of the time T of motion of an ion with mass M in the ion-optical system of the instrument was also assumed to be known:

$$\mathrm{T} = A\sqrt{\mathrm{M}} + B,$$

where A and B are some coefficients depending on two operating modes of the instrument: with "narrow" (N) and "wide" (W) windows. The values of T we used (in counts, 1 count = 66.7 ns) are given in Table 5.

Using this table, we can calculate $r_2, \ldots, r_m$ for each combination R_m. Note also that, according to Table 5, an eight-digit code composed of 0 and 1 can correspond to each combination. For example, "10000001" means the combination (H, Ag). These designations are used below.

Let us turn back to formula (4). The values of $P(R_m, \nu)$ calculated from N realizations may be broken up into groups, depending on $m = 2, 3\ldots$ The combinations in each group may be arranged in order of decreasing probability $P(R_m, \nu)$. How significant is the difference between the maximum and minimum probabilities in the group?

Let us formulate this question more clearly. Consider a model in which pulses in each session occur independently of each other with some probability P_{mean}. It follows from formula (3) that, in this case, $P(R_m, \nu)$ must be constant for a fixed m. Can the spread

in calculated $P(R_m, \nu)$ be explained in terms of this model?

To answer this question, we use numerical simulations. Let L_i be the number of pulses in the ith session of length n and let $i = 1, \ldots, N$. The mean occurrence probability of a pulse is then

$$P_{\text{mean}} = \frac{1}{N}\sum_{i=1}^{N}\frac{L_i}{n}.$$

Using a random-number generator, we produce N artificial sessions in which pulses occur with the probability P_{mean}. Based on these data, we obtain estimates in the same manner as the estimates for real measurements. (The symbols ['] and ["] are used to denote the estimates for model and real measurements, respectively.)

Let $P'_{\text{min}}(m, \nu)$ and $P'_{\text{max}}(m, \nu)$ be the minimum and maximum values of $P(R_m, \nu)$ for all combinations with a fixed m.

Denote the differences $\Delta'(m, \nu)$ obtained from model and real measurements by $\Delta'(m, \nu) = P'_{\text{max}}(m, \nu) - P'_{\text{min}}(m, \nu)$ and $\Delta''(m, \nu)$ respectively. If the model is valid for real measurements, then there must be $\Delta''(m, \nu) \le \Delta'(m, \nu)$. If this condition is not satisfied, then the occurrence of combinations with

$$P''(R_m, \nu) > P''_{\text{min}}(R_m, \nu) + \Delta'(m, \nu)$$

cannot be explained in terms of the model with random independent pulses.

When performing our calculations, we broke up the data for each instrument into groups by two characteristics: the distance to the comet and the operation mode. In addition, the calculations within each group were carried out for various values of the minimum pulse height A_{min}; i.e., only pulses with an amplitude larger than or equal to A_{min} were included in the processing procedure.

The results for $\nu = 3$ are shown in Figs. 5–7. Let us describe the notation in these figures.

The curve R represents the values of $P''(R_m, \nu)$ arranged in decreasing order within each group of combinations with the specified m. The vertical lines on the x axis mark the regions corresponding to each value of $m = 2$, 3, and 4. The points "M" correspond to the model values of $P'(R_m, \nu)$.

The horizontal lines "B" denote the boundaries $P'_{\text{min}}(m, \nu)$ and $P''_{\text{min}}(m, \nu) + \Delta'(m, \nu)$. Five combinations with maximum probabilities $P''(R_m, \nu)$ are given in the region corresponding to each m.

In addition, the values of P_{mean}, the number of sessions N involved in our calculations, and the minimum distance to the comet R_{min} are given in the figures. The letters "N" and "W" in all figures denotes the NEW and WEW operation modes, respectively.

Note especially the graphs representing the results of processing for a special set of sessions selected by an expert. This set is labeled "test."

Translated by A. Kozlenkov